MINISTRY OF EDUCATION AND TRAINING
HCM CITY UNIVERSITY OF TECHNOLOGY AND EDUCATION

---oo0oo---

PHAN THI DANG THU

BUCKLING ANALYSIS OF INFLATABLE COMPOSITE BEAMS

PHD THESIS
MAJOR: MECHANICAL ENGINEERING
CODE: 9520103

HCM City, August 2021

MINISTRY OF EDUCATION AND TRAINING
HCM CITY UNIVERSITY OF TECHNOLOGY AND EDUCATION

--- oOo ---

PHAN THI DANG THU

BUCKLING ANALYSIS OF INFLATABLE COMPOSITE BEAMS

MAJOR: MECHANICAL ENGINEERING

CODE: 9520103

Supervisor one: Assoc. Prof. Dr. Phan Dinh Huan

Supervisor two: Assoc. Prof. Dr. Le Hieu Giang

Reviewer 1:

Reviewer 2:

Reviewer 3:

HCM City, August 2021

BỘ GIÁO DỤC VÀ ĐÀO TẠO
TRƯỜNG ĐẠI HỌC SƯ PHẠM KỸ THUẬT
THÀNH PHỐ HỒ CHÍ MINH

Số: 238./QĐ-ĐHSPKT-SĐH

CỘNG HÒA XÃ HỘI CHỦ NGHĨA VIỆT NAM
Độc lập – Tự do – Hạnh phúc

Tp. Hồ Chí Minh, ngày 30 tháng 9 năm 2013

QUYẾT ĐỊNH

Về việc giao đề tài luận án và người hướng dẫn nghiên cứu sinh khóa 2013

HIỆU TRƯỞNG TRƯỜNG ĐẠI HỌC SƯ PHẠM KỸ THUẬT TP. HỒ CHÍ MINH

Căn cứ quyết định số 426/QĐ-TTg ngày 27/10/1976 của Thủ tướng Chính phủ quy định về mạng lưới tổ chức và nhiệm vụ của các trường đại học;

Căn cứ chương 6 Điều lệ Trường Đại học ban hành kèm theo quyết định số 58/2010/QĐ-TTg ngày 22 tháng 9 năm 2010 của Thủ tướng Chính phủ;

Căn cứ thông tư số 10/2009/TT-BGDĐT ngày 07/5/2009 của Bộ Giáo dục và Đào tạo về việc Ban hành Qui chế đào tạo trình độ tiến sĩ;

Căn cứ thông tư số 05/2012/TT-BGDĐT ngày 15/02/2012 của Bộ Giáo dục và Đào tạo về việc sửa đổi, bổ sung một số điều của Quy chế đào tạo trình độ tiến sĩ ban hành kèm theo Thông tư số 10/2009/TT-BGDĐT ngày 07/5/2009 của Bộ trưởng Bộ Giáo dục và Đào tạo;

Xét nhu cầu công tác và khả năng cán bộ;

Xét đề nghị của Trưởng phòng Đào tạo,

QUYẾT ĐỊNH

Điều 1: Giao đề tài luận án tiến sĩ và người hướng dẫn cho:

Nghiên cứu sinh : ***Phan Thị Đăng Thư***

Ngành : Kỹ thuật cơ khí Khoá: ***2013 – 2016***

Tên luận án : ***Phân tích tính ổn định kết cấu dầm bơm hơi vật liệu Composite***

Người HD thứ nhất (HD chính): ***PGS.TS Phan Đình Huấn***

Người HD thứ hai : ***PGS.TS Lê Hiếu Giang***

Thời gian thực hiện : ***01/10/2013 đến 01/10/2016***

Điều 2: Giao cho Phòng Đào tạo quản lý, thực hiện theo đúng Qui chế đào tạo trình độ tiến sĩ của Bộ Giáo dục & Đào tạo đã ban hành.

Điều 3: - Trưởng các đơn vị và các Ông (Bà) có tên ở điều 1 chịu trách nhiệm thi hành quyết định này.

- Quyết định có hiệu lực kể từ ngày ký.

Nơi nhận :
- BGH (để biết);
- Như điều 2, 3;
- Lưu P.ĐT

HIỆU TRƯỞNG

TRƯỜNG ĐẠI HỌC SƯ PHẠM KỸ THUẬT TP. HỒ CHÍ MINH

PGS.TS Đỗ Văn Dũng

LÝ LỊCH CÁ NHÂN

I. LÝ LỊCH SƠ LƯỢC

Họ và tên: PHAN THỊ ĐĂNG THƯ Giới tính: Nữ

Ngày, tháng, năm sinh: 05/11/1977 Nơi sinh: Tiền Giang

Quên quán: Tiền Giang Dân tộc: Kinh

Học vị cao nhất: Thạc Sỹ Kỹ thuật

Đơn vị công tác: Trường Cao Đẳng Công Nghệ Thủ Đức

Chỗ ở riêng hoặc địa chỉ liên lạc: B2-14/09 c/c Lê Thành, Phường An Lạc, Quận Bình Tân, TP.HCM

Điện thoại liên hệ: 0903373645 Email: dangthu0511@yahoo.com

II. QUÁ TRÌNH ĐÀO TẠO

1. Đại học:

- Hệ đào tạo: Chính qui
- Nơi đào tạo: Trường Đại học Sư phạm Kỹ thuật TP. HCM
- Ngành học: Kỹ thuật công nghiệp
- Năm tốt nghiệp: 2000

2. Sau đại học

- Hệ đào tạo: Chính qui
- Nơi đào tạo: trường Đại học Sư phạm Kỹ thuật Tp. HCM - Việt Nam
- Thạc sĩ chuyên ngành: Kỹ thuật cơ khí
- Năm tốt nghiệp: 2004

III. QUÁ TRÌNH CÔNG TÁC

- 2000-2005: Giảng viên - Trường Cao đẳng Bán công Công nghệ và quản trị doanh nghiệp.
- 2005-2019: Giảng viên, Trưởng khoa Cơ khí - Trường Cao đẳng nghề TPHCM
- 2019-2020: Giảng viên, Giám đốc trung tâm - Viện khoa học An toàn vệ sinh lao động TPHCM

- 2020 đến nay: Giảng viên - Trường Cao đẳng Công nghệ Thủ Đức TPHCM

IV. LĨNH VỰC CHUYÊN MÔN

- CAD/CAM/CNC
- Gia công CNC
- Thiết kế kỹ thuật cơ khí

V. CÁC CÔNG TRÌNH ĐÃ CÔNG BỐ

Số TT	NỘI DUNG
1	T. Le-Manh, Q. Huynh-Van, **Thu D. Phan**, Huan D. Phan, H. Nguyen-Xuan "Isogeometric nonlinear bending and buckling analysis of variablethickness composite plate structures"; Composite Structures 1 January 2017, Pages 818-826.
2	**Phan Thi Dang Thu**, Phan Dinh Huan and Nguyen Thanh Truong "Effect parametric to properties of a 2D orthogonal plain classical woven fabric composite"; ISBN: 978-604-913-367-1, pages 509-517.
3	**Phan Thi Dang Thu**, Phan Dinh Huan and Nguyen Thanh Truong "Biaxial beam inflation test on orthotropic fabric beam"; ISBN: 978-604-913-213-1, pages 1169-1176.
4	Nguyen Thanh Truong, Phan Dinh Huan, **Phan Thi Dang Thu** "Discretizing an analytical inflating beam model by the shellmembrane finite elelment"; ISBN: 978-604-913-213-1, pages 1221-1228.
5	**Phan Thi Dang Thu**, Le Manh Tuan, Nguyen Xuan Hung, Nguyen Thanh Truong "Geometrically nonlinear behaviour of composite beams of variable fiber volume fraction in isogeometric analysis"; ISBN: 978-604-82-2028-0, Pages: 1404-1409.
6	**Thu Phan-Thi-Dang**, Tuan Le-Manh, Giang Le-Hieu, Truong Nguyen-Thanh "Buckling of cylindrical inflating composite beams using isogeometric analysis"; ISBN: 978-604-73-3691-3, Pages 821-826.

Số TT	NỘI DUNG
7	**Phan Thi Dang Thu**, Nguyen Thanh Truong, Phan Dinh Huan "Mô hình dầm hơi composite phi tuyến chịu uốn"; ISBN: 976-604-82-2026-6, Page 697-704.
8	**Phan Thi Dang Thu**, Nguyen Thanh Truong, Phan Dinh Huan, Le Dinh Tuan "Biaxial experiments for determining material properties and joint strength of textile plain woven fabric composites"; ISBN: 978-604-913-722-8, Page 1174-1181.

TP. HCM, ngày 12 tháng 8 năm 2021

Nghiên cứu sinh

Phan Thị Đăng Thư

ORIGINALITY STATEMENT

I, Phan Thị Đăng Thư, hereby assure that this dissertation is my own work, done under the guidance of Assoc. Prof. Dr. Phan Dinh Huan and Assoc. Prof. Dr. Le Hieu Giang with the best of my knowledge.

All results and data that are stated and presented in this dissertation are honest. And they have not been published by any previous works.

Ho Chi Minh City, August 2021

Phan Thi Dang Thu

ACKNOWLEDGEMENTS

The dissertation is implemeted at the Faculty of Mechanical Engineering, Ho Chi Minh City University of Technology and Education, Viet Nam. The conducting process of this thesis not only brings motivation, but it also takes several challenges and difficulties. Without any support and coopperating by my professors, colleagues as well as my students, this thesis would not be achieved completely and fluently.

That is why, first of all, I would like to express my appreciation to Assoc. Prof. Phan Dinh Huan and Assoc. Prof. Le Hieu Giang, for accepting me as a PhD student and for their enthusiastic guidance during my research. Moreover, I would like to kindly thank Dr. Nguyen Thanh Truong, Dr. Le Manh Tuan, Mr. Duong Chi Hung (a young brothers), for their helpful supporting in every first steps of doing research. They conscientiously helped me to overcome during my hardest time.

Secondly, I would like to acknowledge Assoc. Prof. Le Dinh Tuan, Faculty of Transportation Engineering, Ho Chi Minh City University of Technology, Vietnam, who troubleshooted my troubles and helped to solve problems incidentally occurring in my study.

Thirdly, I also take this chance to thank all my talent colleagues for their professional instruction and advice, as well as to my lovely students for their nicely support.

Last but not least, the family’s love and encouragement are definitely my biggest motivation. They gave me plenty of valuable assistance with their love and affection.

Phan Thi Dang Thu

ABSTRACT

This thesis presents a numerical modeling and an experimental program approach to investigate the buckling behavior of inflatable beams made from woven fabric composite materials.

In the numerical study, the Isogeometric Analysis (IGA) is utilized to analyze the bucking response of inflatable beams subject to axial compressive load and predict the critical load at which the first wrinkle occurs. In the numerical model, the Timoshenko's kinematics principle is used to build a 3D model of inflating orthotropic beams. In this modeling process, geometrical non-linearity is considerated by using the energy concept that accounts for the change in membrane and strain energies when the beams are bent. By using Lagrangian and virtual work principles, nonlinear equilibrium equations were derived. These equations are then discretized by using NURBS basis functions inherited from IGA approach to derive the global nonlinear equation. The well-known Newton-Raphson algorithm is then used to solve the nonlinear equation. The numerical results are then calibrated with the experimental one. It was found that a good agreement between IGA predictions and test results is achieved. The numerical model could be used for other parametric studies to investigate the influences of material and geometrial parameters on the buckling behaviour of inflatable beams.

In the experiment study, the mechanical properties of the woven fabric composite material used in frabrication of inflatable beams are determined and the biaxial buckling test is carried out. The experimental studies are performed under various inflation pressures to characterize the orthotropic mechanical properties and the nonlinear buckling behaviors. Load versus deflection curve of inflating beams beam with different air pressures obtained from the experimentsare are illustrated., and the first wrinkles of the beams when buckling happens is also monitored. Therefore, the maximum load carrying capacity of the inflating beam with respect to the appearance of the first wrinkle is totally found. In addition, the critical buckling

load is determined through distinct load cases. Then, the discrepancy is evaluated among the proposed orthotropic and isotropic models in literature.

Contents

Notations and conventions

Abbreviations

CAD	Computer Aided Design
FEA	Finite Element Analysis
IGA	Isogeometric Analysis
FGM	Functionally graded material
3D	Three dimensional
NURBS	Non-Uniform Rational B-splines
DOF	Degree of Freedom
OPCWFC	Orthogonal plain classical woven fabric composite
FE	Finite element
FEM	Finite elementingmethod
HOWF	Homogeneous orthotropic woven fabric
LFEIB	Linear finite elementinginflating beam
NLIBFE	Nonlinear inflating beam finite element

Plain weave fabric testing

(x, y)	Axes of symmetry of plain weave fabric specimen
(L, T)	Axes of symmetry of textile fabric, which are assumed to represent the axes of material symmetry (L: warp direction; T: weft direction)

Textile composite parameters and mechanical properties

t_{ϕ}	Fabric thickness
E_l	Warp effective Young's modulus
E_t	Weft effective Young's modulus
G_{lt}	In-plane effective shear modulus

ν_{lt}	Poisson ratio due to the loading in the warp and contraction in the weft
ν_{tl}	Poisson ratio due to the loading in the weft and contraction in the warp

Constants

c	$\cos\varphi$
s	$\sin\varphi$

Structural mechanics of inflating beams

Coordinates systems

$\underline{l}, \underline{t}, \underline{n}$	Warp, weft, normal directions of the fabric
(X, Y, Z)	Cartesian coordinates
$\left(\underline{e}_X, \underline{e}_Y, \underline{e}_Z\right)$	Unit vectors of the cartesian coordinates
$\varphi = \left(\underline{e_Z, n}\right)$	Angle

Mechanical properties

E	Young modulus of the isotropic fabric
G	Shear modulus of the isotropic fabric
$E^* = Et_o^{'}$	Membrane elastic modulus of the isotropic fabric
$G^* = Gt_o^{'}$	Membrane shear modulus of the isotropic fabric
ν	Poisson ratio of the isotropic fabric
E_l	Modulus of elasticity in warp direction of the orthotropic fabric
E_t	Modulus of elasticity in weft direction of the orthotropic fabric
G_{lt}	In-plane shear modulus of the orthotropic fabric
ν_{lt}	Poisson ratio relative to the contraction of the warp under weft traction
ν_{tl}	Poisson ratio relative to the contraction of the weft under warp traction

E_{eq}	Equivalent Young's modulus of the orthotropic fabric
G_{eq}	Equivalent shear modulus of the orthotropic fabric
ν_{eq}	Equivalent Poisson ratio of the orthotropic fabric
e_{lt}	Level of orthotropy
g_{lt}	Parameter to measure the difference between Glt and Geq
$\underline{\underline{\underline{\underline{C}}}}, \underline{\underline{\underline{\underline{C}}}}^{loc}$	Elasticity tensors

Internal forces

N	Axial force
T_y, T_Z	Shear force along y and z axes
M_y, M_Z	Moments around y and z axes

Beam geometry

l_ϕ	Natural length of the inflating beam
R_ϕ	Natural radius of the inflating beam
t_ϕ	Natural thickness of the inflating beam
l_ϕ	Natural length of the inflating beam
l_o	Reference length of the inflating beam
R_o	Reference radius of the inflating beam
t_o	Reference thickness of the inflating beam
A_o	Reference cross-section area of the inflating beam
I_o	Reference moment of inertia of the inflating beam

Loads

F	Compressive concentrated load
F_X, F_Y, F_Z	Components of concentrated loads
f_x, f_y, f_z	Components of the distributed load
M_Y, M_Z	Components of bending moments

F_w	Wrinkling load
$F_{crushing}$	Crushing load

Pressure, pressure forces

p	Inflation pressure
p_n	Normalized inflation pressure
$F_p = p\pi R_o^2$	Pressure force
N^o	Axial force due to the inflation pressure

Coefficients

k, k_y, k_z	Shear correction coefficients

Kinematics

$\underline{u}$	Displacements field
u	Axial displacement
v, w	Deflections along Y and Z axes
θ_Y, θ_Z	Rotations around Y and Z axes

Tensors

$\underline{\underline{E}}$	Green-Lagrange tensor
E_{XX}, E_{XY}	
E_{XZ}, E_{YY}	Components of $\underline{\underline{E}}$
E_{YZ}, E_{ZZ}	
$\delta\underline{\underline{E}}$	Virtual Green-Lagrange tensor
$\delta E_{XX}, \delta E_{XY}$	
$\delta E_{XZ}, \delta E_{YY}$	Components of $\delta\underline{\underline{E}}$
$\delta E_{YZ}, \delta E_{ZZ}$	
$\underline{\underline{S}}$	Second Piola-Kirchhoff tensor
S_{XX}, S_{XY}	

S_{XZ}, S_{YY}	Components of $\underline{\underline{S}}$
S_{YZ}, S_{ZZ}	
$\underline{\underline{S}}^o$	Inflation pressure prestressing tensor

Functions and constants

Φ_E	Strain energy function
δW_{int}	Internal virtual work
δW_{ext}	External virtual work
δW_{ext}^d	External virtual work of the service load
δW_{ext}^p	External virtual work of the pressure load
$Q_i, i = 1...10$	Quantities depending on the initial geometry of the cross-section

Matrix and tensors for finite elementingformulations

$\{d\}$	Nodal d.o.f
$\{D\}$	Beam d.o.f
$\{\delta D\}$	Buckling displacements
$[k]$	Element conventional elastic stiffness matrix
$[K_\sigma]$	Element initial stress stiffness matrix
$[K]$	Beam conventional elastic stiffness matrix
K_{ref}	Beam initial stress stiffness matrix
K_T	Beam tangent stiffness matrix
$\{D\}_i$	Beam displacement vector at increment step i
$\{\Delta D\}$	Nodal unknown displacement increment
$\{R\}$	Beam residual load
$\{F_{\text{int}}\}$	Internal load vector of the beam
$\{F_{ext}\}$	External load vector of the beam

$[N]$	Shape function matrix
$[B]$	Strain-displacement matrix

Aspect ratios

Linear eigen buckling

K_c^l	Normalized linear buckling load coefficient
λ_s	Slenderness ratio of the beam
R_{rt}	Radius-to-thickness ratio
R_{br}	Bending radius ratio

Nonlinear buckling

K_c^l	Normalized nonlinear load parameter
K_f	Incremental load ratio
R_{lr}	Length-to-radius ratio
R_{fr}	Flexion-to-radius ratio

List of Figure

List of Table

CHAPTER 1: INTRODUCTION

1.1 Background information

The inflating structures are common structures which are currently used in amusing and performing projects, such as buoy houses in children's play areas, welcome gate, animals images, etc. In Vietnam, the inflating structures are a relatively new field. In general, designing and analyzing of the inflating structures for large projects have been facing difficult challenges. This is due to the fact that the structural responses of inflating structures considerbly depends on the infilled air and material of the skin. In addition, there is a shortage in the experimental studies of of inflating structures. Some researchers haved studied the applications of inflating structures for practical purposes based on analutical and numerical modeling approaches. Most of those have been forcusing on the structural performance of infalting beams, which are the fundamental components of the main structures. However, the study for buckling and stability responses of inflating beams is still limited.

Recently, the orthotropic fabric materials are widely used in various industrial field. The continuous improvement in the weaving technique has allowed the construction fabrics becoming more strong and be more resistant to different consitions. The adoption of orthotropic fabric materials to inflating structures have been considered recently thanks to its advantage mechanical properties. However, the study for its applications as infalting beams has not been widely investigated in both experimental and numerical modeling manners. In terms of economic aspects, the numerical modeling approach is much more preferable in recent years thanks to the advantages in computer science. However, the use of analytical approach or traditional finite element method still has their own limits.

Isogeometric Analysis (IGA) is an emerging numerical method that have been widely employed and developed in various computational problems recently. The basic concept of IGA is to integrate the tools of Computer-Aided Design (CAD) with

Finite Element Analysis (FEA). Non-uniform rational B-spline (NURBS) functions, which are commonly used for geometrical modeling in CAD softwares, are exploited in the framework of FEA. This combination could allow for a smooth transition in designing process as the transformation between sketching concept and analysis modeling could be dismissed. The NURBS basis functions inherited from CAD technologies are employed to represent the geometries of models and acts as interpolations for physical fields and state variables. Therefore, exact representation of geometries with high-smooth properties are easy to obtained. In addition, a better rate of convergence could be provided thanks to the higher order capacity of NURBS functions. Another dominant feature of IGA is the ability to provide higher order of continuity among the elements of a patch. This quality, which is obtained from the nature of B-spline and NURBS basis functions, is in contrast to intrinsic C^0 continuity of Lagrange interpolation functions of traditional FEA. In general, those advanced features of IGA in geometrical modeling and providing high-continuity interpolations allow IGA to be the best candidate for the analyses of small-scale structures based on the high-order continuum theories.

1.2 Motivation of the thesis

As the use of woven fabric composite materials have become more popular nowadays, the need for investigating their applications in inflating structures becomes crutial. Therefore, this study is devoted to find out the structural performacne of woven fabric beams under compressive loads in both experiemtnal and numerical modelling approaches. In addition, the application of IGA technique to investigate the stability behaviour of inflating havenot been conducted elsewhere before, therefore a new numerical approach based on IGA is worthly conducted.

1.3 The objectives and scope of the study

The main objectives of this study is to investigate the critical loads of inflating beam made from composite textiles in both experimental and numeriacl modeling approaches. There for the goals of this study could be summarized as follows

1) Develope an experimental program, in which:

1.1) Determine textile composite material constants. These constants are used as input data for calculation programs.

1.2) Set up experiments on inflatable beams in terms of equipments and supplies that can be found locally and purchased from abroad.

1.3) Determine critical load of steam beam structures of composite textile materials with different boundary conditions.

1.4) Investigate the effect of initial internal pressure on the strength of the inflatable beam.

1.5) Investigate the effect of initial internal pressure on critical load causing buckling of inflatable beam structure.

2) Apply the "Isogeometric Analysis - IGA" technique develope a numerical program to determine the critical load for the composite woven fabric's inflating beam with different boundary conditions. A piece of code in MatLAB is developed.

3) Compare the experimental results and those obtained from the numerical approach to validate the accuracy of the developed program.

1.4 Methodology

In order achieve the study scopes, this thesis have used several methods as follows:

- Studying literature review related to the subjects of textile composite materials and inflating structures.
- Refer, study and synthesize critical load calculation models for inflatable beam structures of composite textiles to choose a suitable model for analytical equations and finite element calculation models. The goal of this section is to have more analytical tools and traditional finite element tools to verify the IGA calculation results and the experimental results of the thesis.
- Review of NURBS-based geometry and isogeometric analysis (IGA).
- Derive theories for nonlinear buckling analysis of inflating composite structures under the IGA framework and investigate numerical models.
- Construct analytical model and experiment program for verifying the proposed theory.

1.5 Outline of the thesis

The contents of this thesis are briefly organized as follows:

- Chapter 1 discusses a general introduction to background information, the objective and scope of this study, the methodology and the outline of the thesis. The significances and contributions of the study are also pointed out. It could be observed that constructing an effective analysis model for inflating structures is essential.

- Chapter 2 gives a brief review of fibous compiste materials and their applications. A literature review on previous studies on inflating structures is presented. In addition, a short review on the IGA is discussed.

- Chapter 3 is presented to discuss about basic features of IGA and theoretical development of stability governing equatuons of buckling problems. In the IGA introductory part, fundamental concepts that play inportant role in the IGA apporach, e.g knot vector, B-spline, NURBS basis functions, and etc, are presented. The advantages and disadvantages of IGA comparation and finite elementingmethod are also shown discussed as well. The remaining part of this chapter is about the theoretical development of stability governing equations of the buckling problem. Basic assumptions are presented and the deriviation of the gorvernign equations of the stability problems are discussed in detail.

- Chapter 4 is devoted to the developments of the IGA-based numerical model. The procedure to develop the IGA-based numerical model is presented and the general procedure to solve the global equation are addressed. This study is dedicated to linear eigen analysis and nonlinear buckling analysis of inflating beams that made of orthotropic materials when using isogeometric analyis. The influences of geometric nonlinearities and the inflation pressure on the stability response of inflating beam with different boundary conditions are assessed. The beam aspect ratios influenced on the buckling load coefficient are also indicated. The achieved results and experimental results are compared with available ones in literature as well.

- Chapter 5 presents materials selection, prototyping plan, besides also checks buckling, the relationship between load and curve by varying pressure, etc. An experimental program for buckling behavior of inflating beams fabricated from woven fabric composites is presented in this chapter. It begins with as brief review of buckling of thin-walled shell structures, followed by the material test of woven fabric composites. Next, the fabrication procedure of inflating beams and the buckling testing setup are described in detail. Discusion and remarks on the results obtained are then given.

- Chaper 6 addresses and summaries on research contributions and achievements of this work is presented. Important conclusions and findings are also drawn in this chapter. Finally, some suggestions for further studies are discussed.

1.6 Original contributions of the thesis

In this study, the original contributions of the thesis are covered as follows:

- Investigation of an extension of an IGA-based numerical approach for an application in studying the nonlinear buckling behaviors of inflating beams made from woven fabric composite materials. In the proposed method with a HOWF, the IGA is examined based on the modelling 3D Timoshenko beam. The finite elementing model is established with C^1-type continuity via quadratic NURBS-based Timoshenko elements. Additionlly, the biaxial orthotropic mechanical properties of the materal are determined as the material inputs for finite elementing model and IGA.

- Experimental investigation on determining the critical buckling load and load-carrying capacity of the inflating composite fabric beams.

- Study on effects of different air pressures to determine the load-displacement relation of the inflating beam.

1.7 Significances of the thesis

Nowadays, general various types of materials including wood, metal, stone and fabric are widely used in different induustrial fields. The inflating structures have required great demands to alternative the traditional meterials, including inflating columns, beams and arches. With the continual improvement in the weaving technique, these construction fabrics are often formed into closed tubes, which are inflating to withstand the self and other loads. The advantage between modern textile materials and conventional materials is that the former can be tailored to particular requirements of certain applications, easy to deploy, having lightweight and low volume storage. Such inflating structures are often employed in the fields of aerospace, civil engineering, military, marine, agriculture and entertainment. This requires a good knowledge about the behaviour of materials for structural design and optimization.

There are still not many in-depth research results on structures as well as stable bearing capacity of inflating structures given in Vietnam until present. There is a lack of scientific document on referring to the research and application of this new material in construction. Therefore, the thesis with its importance is given to research, develop, build models, determine the mechanical properties of technical fabrics as well as the calculation theories of inflating structures, for use in construction.

CHAPTER 2: LITERATURE REVIEW

2.1 An overview of fibous composite materials

Besides construction materials such as wood, stone, metal ..., fabric materials today are also widely used in construction works. With continuous improvement in the weaving technique, the construction fabrics are becoming more and more resistant. These construction fabrics are often used to form closed tubes, which are infused with air so that the critical bodies and other loads can be loaded. The bellows are the structural foundations in many constructions around the world: moon-based, site model location, stadium dome, exhibition halls, outdoor temporary structures. The priority of using new materials for structures over type data transmission systems is light weight, easy deployment and rearrangement, it is possible to shape to special shapes image in some applications and use less storage space. Durable, low production costs and low development costs (without the use of tools) also offer various benefits compared to other structures.

The field of composite materials is both old and new. It is old in the sense that most natural objects, including the human body, plants, and animals, are composites. It is new in the sense that only since the early 1960s has engineers and scientists exploited serious the vast potential of fabricated fibrous composite materials. The development of new composites and applications of composites has been accelerated. The textile structural composite cited in this study should be considered as typical of modern materials. As a well-known definition, a composite is a material composed of two or more distinct phases **Figure 2.1**. Thus, a composite is heterogeneous. The fibrous composites are materials in which one phase acts as a reinforcement of a second one. The second phase is called the matrix. The challenge is to combine the fibers and the matrix to form the most efficient material for the extended application.

Textile preforms are fibrous assembly with prearranged fiber orientation preshaped and often preimpregnated with matrix for composite formation. The microstructural organization of fibers within a preform, or fiber architecture, determines the pore geometry, pore distribution and tortuosity of the fiber paths within a composite. Textile preformsnot only play a key role in translating fiber properties to composite performance but also influence the ease or difficulty in matrix and consolidation. Textile preforms are the infiltration structural backbone for the toughening and net shape manufacturing of composites.

The flexible fibers, such as glass, carbon, and aramid, can be woven into textile fabric, which can then be impregnated with a matrix material. A wide variety of weave patterns are available. Plain woven composites or homogeneous orthotropic woven fabric (HOWF) composites are orthotropic materials which can be classified into two patterns, a plain weave (every fiber over and under every other perpendicular fiber) and a two-harness satin weave (under only every two fibers). Woven fabrics naturally have better in-plane transverse effective properties than unidirectional lamina. They lay better in structural configurations with substantial curvature and are more durable during handling.

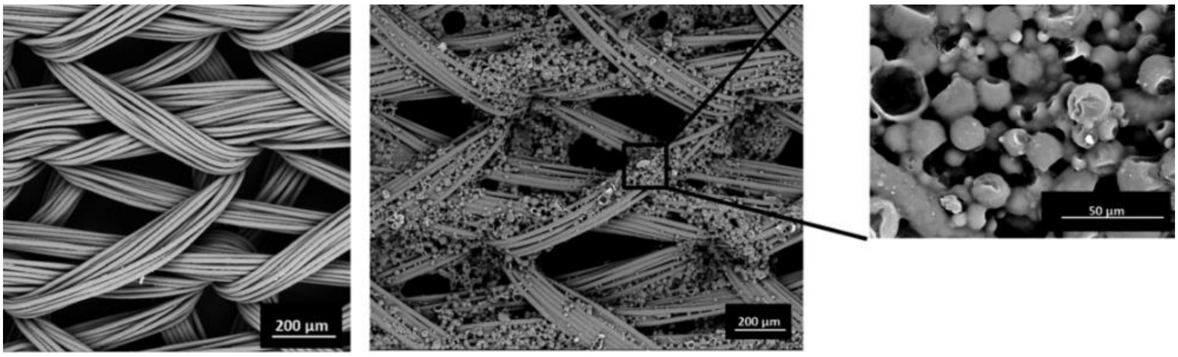

Figure 2.1 Multiphase Media [1]

In addition, a wide variety of fibers and matrix materials are now available for use. The selection of the specific fiber and matrix to be used in a composite is not arbitrary. The two (or more) phases of a composite must be carefully chosen for structural efficiency. The composite generally must be resistant to debonding at the fiber/matrix interface, and it must also be resistant to fiber breakage and matrix cracking. However, in application where it is desired to dissipate energy during the failure process (such as in crashworthy or impact-resistant structures), progressive fiber failure and fiber/matrix debonding (damage development) are positive features because they dissipate energy. Thus, a major challenge for the mechanical and metarial community is to understand the factors that affect damage development and to know how to design for it under severe environmental and mechanical loading conditions, including the fabrication phase as well as the in-service phase.

2.1.1 Fiber types

A wide variety of fibers is available. Glass fibers have been used since the 1930s; however, it was only in the late 1950s that fibers which exhibit significantly higher stiffness were developed for structural applications. These new high-specific stiffness (stiffness divided by density) and high-specific strength (strength divided by density) fibers are called advanced fibers. Composites made from them are called advanced composites. An in-depth discussion of fiber types and fabrication methods can be found in the book by Chawla K.K. [1].

As indicated in **Table 2.1**, different fibers have different morphology, origin, size, and shape. Some fibers, such as glass, carbon, and alumina, are supplied in the form of tows (also called rovings or strands) consisting of many individual, continuous fiber filaments.

Table 2.1 Typical Features of Fibers

Fiber Type		Origin	Fabrication	Filament (μm)	Filaments/ Tow
Glass	S-2 glass	Molten glass	Fiber-drawing	6-4	2000
Organic	Kevlar 49	Liquid Crystal	Spinning	12	1000
Carbon	AS4	PAN	Heat & stress	8	12,000
	P-100S	Pitch	Heat	10	2000
	IM8	PAN	Heat & stress	5	12,000
Ceramic	Boron	Tungsten core	CVD	142	1
	Nicalon (SiC)	Polymer Precursor	Pyrolysis	15	500
	SCS-6 (SiC)	Carbon core	CVD	127	1
	Alumina	Slurry mix	Spin and heat	20	1

The size of the individual filaments ranges from 3 to 147 μm ($0.1\text{x}10^{-3}$ - $5.8\text{x}10^{-3}$ in). The maximum use temperature of the fibers ranges from as low as 250^0C

(482^0F) to as high as 2000^0C (3632^0F); however, in most applications, the use temperature of a composite is controlled by the use temperature of the matrix.

Boron is a ceramic monofilament fiber manufactured by chemical vapor deposition of boron on a tungsten core. Thus the fiber itself is a composite. It has a circular cross section and has been produced over a wide range of fiber diameter (33 - 400 μm) with the typical boron fiber diameter being approximately 140 μm. This is a relatively large fiber diameter and results in lower flexibility, in particular because boron is a very britle material. The mismatch in the coefficient of thermal expansion of the tungsten core and the deposited boron results in residual stresses which develop during fabrication cool-down to room temperature.

Carbon filaments are made by controlled pyrolysis (chemical decomposition by heat) of a precursor material in fiber from such as polyacrylonitrile, rayon, or pitch by heat treatment at temperatures ranging from 1000 - 3000^0C, with the fiber properties varying considerably with the fabrication temperature. Individual carbon filaments have a diameter of 4-10μm. The small filament size and tow arrangement result in a very flexible fiber which can actually be tied into a knot without breaking the fiber. The modullus and strength of carbon fibers is controlled by the process, which consists of thermal decomposition of the organic precursor under well-controlled conditions of temperature and stress.

A second type of carbon fiber is made from a pitch precursor. The pitch fibers are made by spinning a petroleum-based product to form a pitch precursor. The cross section of carbon fibers is often noncircular. Indeed, many have the shape of a kidney bean. Carbon fibers have a heterogeneous microstructure consisting of numerous lamellar ribbons. The morphology is very dependent on the manufacturing process.

Glass fibers are available in a variety of froms: E-glass and S-2 (Owens-Corning Fiberglas Corporation) are the most common for structural applications. E-glass is used where strength and high electrical resistivity are required, and S-2 glass is used in composite structural applications which require high strength, modulus, and stability under extreme temperature and corrosive environments. Glass fibers are produced by drawing molten glass through numerous tiny orifices in a gravity-fed tank to form continuos fialaments which are gathered together in a strand or tow. This fabrication method results in individual filaments that are small in diameter, isotropic, and very flexible.

Alumina fibers are ceramics fabricated by spinning a slurry mix of alumina particles and additives to form a yarn which is then subjected to controlled heating. The most important feature of alumina fibers is their strength retention at high temperature.

Aramid is an organic fiber which is melt-spun from a liquid polymer solution. The Du Pont company developed these fibers and sells their product under the trade name Kevlar, four grades of Kevlar with varying engieering properties are available. The morphology of the fiber consists of radially arranged crystalline sheets resulting in anisotropic properties. The filaments are small in diameter (≈12μm) and partially because of this, very flexible.

Silicon carbide (SiC) is a ceramic fiber made by one of two methods. The first method consists of chemical vapor deposition of silicon and carbon onto a pyrolytic graphite-coated carbon core. This fiber (developed by AVCO Specialty Materials Co. in the United States and designated SCS-6) is very similar in size and microstructure to boron fiber. The SCS-6 fiber is relatively stiff in flexure, having a diameter of 140 μm (0.00556 in). The second method for producing silicon car-bide fibers is controlled pyrolysis of a polymeric precursor. This method results in filaments which are similar to carbon filaments in term of size (≈14μm, 0.00056 in) and microstructure. The diameter of a Nicalon filament is approximately one-tenth that of an SCS-6 fiber, and hence it is much more flexile.

Typical engineering properties of specific fibers are compared with the properties of structural and matrix materials in **Table 2.2**. The modulus and strength values are for tensile loading along the axis of the fiber. Possibly the most important properties given in **Table 2.2** are the specific stiffness, the specific strength, and the coefficient of thermal expansion. The specific stiffness and strength values normalized with those of aluminum.

Table 2.2 Properties of Engineering Materials, Fibers and Matrix

Material	**Density ρ,** (g/cm^3)	**Modulus E_L,** (GPa)	**Poisson's Ratio ν_L**	**Strength σ_L^M** (MPa)	**Specific Stiffness (E/ρ)/(E/ρ)$_{Al}$**	**Specific Strength $(\rho^M/\rho)/(\rho^M/\rho)_{AL}$**	**Thermal Expansion Coefficient α_L, μ/^{0}C**
			METALS				
Steel	7.8	200	0.32	1724	1.0	1.2	12.8
Aluminum	2.7	69	0.33	483	1.0	1.0	23.4
Titanium	4.5	91	0.36	758	0.95	1.2	8.8
			FIBERS (Axial Properties)				
AS4	1.80	235	0.20	3599	5.1	11.1	-0.8
T300	1.76	231	0.20	3654	5.1	11.5	00.5
P100S	2.15	724	0.20	2199	13.2	5.5	-1.4
IM8	1.8	310	0.20	5171	6.7	16.1	--
Boron	2.6	385	0.21	3799	5.8	8.3	8.3
Kevlar 49	1.44	124	0.34	3620	3.6	13.9	-2.0
SCS-6	3.3	400	0.25	3496	5.1	6.1	5.0
Nicalon	2.55	180	0.25	2000	2.8	4.4	4.0
Alumina	3.95	379	0.25	1585	3.7	1.9	7.5
S-2 Glass	2.46	86.8	0.23	4585	1.4	10.4	1.6
E-Glass	2.58	69	0.22	3450	1.05	7.5	5.4
Sapphire	3.97	435	0.28	3600	4.3	5.1	8.8
			MATRIX MATERIALS				
Epoxy	1.38	4.6	0.36	58.6	0.08	0.4	63
Polyimide	1.46	3.5	0.35	103	0.03	0.4	36
Copper	8.9	117	0.33	400	0.5	0.3	17
Silicon carbide	3.2	400	0.25	310	4.9	0.5	4.8

As indicated in **Table 2.2** advanced fibers exhibit a broad range of properties. Indeed, the properties of carbon fibers can vary significantly depending upon the fabrication process. The fiber data in **Table 2.2**, are for the fiber only, with the loading along the fiber axis. These properties are reduced significantly when the fiber is used with a matrix material to form a composite. The specific properties are reduced even further when the loading is in a direction other than along the fibers. Nevertheless, actual experience has shown that significant weight savings are possible in primary engineering structures through the use of advanced composites. As will be discussed later in this chapter, weight is not the only reason for choosing composites; indeed, for some applications composites are chosen when there is a weight penalty, but there are other advantages such as heat transfer characteristics or noncondutive properties which are more important.

2.1.2 Matrix Materials

There are some materials including polymers, metal and ceramics are used as matrix materials in continuous fiber composites. Polymeic matrix materials can be further subdvided into thermoplastics and thermosets. The thermoplastics soften upon heating and can be reshaped with heat and pressure. Thermoplasyic polymers used for composites include polyphenylene sulfide (PPS), and polysulfone. The thermoplastic composites offer the potential for higher toughness and high volume, low cost processing. They have a useful temperature range upwards of 225^0C (437^0F). Thermoset polymers become cross linked during fabrication and do not soften upon reheating. The most comom thermoset polymer matrix materials are polyesters, epoxies, and polyimides. Polyesters are used extensively with glass fibers. They are inexpensive, are lightweight, have a useful temperature range up to 100^0C (212^0F), and are somewhat resistant to environmental exposures. Epoxies are more expensive but have better moisture resistance and lower shrinkage on curing. Their maximum use temperature is in the vicinity of 175^0C (347^0C). Polyimides have a higher use temperature (300^0C, 572^0F) but are more difficult to fabricate.

The most common metals used as matrix materials are alumium, titanium, and copper. Reasons for choosing a metal as the matrix material include higher use temperature range, higher transverse strength, toughness (as contrasted with the brittle behavior of polymers and ceramics), the absence of moisture effects, and high thermal conductivity (copper). On the negative side, metals are heavier and more susceptible to interfacial degradation at the fiber/matrix interface and to corrosion. Aluminum matrix composites have a use temperature upwards of 300^{0}C (572^{0}F), and titanium can be used at 800^{0}C (1470^{0}F). Essentially all materials exhibit degradation of properties at highest temperatures. The main reasons for choosing ceramics as the matrix include a very high use temperature range (>2000^{0}C, 3600^{0}F), high elastic modulus, and low density. The major disadvantage to ceramic matrix materials is their brittleness, which makes them susceptible to flaws. Carbon, sillicon carbide, and silicon nitride are ceramics that have been used as matrix materials.

Carbon/carbon is a compositte that consists of carbon fibers in a carbon matrix. The primary advantage of this material is that it can withstand temperature in excess of 2200^{0}C (4000^{0}F). The disadvantage of caron/carbon composites is that their fabrication is an expensive, multistage process. Thus this material is used only where its high temperature capabilities are essential for the application.

2.1.3 Composite Properties

Table 2.3 presents typical average or effective properties for unidirectional composites. The designation of the different composites consists of the name of the fiber followed by the name of the matrix. Unidirectional fibrous composites exhibit different properties in different directions. This is reflected in **Table 2.3** by the labels axial and transverse, which refer to properties in the direction of the fiber (axial) and the properties perpendicular to the fiber (transverse). The properties of a unidirectional composite are also a function of the volume fraction of fibers.

Table 2.3 Typical properties of unidirectional composites (Chawla K.K. [1])

Material	**AS4/ 3501-6**	**T300/ 5208**	**Kevlar/epoxy**	**Boron/Al**	**SCS-6/ Ti-15-3**	**S-2 glass/ Epoxy**
Density, g/cm^3	1.52	1.54	1.38	2.65	3.86	2.00
Axial modulus E_1, GPa	148	132	76.8	227	221	43.5

Transverse modulus E_2, GPa	10.50	10.8	5.5	139	145	11.5
Poisson's ratio ν_{12}	0.30	0.24	0.34	0.24	0.27	0.27
Poisson's ratio ν_{23}	0.59	0.59	0.37	0.36	0.40	0.40
Shear modulus G_{12}, GPa	5.61	5.65	2.07	57.6	53.2	3.45
Shear modulus G_{23}, GPa	3.17	3.38	1.4	49.1	51.7	4.12
Modulus ratio E_1/E_2	12.6	12.3	14.8	1.6	1.5	4.6
Axial tensile strength χ_τ, MPa	2137	1513	1380	1290	1517	1724
Transverse tensile strength Υ_τ, MPa	53.4	43.4	27.6	117	317	41.4
Strength ratio χ_τ/Υ_τ	27	35	50	11	4.8	42
Axial CTE α_1, $\mu/^0C$	-0.8	-0.77	-4	5.94	6.15	6.84
Transverse CTE α_2, $\mu/^0C$	29	25	57	16.6	7.90	29
Fiber volume fraction V_f	0.62	0.62	0.55	0.46	0.39	0.60
Ply thickness, mm	0.127	0.127	0.127	0.178	0.229	

2.1.4 Advantages of composite

The initial development and application of advanced fibrous composites were pursued primarily because of the potential for lighter structures. The first applications in the early 1960s were in aerospace structures, where weight critically affects fuel consumption, performance, and pay load, and in sports equipment, where lighter equipment often leads to improved performance. Today fibrous composites are often the materials of choice of designers for a variety of reasons, including low weight, high stiffness, high strength, electrical conductivity low thermal expension, low or high rate of heat transfer, corrosion resistance, longer fatigue life, optimal design, reduced maintenance, fabrication to net shape, and retention of properties at high operating temperature.

The first advanced feature of composite is its specific stiffness and specific strength. Undoubtedly the most often cited advantage of fibrous composites is their high specific stiffness and high specific strength as compared with traditional engineering materials. These properties lead to improved performance and reduced erergy consumption, both vitally important in the design of almost all engineering structures. Because composites are fabricated, they can be engineered to meet the specific demands of each particular application. Available design options include the choice of materials (fiber and matrix), the volume fraction of fiber and matrix, fabrication method, layer orientations, number of layers in a given direction, thickness of individual layers, type of layer (unidirectional or fabric), and the layer stacking sequence. This vast array of design variables for composites contrasts sharply with more traditional engineering materials, where the choices are much more limited. The availability of a wide array of structured materials means that more efficient structures can be fabricated with less material waste. Composites can be designed to have the desired properties in specified directions without overdesigning in other directions.

The fatigue lives of several composites are found out to that the material can withstand under tensile stress. Clearly, composites exhibit much better resistance to fatigue than does aluminum. This can be critical in structures such as aircraff, where fatigue life is often the most important design consideration. Improved fatigue life is one of the major reasons why there has been a shift to composites by the aircraft industry. Fatigue life is also important for many other structures that experience cyclic loading, such as transportation vehicles, bridges, industrial components, and structures exposed to variable wind or water loading.

For the dimensional stability, it is seen that nearly all structures are exposed to temperature changes during their lifetimes. The strains associated with temperature change can result in changes in size or shape, increased friction and wear, and thermal stresses. In some applications these thermal effects can be critical. Increased friction between moving parts can result in failure because of overheating. Thus, there are many applications where a zero or near zero-CTE material can result in significant bebefits. Through proper design, it is possible to have zero-CTE composites or to design the CTE of the composites to match that of other components to minimize thermal mismatch and the resulting thermal stresses.

Polymer and ceramic matrix materials can be selected to make composites resistant to corrosion from moisture and other chemicals. Current applications of glass fiber composites that have been driven by corrosion considerations include filament wound underground storage tanks, strutural members for offshore drilling platforms and chemical plants, sucker rod used in pumping oil from wells, pipe, and domestic applications including doors, window frames, and deck funiture in coastal regions where saltwater corrosion is a major problem.

Polymeric and ceramic matrix composites can often be made to be essentially maintenance free compared with traditional engineering materials. This is true primarily because of the corrosion resistance. Reduced maintenance can represent substantial savings and should be considered in all total cost evaluations. Unfortunately, all too often, cost decisions are based primarily on the intitial capital expenditure without regard for the total lifetime cost of maintaining the structure. Corrosion resistance results in longer life of a structure and hence reduced replacement cost.

Composite structures can be fabricated efficiently through the use of automated methods such as filament winding, pultrusion, and tape laying. Efficiencies in fabrication can also be achieved because composites can be fabricated with very little material waste. In many case, composite components can be fabricated exactly to size specifications with no materials waste. This is in stark contrast to the use of metals, where it is often necessary to “hog out” large portions of material to arrive at the final configuration. Fabrication costs also are directly related to the number of parts in a structure. The use of composites can be substantially reduced this number because of the ability to fabricate to net shape and because of the use of bonded rather than riveted joints. As an example, two sections of a fuselage were made by riveting aluminum components and adhesively bonding compositte components. The number of parts in the aluminum structure was 11000, whereas the composite structure had only 1000. This tenfold reduction represents a significant saving in both the cost of components and the cost of assembly.

It is desirable that many engineering structures be elctrically nonconducing. Excellent examples are the glass/polyester ladders and booms which have replaced steel and aluminum in order to reduce the possibility of electrocution. Nonconducting components are also important for applications in the electronics industry, whether it be a computer chip or the entire building in which the chips are fabricated. In contrast, copper matrix composites are now under consideration for high temperature applications because of the high thermal conductivity of copper. Copper matrix composites can serve as radiators in regions where it is necessary to maintain lower temperature. It is noteworthy that the fiber glass ladders and the copper matrix composites are chosen even though there is a weght penalty. In evaluating the cost competitiveness of structures made from composite materials the total life time cost should be included. Per pound, composites are usually more expensive than traditional materials; however, many other factors must be included in a meaningful cost comparison. First, fever pounds of composite material are requred because of the higher specific stffness and strength. Second, it is possible that fabrication costs can be lower. Third, transportation and erection costs are generally lower for composite structures. Finally, the composite structure will generally last much longer than the traditional material and will requie much less maintenance during its life. Composite materials have been shown to be cost competitive in a wide variety of aerospace, automotive, industrial, domestic, oil drilling, and elactronic applications, among orthers.

2.2 Practical applications of inflating composite structures

Advanced lightweight laminated composite structural elements are increasingly being introduced to new designs of modern aerospace structures for enhancing their structural efficiency and performance. The introduction of new fiber materials, such as glass, carbon or aramid fibers with orthotropic material behavior have motivated a deep study of such elements which are used to build membrane and thin shell structures.

Inflating structures are membrane components made of elastic/plastic fabric textiles that are inflating by using air pressure to maintain the shape and stiffness of these structures. Advantage of inflating beams is to be able to absort impact loads, toughness and easy assembly, light weight and require little space for storage. Low manufacturing cost is also an effective factor in industrial application.

2.2.1 Aerospace

In recent years, developments in space technologies have focused on reducing the prohibitive costs of space missions Veldman [2]. In the space industry, initiatives a re currently underway that seek to unlock the cost-saving potential of recent breakthroughs in materials science. Specifically, these research initiatives hope to achieve significant reductions in launch mass and volume of orbital payloads by replacing conventional spacecraft materials with new ultra-light alternatives. In this regard, inflating technology is a promising solution for deploying large systems in space. They are well suited for application in a variety of large space systems including: One of the earliest applications of inflating structures in the space is the project of inflating satellites Veldman [2]. NASA scientists are now using inflating technology to build a telescope that is nearly twice as large as Hubble (The first space telescope launched) but that weight only about one-sixth as much as Hubble. This telescope would be made using the inflating technology. Some examples on the use of composite materials on aerospace are illustrated in **Figures 2.2** to **2.5**.

Inflating habitats are under development for an orbit use, during the passage between planets and on planetary surfaces. The inflating buildings in the shape of torus or dome are proposed in the Martian colony project. The first of these inflating space habitats, called TransHab, was proposed for the International Space Station (by NASA). Nowadays, inflating structures are scalable and reconfigurable to fit a wide range of applications from small gun-launched munitions to large high altitude long endurance (HALE) aircraft. Due to the unique requirements for flight such as high aspect ratio and unconventional airfoil profiles due to the low density and high aerodynamic efficiency, this places significant constraints on inflating wing designs for use in such vehicles.

Figure 2.2 30 meter ECHO I Balloon Satellite [2]

Figure 2.3 ARISE inflating telescope [2]

Figure 2.4 Inflating lunar habitat proposal [2]

Figure 2.5 Inflating aircraft [2]

2.2.2 Civil engineering and architecture

The first pneumatic building proposal is attributed to Frederick William Lanchester, an English engineer, who patented a design for a field hospital in 1917. This fabric tent without poles or conventional structure was to be supported by low air pressure and entered by means of air locks. In 1942, prompted by the demands of the War Production Board (USA), many inflating buildings have been produced. In the recent decades inflating shelters arc used by the assisting authorities in case of major accidents such as emergency shelters after natural disasters **Figure 2.6a**, decontamination regions, tents for Red Cross **Figure 2.6c**, Police, Civil Defence and Military (as storage hangars for airplanes or vehicles) etc. Many inflating churches **Figure 2.6b**, mosques, synagogue etc. have also constructed nowadays. This technology has reduced the transportable weight of a tent by 66%, the transportable volume by 75% and the setup time by 50% and it is a point that the payload and the optimum shape for a specific application become the central preoccupation for designers. Likewise, many membrane inflating structures have been constructed in the civil Engineering field: the roof of inflating stadiums such as the Carrier dome (USA) in 1980 **.7a**, the BC Place stadium (Canada) in 1983 **.7b** the dome Tokyo (Japan) in 1988 **.7c**, etc.

(a) Inflatable tent (b) Inflatable church (c) Inflatable hospital

Figure 2.6 Inflating structures in Civil Engineering and Architecture [1]

(a) (b) (c)

Figure 2.7 Inflating stadiums [1]

2.2.3 Other fields of application

In addition to the fields referred above, the inflating structures find their applications in many other fields such as: Marine and submarine applications, farming field, etc. The popularity of inflating structures is due to the fact that they are very efficient light weight structures. Thus a thorough understanding of the stability behavior of this type of structures is a must for all those who employ them. Unfortunately, very little relevant references have been found on buckling of inflating structures made of plain woven composites. Moreover, based on the review on literature, it could be observed that constructing an effective analysis model for inflating structures is essential.

2.3 Analyses of inflating structures

2.3.1 Analytical approach

The studies on behaviour of inflating structures have bees widely conducted by various researchers by using the analytical approach. Some authors have also applied Euler Bernoulli’s kinematics to modelling the inflating beams. For example, load deflection theory was derived Comer, R. L., & Levy, S. [3] for an inflating isotropic beam. After that, Comer and Levy’s work was extended by Webber, J.P.H. [4] to predict distructing loads in cantilever beams that was inflating. Also, Main et al. [5] did experiments on a cantilever isotropic beam and then Comer’s theory was improved typically. Continuously, Suhey et al. [6] considered a tube pressurized under uniformly distributed loads. By the means of the Euler-Bernoulli's kinematics, material of beams was supposed to be isotropic and their results was obtained theoreticaly for deflection. The Timoshenko's kinematics is determined by some other authors have that it is the best adapted theory for structures as pressure load does not appear in solution of deflection, which is mentioned in the Euler Bernoulli's kinematics situation. For instance, a seri of nonlinear equations was derived by Fichter [7] for the bending and twisting of inflating cylindrical beams. This derivation was based on three following significant assumptions: cross section of the inflating beam, which is the first issue, remains undeformed under the applied loading; secondly, the cross-sectional translation and rotations are small; and the negligible characteristic of circumferential strain is the third assumption. He used the Timoshenko kinematics and energy minimization approach. A homogeneous isotropic fabric is supposed to apply on the beam. Later Topping, A.D. [8] and Douglas, W.J. [9] have investigated the structural stiffness of an inflating cylindrical cantilever beam that was influenced by large deformations. The finite theory of elasticity and the theory of small deformations have been employed to obtain explicit analytical results. Their analyses also account for the changes of geometry and material properties that occur during the inflation process. Wielgosz and Thomas [10] have derived analytical solutions for inflating panels and tubes by using the Timoshenko kinematics and by writing the equilibrium equations in the deformed state of the isotropic beam in order to take into account the geometrical stiffness and the follower force effect due to the internal pressure. They have shown that the limit load is proportional to the applied pressure and that the deflections are inversely proportional to the material properties of the fabrics and to the applied pressure. Wielgosz and Thomas [10] and Thomas and Wielgosz [11] have presented experimental, analytical and numerical results on the deflections of highly inflating fabric tubes submitted to bending loads. Experiments have been displayed and they have shown that the tube behaviour looks like that of inflating panels. Equilibrium equations have been once again written in the deformed state to take into account the geometrical stiffness and the follower forces. Comparisons between experimental and analy tical results have proven the accuracy of their beam theory for solving problems on the deflections of highly inflating tubes. Le and Wielgosz [12] have used the virtual work principle in Lagrangian form and the usual Saint Venant Kirchhoff hypothesis with finite displacements and rotations in order to derive the nonlinear equations for inflating isotropic beams. The nonlinear equilibrium equations have been linearized around the pre-stressed reference configuration which has to be defined as opposed to the so-called natural state. These linearized equations have improved Fichter's theory.

Although a lot of research groups have made much efforts in developing the analytical methods over many years but almosts they have focused on isotropic fabric materials. Until now, there has a few work that focuses on the case of orthotropic fabric material.

2.3.2 Numerical approach

Nowadays, inflating beams pose significant challenges to the analysts, especially in cases where the analytical solutions are difficult to find in gernalized cases of loadings and boundary conditions. In the numerical modelling of inflating beams, significant prior researches have been conducted. Steeves has used the principle of minimum potential energy to derive a set of governing differential equations for lateral deformation of inflating beams. A simplifying approximation, assuming that the cross sections of the beam remain undeformed, has then been employed to reduce the dimensions to one dimension: This beam element has included a pressure stiffening term. Quigley et al. and Cavallaro et al. [13] have used the finite element approach to predict the linear load-deformation response of inflating fabric beams. However, the pressure stiffening term in Steeves's element has treated the axial pressure resultant as an externally applied stiffening tension force. This formulation has predicted an unbounded increase in beam stiffness with increasing inflation pressure. Wielgosz and Thomas [10, 14] and Thomas and Wielgosz [11] have studied the load-deflection behaviour of highly inflating fabric tubes and panels, and have developed a specialized beam finite elementingusing

Timoshenko beam theory. In their approach, the force generated by the internal pressure has beeen treated as a follower force which has accounted for pressure stiffening effects. However, the element formulation did not consider the fabric wrinkling. Bouzidi et al. [15] have presented theoretical and numerical developments of finite elements for azisymmetric and cylindrical bending problems of pressurized isotropic membranes. The external loading has been mainly a normal pressure to the membrane and the developments have been made under the assumptions of follower forces, large displacements and finite strains. The total potential energy has been minimized, and the numerical solution has been obtained by using an optimization algorithm. Suhey et al. [6] have presented a numerical simulation and design of an inflating open-ocean-aquaculture cage using nonlinear finite elementinganalysis of isotropic membrane structures. Numerical instability caused by the tension-only membrane has been removed by adding an artificial shell with small stiffness. The finite elementing model has been compared with a modified beam theory for the inflating structure. A good agreement has been observed between the numerical and theoretical results. Le and Wielgosz [16] have discretized the nonlinear equations obtained in Le and Wielgosz [12] to carry out a finite element formulation for linearized problems of highly inflating isotropic fabric beams. Their numerical results obtained with the beam element have been shown to be close to their 3D isotropic fabric membrane finite elementingand analytical results obtained in Le and Wielgosz. [12]. Davids [17] and Davids and Zhang [18] have derived a Timoshenko beam finite elementingfor nonlinear load-deflection analysis of pressurized isotropic fabric beams and the numerical examination of the effect of pressure on the beam loaddeflection behaviour. The basis of their element formulation has been an incremental virtual work ezpression that has included explicitly the work done by the pressure. Parametric studies have been also investigated to demonstrate the importance of including the work done by the pressure in their models. More recently, Malm et al. [19] have used 3D isotropic fabric membrane finite elementing model to predict the beam load-deformation response. Comparison between the finite elementing model load-deflection responss and beam theory has shown the accuracy of the conventional beam theory for modelling the isotropic fabric airbeam. Most of the former works, the fabric was always supposed to be isotropic. Considering the inflating beams made of orthotropic fabric materials, several research groups have been conducted, Plaut et al. [20] have studied the effect of the snow and wind loads on an inflating arch in the assumption of linear thin-shell theory of Sanders. They have used this theory to formulate the governing equations, which include the effect of the initial membrane stresses. The material was assumed to have a linearly elastic, nonhomogeneous and orthotropic behaviour. Approzimate solutions have been obtained using the Rayleigh-Ritz method. Plagianakos et al. [21] have studied a low pressure Tensairity in order to estimate its potential towards applications including axial compressive loads. Compression experiments have been conducted on a simply-supported spindle-shaped Tensairity column and displacements have been measured in several positions along the span, whereas axial forces have been experimentally determined by strain gauges measurements. Comparisons has been made between experimental results, finite elementingand analytical predictions they have already developed, and a good agreement has been found. Moreover, Nguyen et al. [22] studied an analytical approach to approximate the critical load for an HOWF 3D Timoshenko. Regarding the buckling behavior, the model of proposed inflatable beam proved a prosperity adjustment with the previous models in literature. The total Lagrangian form of Timoshenko kinematics and virtual work principles were applied to formulate the beam’s governing equations.

Overall, it is seen that a great number of studies have been conducted recently to development of numerical model to the infalting beam structures, the study on the influence of orthotropic fabric on the structural behaviour has not been handled yet. Moreover, all previous studies only developed based on traditional finite element approach, which could be not suitable for infalting structures with curve geometries and those require high-order continuity of interpoaltion functions.

The IGA approach was firstly introduced by Hughes in [23]. Since then, it quickly becomes a hit in many fields of computational mechanics, where its efficiency compared to traditional Finite Element Analysis (FEA) was proven. The fundamental concept of the IGA is to bridge the gap between the methods for analysis and conventional computer-aided design tools using NURBS basis functions. Therefore, the time taken from preliminary designs to analysis progress is reduced considerably while exact geometries of the modelled objects are preserved. The compelling advantages of the IGA have been proved through a large number of publications for plate problems. Having distinguished features, the NURBS basis functions are capable of providing a smooth and high continuity interpolation, which allows to construct the elements in a straightforward manner. Over ten years of development, IGA is still the topic of interest. J.A. Cottrell [24] investigated structural vibration, linear and nonlinear analysis of structures, shape structural optimization Wolfgang A. Wall [25], thin shell structures Kirchhoff-Love Kiendl [26]; Nguyen-Thanh [27], Reissner-Mindlin shell Benson [28]; Thai [29], laminated composite plates based on layer-wise theory Thai [30] and rotation-free Benson [31]. There are research groups over the world working on IGA. In Vietnam, Professor Hung Nguyen-Xuan and colleagues are pioneers in this area with several publications using IGA for analysis of static, vibration and stability of Reissner-Mindlin plates. Thai [29] and Thai [30] investigated behavior of laminated composites based on higher-order shear defomation theory and layer-wise theory in the IGA framework. Tran [32] and Nguyen-Xuan [33] studied FGM plates using IGA and higher-order shear theory. However, in the best knowledge of author, there is still lack of studies using IGA for inflating structures, especially stability of inflating beams and plates.

2.4 Conclusions

In this chater, an overview of fibous composite materials is presented. Thanks to its advanced mateiral properties, the fibous composite materials have been widely applied in various fileds in industrial and science applications. In the filed of structural engineering, the materials are most used for inflating structures.

The literature review shows that the most widely used approach to analyze the structural responses of inflating structures is the analytical approach. However, most of previous reseach only forced on the isotropic materials. Only a few studies have been conducted for orthotropic materials. In addition, the use of numerical approach to solve the problems are also limited. This is the main motivation for this research, which will focus on investigating the structural behaviour of composite fabric inflating structures in both experimental and numerical manners.

CHAPTER 3: THEORETICAL FORMULATIONS

3.1 Overview and basics of Isogeometric Analysis

Designers have long used computers for their calculations. Initial developments were carried out in the 1960s within the aircraft and automotive industries. It's the beginning of CAD, also known as CADD (Computer Aided Design and Drafting). Some of the mathematical description work on curves was developed in the early 1940s and the most efficient one is NURBS, can represents not only free-form curves but also surfaces and solids in three-dimensional space, appeared in at the end of 1980s. Designers now generate CAD files and these must be translated into analysis-suitable geometries, meshed and input to large-scale finite elementinganalysis codes. When engineering designs are becoming increasingly more complex, it is obvious that engineering design and analysis could not be separate endeavors. Design of sophisticated engineering systems is based on a wide range of computational analysis and simulation methods, including structural mechanics, fluid dynamics, acoustics, electromagnetics, heat transfer, etc. Design and analysis intercommunicate each other closely. However, analysis-suitable models are not automatically created or readily meshed from CAD geometry. Although meshing process is not always appreciated in the academic analysis community, there are many time consuming, preparatory steps involved.

The integration of CAD and CAA (analysis is usually referred to as CAA, which stands for Computer Aided Analysis) is a key for this problem. The process has been proven a formidable problem and seems that fundamental changes must take place to fully integrate engineering design and analysis. Recent trends taking place in engineering analysis and high-performance computing are also demanding greater precision and tighter integration of the overall modeling-analysis process. A finite elementingmesh is only admitted as an approximation of the CAD geometry. In most of the cases, this approximation creates errors in analytical results. Automatic adaptive mesh refinement has been conceived as widely adopted in industry. And it is necessary to study extensively in academic literature, because mesh refinement requires access to the exact geometry. Hence, automatic communication with CAD which can represent geometry accurately is an important duty.

An overview of NURBS theory focusing on the mathematical description of free-form curves is reviewed in this chapter. Most of the basics of IGA and more details on NURBS-based modelling can be found in the books of Piegl [34] and [35]. Non-Uniform Rational B-Spline (NURBS) was developed from Bézier curves and surfaces which were proposed in the late 1960s and early 1970s. NURBS curves can represent precisely a wide range of geometry, especially conic sections. NURBS-based geometry has great advantages in flexibility and precision, and hence nowadays becomes the standard for geometric modelling in computer aided design (CAD). This chapter starts with a short review of Bézier curves that is the antecedent of B-Spline geometry. B-Spline curves are then explained in details since most of the definitions and properties of B-Splines apply to NURBS. Finally, NURBS as a generalization of B-Splines is presented.

3.1.1 Advantages of IGA in comparison with FEM

Ther are some advantages between IGA and conventional FEM briefly addressed as followings: computing domain, firstly, stays preserving at any level of domain discretization and no matter how coarse it is. In the context of connecting mechanics, this leads to the simplification of connecting detection at the interface of two connecting surfaces, especially in the large deformation circumstance where the relative position of these two surfaces usually changing. Additionally, a sliding joint between surfaces can be reproduced precisely and accurately. This is also beneficial for problems that are sensitive to geometric imperfections, for example, shell buckling analysis, boundary layer phenomena, and fluid dynamics analysis.

Secondly, NURBS based CAD models make the mesh generation step is done automatically without the need for geometry clean-up or feature removal. This can lead to a dramatical reduction in time consumption for meshing and clean-up steps, which account approximately 80% of the total analysis time of a problem Cottrell [36].

Thirdly, the need to communicate with CAD geometry causes effortless and less time-consuming of mesh refinement. This advantage repulses same basis functions which are utilized for both modeling and analysing processes. It can be steadily indicated that the partition of geometry position and the mesh refinement of the computating domain are simplified to knot insertion algorithm, which is performed automatically. These partitioning segments then become new elements and the mesh is exact entirely.

Finally, inter-element regularity higher with the maximum of C^{p-1}in the absence of repeated knots makes the naturally suitable method for mechanics problems. The higher-order element derivatives in formulations as Kirchhoff-Love shell, gradient elasticity, Cahn-Hilliard equation of phasing separation… This results from directly utilizating of B-spline/NURBS are based on analysing calculation. In contrast with FEM's basis functions, which are defined locally in the element's interior with C^0 continuity across element boundaries (and thus the numerical approximation is C^0), IGA's basis functions are not located in one element (knot span). Insteadly, they are usually defined over several contiguous elements which guarantee a greater regularity and interconnectivity. Therefore, the approximation is highly continuous. Furthermore, one another benefit of this higher smoothness is the greater convergence rate in comparison with conventional methods, especially combination of a new type of refinement technique which called *k*-refinement. Nevertheless, it is worthy to mention that the larger support of basis does not lead to bandwidth increment in the numerical approximation and thus the bandwidth of resulted sparse matrix will be retained in the classical FEM's functions.

3.1.2 Disadvantages of IGA

This methodology, however, presents some challenges that require special treatments.

The most significant challenge of making use of B-splines/NURBS in IGA is that its tensor producing structure does not permit a true local refinement. Any knot insertion will lead to global propagation across computational domain.

Due to the lack of Kronecker delta property, in addition, the application of in-homogeneous Dirichlet boundary condition or forces/physical data exchange in a coupled analysis are highly involved.

Furthermore, owing to the larger support of the IGA's basis functions, the resulted system of matrix is relatively denser (containing more non-zero entries) when it compares to the FEM and tri-diagonal banding structure as well.

3.1.3 Bézier Curves

The Bézier curves is a parametric polynomial curve which is defined as a product of the coordinate functions and control points, which are not interpolated but approximated, see **Figure 3.1**. Mathematically, a parametric Bézier curve is defined by the linear combination of basis functions and control points, as follows Wolfgang [25].

$$\mathbf{C}(\xi) = \sum_{i=1}^{n} B_{i,p}(\xi)\mathbf{P}_i \qquad 3.1$$

where n is the number of *control points* $p+1$ and $B_{i,p}(\xi)$ are the Bernstein polynomials of polynomial degree *p*. The polynomial degree is related to the number of control points by: $p = n-1$. The Bernstein polynomials are defined by:

$$B_{i,p}(\xi) = \frac{n!}{i!(n-i)}(\xi)^i(1-\xi)^{n-i} \qquad 3.2$$

which requires that $\xi \in [0,1]$.

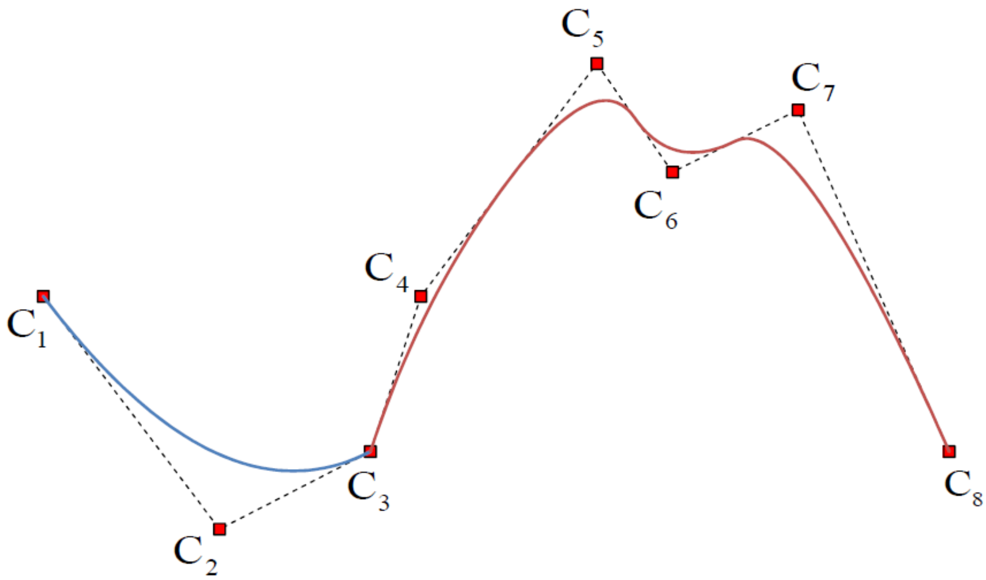

Figure 3.1 An example of B-spline curve

The Bézier curves have the following disadvantages Kiendl [26]: a high degree is required in order to increase number of control points; with increasing polynomial degree, the Bézier curves are inefficient to process and the algorithms are numerically instable; although Bézier curves can be shaped by means of their control points, the control is not sufficiently local; there is no point of reduced continuity which can be inserted inside the curve. These problems can be overcome by using B-Splines.

3.1.4 B-Spline

Similar to Bézier curves, B-Spline curves are defined by a linear combination of controling points with basis B-Splines functions over a parametric space. The parametric space is divided into interval parts and the B-Splines are defined piecewise on these intervals with certain continuity requirements between the intervals. Since the number of intervals is arbitrary, the polynomial degree can be chosen independently out of the number of control points. Therefore, a large set of data points can be approximated by using low polynomial degree. The parametric space is defined by the so-called *knot vector*.

3.1.4.1 Knot Vector

The knot vector is a set of non-decreasing real numbers representing coordinates in parametric space:

$$\Xi = \left\{ \xi_1, \xi_2, \xi_3, ..., \xi_{n+p+1} \right\} \tag{3.3}$$

where $\xi_i \in \mathbb{R}$ is the i^{th} knot, i is the knot index, $i = 1, 2, ..., \mathrm{n+p+1}$, p is the polynomial degree and *n* is the number of basis functions. The intervals $\left[\xi_1, \xi_{n+p+1}\right]$ and $\left[\xi_i, \xi_{i+1}\right]$ are called a *patch* and a *knot span*, respectively. A B-Spline basis function is C^{∞} continuous inside a knot span, and C^{p-1} continuous at a single knot. A knot value can be repeated more than once and is then called a multiple knot. If all knots are equally spaced in the parametric space, the knot vector is called *uniform, and non-uniform vice versa.* A knot vector is said to be *open* if the first and the last knot have the multiplicity $p+1$. In a B-Spline with an open knot vector, the first and the last control points are interpolated and the curve is tangential to the control polygon at the start and the end of the curve.

3.1.4.2 B-Spline Basis Functions

B-Splines basis functions $N_{i,p}\left(\xi\right)$ of degree $p \geq 0$ are defined by the Cox-deBoor recursive formula Thai as follows:

$$N_{i,0}\left(\xi\right) = \begin{cases} 1 & if\, \xi_i \leq \xi_{i+1} \\ 0 & otherwise, \end{cases} \tag{3.4}$$

$$N_{i,p}\left(\xi\right) = \frac{\xi - \xi_i}{\xi_{i+p} - \xi_i} N_{i,p-1}\left(\xi\right) + \frac{\xi_{i+p+1} - \xi}{\xi_{i+p+1} - \xi_{i+1}} N_{i+1,p-1}\left(\xi\right) \tag{3.5}$$

Important properties of B-Spline basis functions are:

Partition of unity, i.e. $\sum_{i=1}^{n} N_{i,p}\left(\xi\right) = 1$

Non-negativity, i.e. $N_{i,p}\left(\xi\right) \geq 0$

Local support, i.e. $N_{i,p}\left(\xi\right)$ is non-zero only in the interval $\left[\xi_i, \xi_{i+p+1}\right]$

Linear independence, i.e. $\sum_{i=1}^{n} \alpha_i N_i^p\left(\xi\right) = 0 \Leftrightarrow \alpha_{i,j} = 0$

Examples of quadratic and cubic B-Spline basis functions for open, non-uniform knot vectors are presented in **Figure 3.2**.

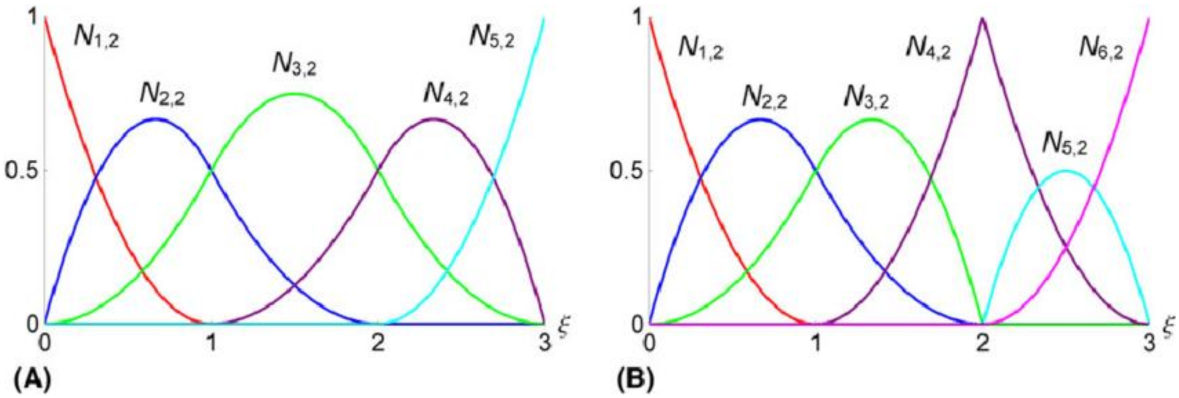

Figure 3.2 (a) Examples of Quadratic B-spline basis functions

The derivatives of the B-Spline basis functions are computed by the following formula Wolfgang [25]:

$$N_{i,p}^{(k)} = \frac{p}{p-k}\left(\frac{\xi-\xi_i}{\xi_{i+p}-\xi_i}N_{i,p-1}^{(k)} + \frac{\xi_{i+p+1}-\xi}{\xi_{i+p+1}-\xi_{i+1}}N_{i+1,p-1}^{(k)}\right) with \qquad k=0,\dots,p-1 \qquad 3.6$$

3.1.4.3 B-Spline Curves

A B-Spline curve of p order is defined by a tensor product of B-spline basis functions and control points, as follows:

$$\mathbf{C}(\xi) = \sum_{i=1}^{n} N_{i,p}(\xi)\mathbf{P}_i \qquad 3.7$$

The control points $P_i \in \mathbb{R}^d, i = 1,2,\dots,n$ are points in d-dimensional physical space $\mathbb{R}^d$, and construct the *control polygon*. In **Figure 3.3** a quadratic B-Spline curve with open knot vector is given. As can be seen, the first and last control point are interpolated and the curve is tangential to the control polygon at its start and end. The derivative of a B-Spline curve is also a B-spline curve which is computed by the following formula T.J.R. Hughes [23]:

$$C^{(k)}(\xi) = \sum_{i=0}^{n-k} N_{i,p-k}(\xi)P_i^{(k)} \qquad 3.8$$

$$P_i^{(k)} = \begin{Bmatrix} P_i & k=0 \\ \dfrac{p-k+1}{u_{i+p+1}-u_{i+k}}\left(P_{i+1}^{(k-1)} - P_i^{(k-1)}\right) & k>0 \end{Bmatrix} \qquad 3.9$$

Some important characteritics of B-spline curves are:

- Convex hull property: the inside curve contained in the convex hull of controling polygon.
- The controling points are generally not interpolated.
- The controling points influences on maximum $p+1$ sections.
- For open knot vectors, the first and last controling point are interpolated. The curve is tangential to the controling polygon at the beginning and the end of the curve. The C^{∞} continuous curve between two knots and continuous C^{p-k} at one knot having multiplicity *k*.
- Affine transforming of the B-Spline curve are performed correspondingly by transforming the controling points.
- A Bézier curve is also a B-Spline curve but with only one interval knot.

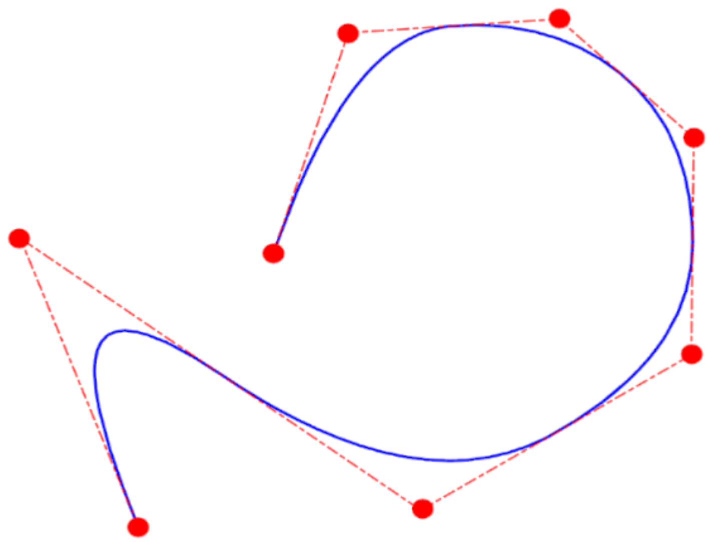

Figure 3.3 B-Spline, piecewise quadratic curve in $\mathbb{R}^2$ and corresponding control polygon

3.1.5 NURBS Curves

NURBS is abbreviation for Non-Uniform Rational B-Splines. In term of non-uniform, it refers to knot vector which is generally unchanged. Other term named rational term shall refer to the basis functions. For B-Splines, the basis functions are known as incoherent polynomials. For NURBS they are piecewise rational polynomials. A rational B-Spline curve in $\mathbb{R}^d$ is the projection onto d-dimensional physical space of a non-rational (polynomial) B-spline curve defined in $d+1$-dimensional homogeneous coordinate space. In three-dimensional Euclidean space, the control points $R_{i,p}(\xi)=\dfrac{N_{i,p}(\xi)w_i}{\sum_{i=1}^{n}N_{i,p}(\xi)w_i}$.

Then homogeneous four-dimensional control points are written as Kiendl [26]:

$$\mathbf{P}^w=\{wx,wy,wz,w\}=\{X,Y,Z,W\},w\neq 0, \tag{3.10}$$

and the non-rational B-Spline curve is obtained as follows:

$$\mathbf{C}^w(\xi)=\sum_{i=1}^{n}N_{i,p}(\xi)\mathbf{P}_i^w \tag{3.11}$$

Projecting back into three-dimensional space by using a mapping, denoted by Kiendl [26].

$$\mathbf{P}=H\mathbf{P}^w=H\{X,Y,Z,W\}=\begin{cases}\{X/W,Y/W,Z/W\} & if\ W\neq 0\\ direction\{X,Y,Z\} & if\ W=0\end{cases} \tag{3.12}$$

the rational B-Spline curve is yielded as:

$$\mathbf{C}(\xi)=\{x(\xi),y(\xi),z(\xi)\}=\frac{\sum_{i=1}^{n}N_{i,p}(\xi)w_i\mathbf{P}_i}{\sum_{i=1}^{n}N_{i,p}(\xi)w_i} \tag{3.13}$$

Defining NURBS basis functions as:

$$R_{i,p}(\xi)=\frac{N_{i,p}(\xi)w_i}{\sum_{i=1}^{n}N_{i,p}(\xi)w_i} \tag{3.14}$$

one can write a NURBS curve in the common way as the sum of control points times the respective basis functions:

$$\mathbf{C}(\xi)=\sum_{i=1}^{n}R_{i,p}(\xi)\mathbf{P}_i \tag{3.15}$$

If all controling weights are equal, the rational formula in **Eq. 3.14** scale down to the normal B-Spline functions. It means that this B-Spline is a particular case of NURBS with equilibrium controling weights, and all properties of B-Splines listed in

Section 3.1.4.3 apply to NURBS as well. The significant superiority of the basis rational functions is that they allow an exact shape of conic sections, including circle and ellipse curves. **Figure 3.4** shows a NURBS curve through an ellipse form. Therefore, the NURBS are able to draw smooth shapes, linear forms, sharp edges, as well as supreme geometric objects like spheres, cylinders, or ovals, etc. These informations explain why NURBS application can establish a standard rule sin CAD modelling.

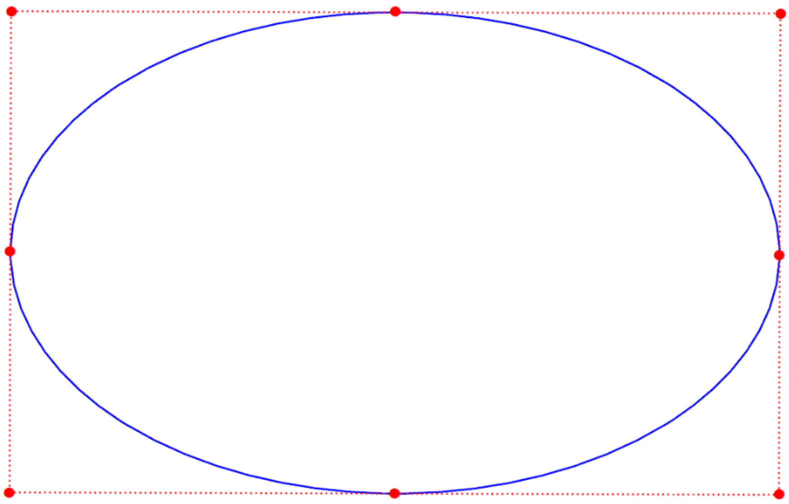

Figure 3.4 Exact ellipse represented by a NURBS curve

3.1.6 NURBS Refinement

There are two basic techniques for increasing the flexibility of a NURBS-based geoemtry, namely *knot insertion* and *degree elevation* or *order elevation.*

In knot insertion, the knot spans are divided into smaller ones by inserting new knots in order to enrich the basis functions. Knots may be inserted without changing a curve geometrically or parametrically. As a consequence, at this point the continuity is reduced by one. For each additional knot, an additional control point is inserted.

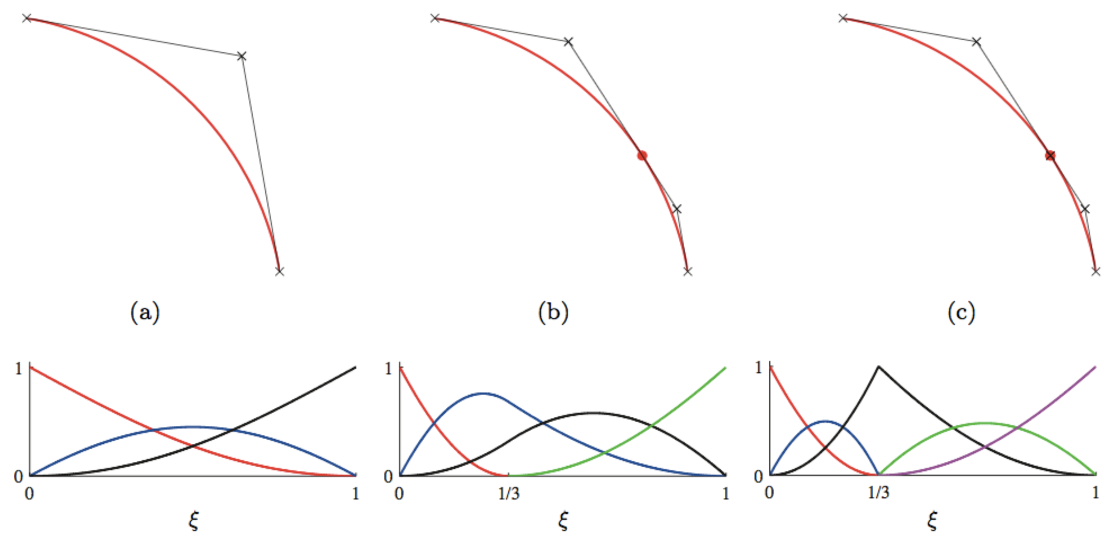

(d) $\Xi = \{0,0,0,1,1,1\}$ (e) $\bar{\Xi} = \{0,0,0,\frac{1}{3},1,1,1\}$ (f) $\bar{\bar{\Xi}} = \{0,0,0,\frac{1}{3},\frac{1}{3},1,1,1\}$

Figure 3.5 Successive insertion of the knot $\bar{\xi} = \dfrac{1}{3}$: (a) original geometry and (d) basic functions, (b)-(c) refined geometries and (e)-(f) corresponding basic funtions.

Related to elevation, the number of knot intervals remains same level but there is an increasing at polynomial degree of the basis functions. While the degree is grown, existing knots are repeated so that the continuity at these points sets at the same position. Focused on surfaces, refinementing procedures can be applied independently to both parametric directions ξ and η. With knot insertion, a very important feature of the elevation is that it does not change either the geometry or the numerals.

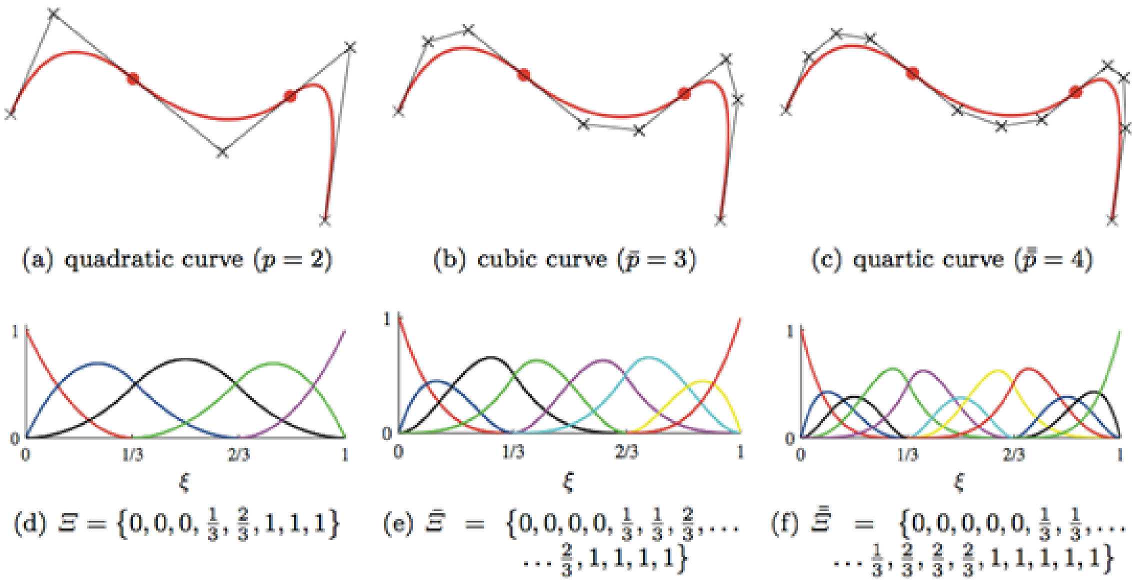

Figure 3.6 Successive degree elevation of the a quadratic rational curve: (a) original geometry and (d) basic functions, (b)-(c) degree elevated geometries and (e)-(f) basic function

There are standard algorithms about knot inserting and ordering elevation B-Splines, kindly refer Cottrell et al. [24]. With NURBS, the similar algorithms is able to utilize, however, it is necessary to put in an application the homogeneous control coordinates $\mathbf{P}_i^W$, which means B-Spline is refined in the projective $\mathbb{R}^4$ space. After obtaining the refinedly controling points in projective space, they are extrapolatedly back to the $\mathbb{R}^3$ space.

3.1.7 Continuity

For demonstrated isogeometric analysis, the continuity between elements and patches plays a crucial role in the following chapter. Therefore, this section shall mention about investigating conditions in continuity for B-Splines and NURBS.

About parametric curves and surfaces, there are two kinds of continuity which are the geometric and the parametric continuity. For the zeroth-order continuity, it equals as shown in the expression $G^0 = C^0$. However, for a continuity degree $k \geq 1$ they needs to be distinguished. Generally, the parametric continuity C^k implies the geometric continuity G^k but not vice versa. For the proposed method, the geometric continuity G^1 between surfaces is needed, so at first difference between G^1 and C^1 shall be briefly discussed.

Given are two curves $C^1\left(\xi\right)$ and $C^2\left(\xi\right), 0 \le \xi \le 1,$ which join at their ends:

$$C^1\left(1\right) = C^2\left(0\right) \tag{3.16}$$

the curves are C^1 continuous if their first derivatives at the joint are equal:

$$\frac{\partial C^1\left(1\right)}{\partial \xi} = \frac{\partial C^2\left(0\right)}{\partial \xi} \tag{3.17}$$

This means that their tangent vectors at the joint are parallel and have the same magnitude. For G^1 continuity, the tangent vectors only have to be parallel but not necessarily of the same magnitude Veldman [2]. So for G^1 the following equation must hold:

$$\frac{\partial C^1\left(1\right)}{\partial \xi} = c.\frac{\partial C^2\left(0\right)}{\partial \xi} \tag{3.18}$$

where *c* is a scalar multiplier.

For a B-Spline curve, the first derivatives at the endpoints of a B-Spline curve are given by **Eq. 3.8**. It is noted that the derivatives of NURBS are also conducted in a similar manner.

$$\frac{\partial C^1\left(1\right)}{\partial \xi} = \frac{p}{\xi_{p+2}}\left(P_2 - P_1\right) \tag{3.19}$$

$$\frac{\partial C^1\left(1\right)}{\partial \xi} = \frac{p}{1-\xi_n}\left(P_n - P_{n-1}\right) \tag{3.20}$$

The factors $\frac{p}{\xi_{p+2}}$ and $\frac{p}{1-\xi_n}$ *are* scalar multipliers of the tangent vectors and therefore irrelevant for the geometric continuity. The last control point of the first curve is equal to the first control point of the second curve, $C_n^1 = C_1^2,$ so the curves are G^1 continuous as illustrated in **Figure 3.9** if the following condition holds:

$$\left(C_2^2 - C_n^1\right) = c.\left(C_n^1 - C_{n-1}^1\right) \tag{3.21}$$

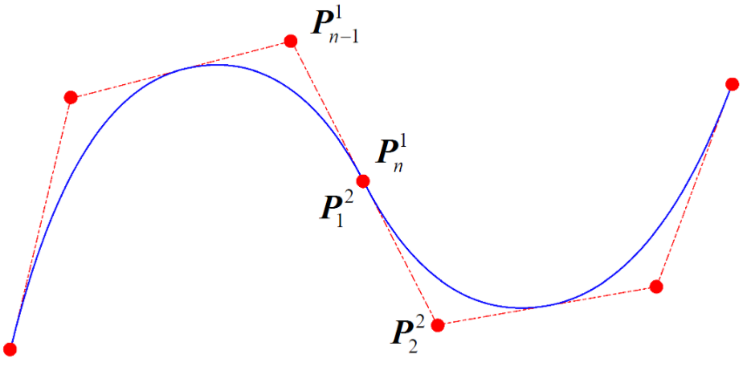

Figure 3.7 G^1 - continuous B-Spline curves

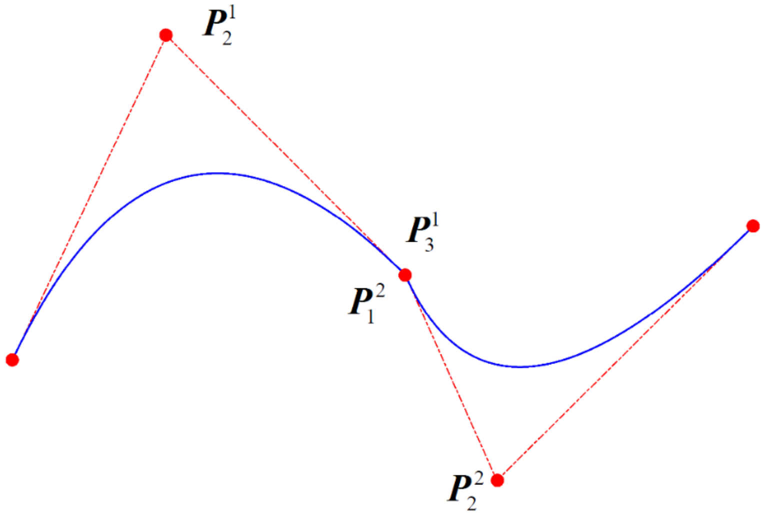

Figure 3.8 G^0 - continuous B-Spline curves

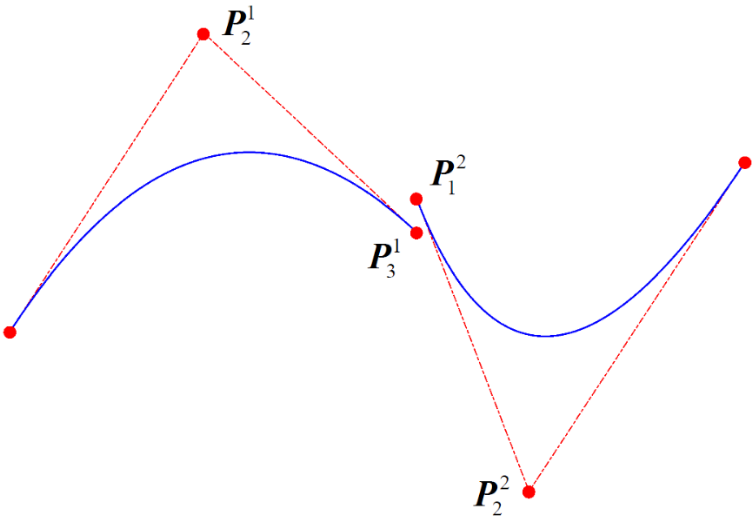

Figure 3.9 Discontinuous B-Spline curves

3.1.8 Isogeometric Analysis

The term *isogeometric analysis* was proposed by T.J.R. Hughes [37] and means that the analysis model uses the same mathematical description as the geometry model. It is an enhancement to isoparametric analysis. The isoparametric concept states that the same functions are used to describe the initial geometry and the unknown solution field, e.g displacements Zhang [38]. It is noted that in this context, initial geometry refers to the initial geometry of the analysis model. The isoparametric concept is an important prerequisite for the correct treatment of rigid body motions. In traditional finite elementinganalysis, low order, mostly linear, Lagrange polynomials are used as basis functions for the analysis, whereas computer aided geometry modeling is based on techniques like spline-functions and subdivision surfaces. As a consequence, a model conversion is necessary if a geometry designed in a CAD program is to be analyzed by FEA. For analysis, the geometry is converted into a mesh of finite elements, which is why this process is called meshing. This model conversion causes a series of problems. The most obvious problem is that due to the model conversion, geometric information is lost.

The finite element geometry is only an approximation to the original geometry and the quality of this approximation depends on the mesh density. However, an exact description of the geometry is crucial if small geometric imperfections can decide about the overall structural behavior, like in buckling of thin shells.

The second aspect is the time impact of meshing, which is a serious problem in industrial applications, especially since the whole process has to be redone every time a mesh needs to be refined or modified. The isogeometric analysis has shown many great advantages on solving many different problems in a wide range of research areas such as fluid-structure interaction Veldman [2], Kiendl [26], Nguyen-Thanh [27], shells T.J.R. Hughes [37], structural analysis J.A. Cottrell [24], Benson [28], Thai [29], fracture mechanics Cottrell [39] and so on.

The core idea of isogeometric analysis is that the functions used for the geometry description in CAD are adopted by the analysis for the geometry and the solution field. By this, the whole process of meshing can be omitted and the two models for design and analysis merge into one. The schematic illustration of NURBS paraphernalia is illustrated in **Figure 3.10**.

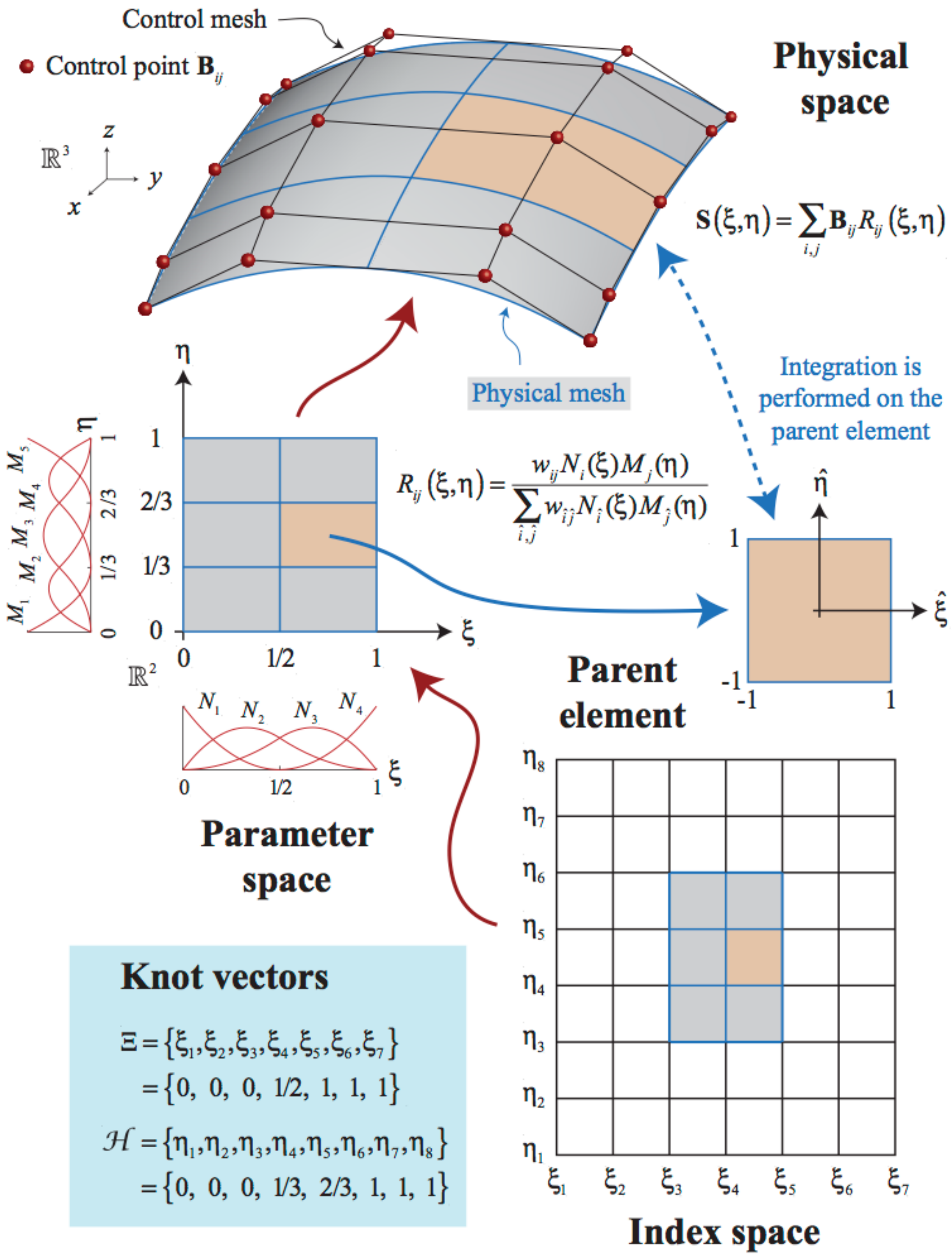

Figure 3.10 Schematic illustration of NURBS paraphernalia for a one-patch surface model. (Hughes et al [23])

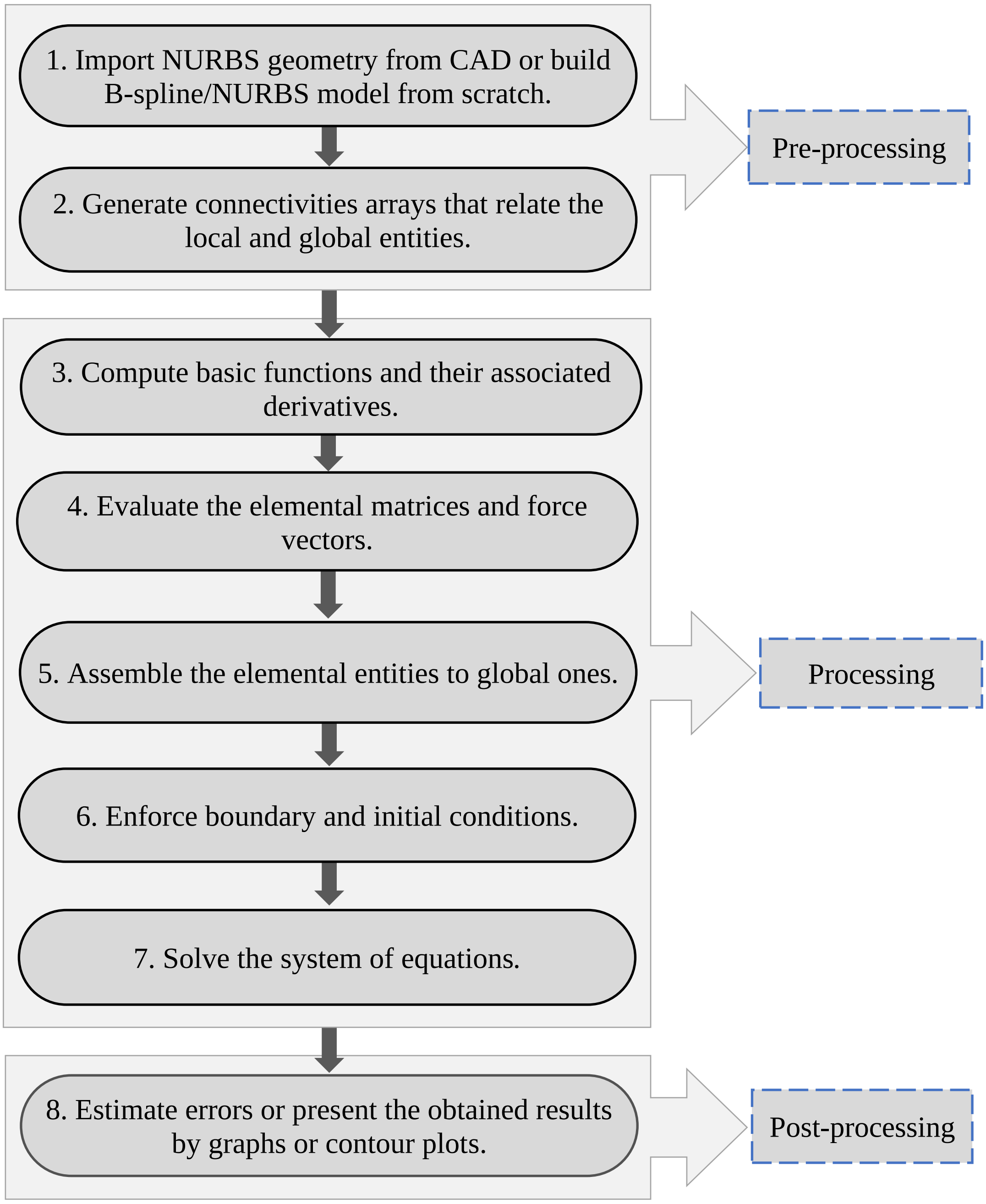

Figure 3.11 Summary of IGA procedure

3.1.9 NURBS-based elements for IGA

Similar to the traditional finite element analysis, the isogeometric analysis works with elements. For using NURBS-based isogeometric analysis, the NURBS elements are defined by non-zero knot spans of the knot vectors. This means that the domain consists of a couple of NURBS patches and each patch is a subdomain that is divided into elements by the knot vectors. In the following, more detailed information of isogeometric NURBS- elements are presented, as well as their consequences for analysis and the differences to classical finite elementinganalysis.

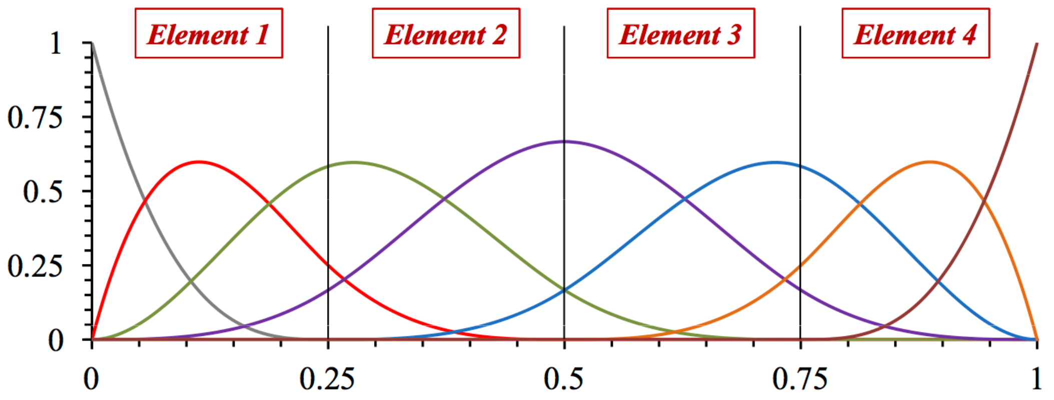

Figure 3.12 Isogeometric NURBS-elements in parametric space (Hughes et al [23])

A NURBS patch is defined over a parametric domain, which is divided into intervals by non-zero knot spans. These intervals are defined as elements. An example of NURBS elements is illustrated in **Figure 3.11**. The reason for this definition is that inside a knot interval, B-Spline basis functions are polynomials and therefore Gauss quadrature can be used for integration on element level. NURBS basis functions are not polynomials but rational polynomials. Therefore, the integration with Gauss quadrature is only approximative for NURBS basis functions. However, the use of Gauss quadrature for NURBS elements has been investigated and proven as reliable in the literature Chawla [1] and Wolfgang [25] as well as in the benchmark examples in this thesis (for the examples presented in this thesis, Gauss integration has been used). An efficient quadrature for NURBS-based isogeometric analysis that makes use of the higher continuities between elements, and therefore is more efficient than Gauss quadrature, is developed by Hughes [40].

Equivalent to finite elements, a NURBS element is defined by a set of nodes and corresponding basis functions. The nodes are the NURBS control points which carry the degrees of freedom for the analysis and boundary conditions are applied to them. Since the element formulation in this thesis is displacement-based, the degrees of freedom are the displacements of the control points. For two-dimensional structures this means that every control point has three degrees of freedom, namely the displacements in x- and y- direction. It is important to note that with this definition of elements, the basis functions are not confined to one element but extend over a series of elements, as illustrated in **Figure 3.11**. This is a very important difference to classical finite elements because it allows higher continuities of shape functions over the element boundaries.

As in the p-version of the finite elementingmethod Pilkey [41], the high-order nature of the basis functions generally results in higher accuracy compared to low-order elements. In contrast to p-version elements, NURBS-elements also have high-order continuities between elements, which is the basis for the element formulation presented in the next chapter. On the other hand, it means that the elements are interconnected and not independent of each other. The basis functions inside a knot span are defined by the Cox-deBoor recursion formula and depend on the neighboring knot spans, see **Eq. 3.4**. Therefore, it is not possible to define a single NURBS element without a complete NURBS patch. In this context, it is worth discussing the term elements since they are not independent, elementary parts that can be assembled arbitrarily to form a bigger model.

In the implementation persepctive, these elements can be treated exactly in the same way as classical finite elements. The stiffness matrix, for example, is evaluated on element level and assembled to the global stiffness matrix. The only difference is the use of different shape functions. The fact that the corresponding nodes, i.e. control points, usually lie outside the element, is solely a consequence of the used basis functions and does not make any difference in the treatment of these elements in a finite element code. Many locking phenomena in structural analysis are a consequence of the low-order basis functions that cannot correctly represent the physical behavior Bezier [42] and Hughes [23]. Since NURBS are higher order functions, these locking effects can be avoided efficiently.

The following important properties of NURBS as basis for analysis are summarized:

- The basis functions fulfill the requirements of linear independence and partition of unity. They have a local support, depending on the polynomial degree.
- Basis functions have higher-order continuities over element boundaries.

- Degrees of freedom are defined on the control points.
- The isoparametric concept is used.
- Rigid body motions are treated correctly (zero strains) due to the affine covariance property of NURBS.
- Locking effects stemming from low-order basis functions can be precluded efficiently.

3.1.10 Isogeometric Analysis versus Classical Finite elementingAnalysis

The use of NURBS basis for geometric modelling and analysis is the significant difference of isogeometric analysis versus standard finite elementingmethod. Isogeometric analysis employs NURBS basis functions to construct exact geometry at all levels of discretization, while the classical families of interpolatory polynomial as Lagrange polynomials or Hermite polynomials are widely utilized in typical finite elementinganalysis.

Major differences are listed in **Table 3.1**. On the other hand, isogeometric analysis and classical finite elementingshare many common features. For instance, they are both isoparametric implementations of Galerkins method, accordingly, isogeometric analysis inherites the computing implementation of finite elementingprocedure. Others are given in

Table 3.2.

Table 3.1 NURBS based isogeometric analysis versus classical finite element analysis. (Wolfgang [25])

Isogeometric analysis	**Classical finite elementing analysis**
- Exact geometry	- Approximate geometry
- Control points	- Nodal points
- Control variables	- Nodal variables
- Basis does not interpolate control points and variables	- Basis interpolates nodal points and variables
- NURBS basis	- Polynomial basis

- High, easily controlled continuity	- C^0-continuity, always fixed
- *hpk*-refinement space	- *hp*-refinement space
- Pointwise positive basis	- Basis not necessarily positive
- Convex hull property	- No convex hull property
- Variation diminishing in the presence of discontinuous data	- Oscillatory in the presence of discontinuous data

Table 3.2 Common features shared by isogeometric analysis and classical finite element analysis. (Wolfgang [25])

Isoparametric concept
Galerkins method
Code architecture
Compactly supported basis
Bandwidth of matrix
Partition of unity
Affine covariance
Patch tests are satisfied

3.2 Cotinuum-based governign equations of stability problems of inlfating beams

A large number of analytical analyses related to the inflating beams and arches are available in literature, concerning both theoretical and experimental analysis. One important aspect is need to build the best adapted analytical modeling for beam structures. Euler-Bernoulli kinematics and the Timoshenko kinematics are widely used to gain the analytical solutions and to develop the formulations for inflating beams made of woven fabrics. Comer [3] derived a load deflection theory in the case of isotropic beams. Main [43] and Main [5] proposed a method for analyzing the inflating fabric beams with a model analogous to the shear-moment method and developed the theory considering orthotropic membrane model. Fichter [7] Analytical buckling analysisconstructed Timoshenko cylindrical inflating beams made of elastic isotropic textile fabric based on energy minimization approach. Effects of air pressures to the load carrying capacity of the beam were taken into account.

In general, the beam theoretical model is developed based on the Assumptions are made as follows: (i) the cross section of the inflating beam remains undeformed under applied load, (ii) the cross section translation and rotations are small, (iii) the circumferential strain is negligible. Wielgosz [10] presented analytical solutions for inflating plates and tubes based on Timoshenko kinematics. The work took into account the geometric stiffness and the residual force effect due to the internal pressure. They indicated that the limit load is proportional to the applied pressure and that deflections are inversely proportional to the material properties of the fabrics and to the applied pressures. In order to improve Fichter's theory, Wielgosz [44] proposed a new formulation using the virtual work principle in Lagrangian form and Kirchhoff hypothesis with finite displacement and rotation to derive nonlinear equations of inflating beams. Davids [17] and Davids [18] presented nonlinear load-deflection response of Timoshenko inflating beams. Parametric studies have been also investigated in their work. Malm [19] used 3D isotropic fabric membrane finite element model to predict the beam load-deformation response.

In this chapter, theoretical formualtions developed by Nguyen and his coleagues ([22], [52] and [130]) are employed for the buckling problems of inflating composite beams is presented. The obtained governing equations are then discretized in accordance to IGA manner in the next chapter to find the numerical solutions of the buckling problems. It is noted that in the previous work of Nguyen ([22] and [52]), the author used traditional finite element approach to solve the problem.

3.2.1 Mathematical description of inflating beams

In this study, we focused our work on the Timoshenko beams made from orthotropic material. For inflating structures, the load is applied in two stages: First, the beam is inflating to the pressure p, and other external forces are applied. At the beginning of the first step, the internal pressure is zero and the beam is in its natural state **Figure 3.13a**. The reference configuration corresponds to the end of the first stage **Figure 3.13b**. The Green-Lagrange strain measure is used due to the geometrical nonlinearities.

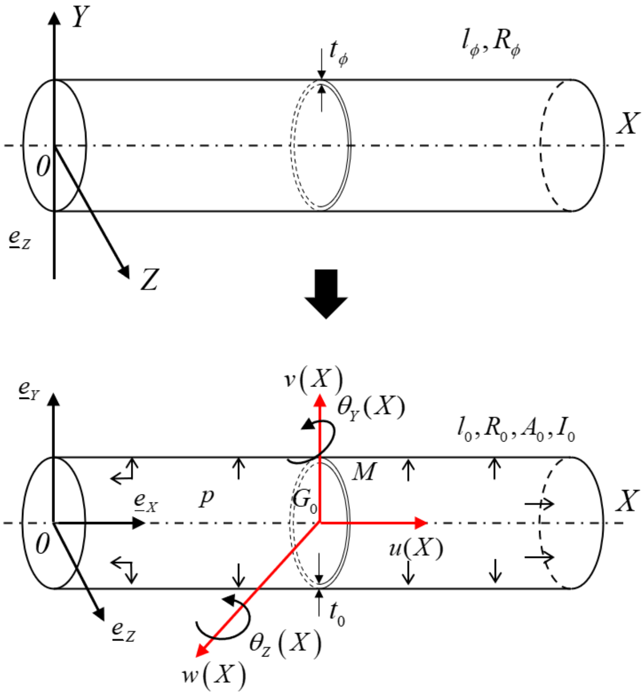

Figure 3.13 HOWF inflating beam: (a) in natural state and (b) in the reference configuration (inflating state)

Figure 3.13 shows an inflating cylindrical beam made of an HOWF. l_0, R_0, t_0, A_0 and I_0 represent respectively the length, the external radius, the fabric thickness, the cross-section and the second moment of inertia around the principal axes of inertia Y and Z of the beam in the reference configuration which is the inflating configuration. A_0 and I_0 are given by

$$A_0 = 2\pi R_0 t_0 \tag{3.22}$$

$$I_0 = \frac{A_0 R_0^2}{2} \tag{3.23}$$

where the reference dimensions l_0, R_0 and t_0 depend on the inflation pressure and the mechanical properties of the fabric Apedo [45]:

$$l_0 = l_\phi + \frac{pR_\phi l_\phi}{2E_t t_\phi}\left(1 - 2v_{lt}\right) \tag{3.24}$$

$$R_0 = R_\phi + \frac{pR_\phi^2}{2E_t t_\phi}\left(2 - \nu_{lt}\right) \quad 3.25$$

$$t_0 = t_\phi + \frac{3pR_\phi}{2E_t}\nu_{lt} \quad 3.26$$

in which l_ϕ, R_ϕ and t_ϕ are respectively the length, the fabric thickness, and the external radius of the beam in the natural state.

The internal pressure p is assumed to remain constant, which simplifies the analysis and is consistent with the experimental observations and the prior studies on inflating fabric beams and arches. The initial pressurization takes place prior to the application of concentrated and distributed external loads, and is not included in the structural analysis per se.

The slenderness ratio is $\lambda_s = \frac{L}{\rho}$ where $L = \mu l_0$ is the beam length and $\rho = \sqrt{\frac{I_0}{A_0}}$ is the beam radius of gyration. The coefficient μ takes different values according to the boundary conditions of the beam.

M is a point on the current cross-section and G_0 the centroid of the current cross-section lies on the X - *axis*. The beam is undergoing axial loading. Two Fichter's simplifying assumptions are applied in the following:

- The cross-section of the inflating beam under consideration is assumed to be circular and maintains its shape after deformation, so that there are no distortion and local buckling;
- The rotations around the principal inertia axes of the beam are small and the rotation around the beam axis is negligible.

3.2.2 Theoretical formulation

3.2.2.1 Kinematic relations

The material is assumed orthotropic and the warp direction of the fabric is assumed to coincide with the beam axis; thus the weft yarn is circumferential. The model can be adapted to the case where the axes are in other directions. In this case, an additional rotation may be operated to relate the orthotropic directions and the beam axes. This general case is not addressed here because, for an industrial purpose, the orthotropic principal directions coincide with the longitudinal and circumferential directions of the cylinder.

With the hypotheses proposed by Fichter were applied, the displacement filed of an arbitrary point *M(X, Y, Z)* are expressed as follows:

$$\underline{\mathbf{u}}(M)=\begin{Bmatrix}\underline{u}_X\\ \underline{u}_Y\\ \underline{u}_Z\end{Bmatrix}=\begin{Bmatrix}u(X)\\ v(X)\\ w(X)\end{Bmatrix}+\begin{Bmatrix}Z\theta_Y(X)\\ 0\\ 0\end{Bmatrix}+\begin{Bmatrix}-Y\theta_Z(X)\\ 0\\ 0\end{Bmatrix} \qquad 3.27$$

Where $\underline{u}_X,\underline{u}_Y$ and $\underline{u}_Z$ are the components of the displacement at the arbitrary point *M*, whilst $u(X),v(X)$ and $w(X)$ correspond to the displacements of the centroid G_0 of the current cross-section at abscissa X, related to the base (X, *Y, Z*); $\theta_Y(X)$ and $\theta_Z(X)$ are the rotations of the current section at abscissa X around both principal axes of inertia of the beam, respectively. Let $\delta\underline{\mathbf{u}}$ denote an arbitrary virtual displacement from the current position of the material point M:

$$\delta\underline{\mathbf{u}}=\begin{Bmatrix}\delta u(X)\\ \delta v(X)\\ \delta w(X)\end{Bmatrix}+\begin{Bmatrix}Z\delta\theta_Y(X)\\ 0\\ 0\end{Bmatrix}+\begin{Bmatrix}-Y\delta\theta_Z(X)\\ 0\\ 0\end{Bmatrix} \qquad 3.28$$

The definition of the strain at an arbitrary point as a function of the displacements is:

$$\underline{\underline{\mathbf{E}}}=\underline{\underline{\mathbf{E}}}_l+\underline{\underline{\mathbf{E}}}_{nl} \qquad 3.29$$

Where $\mathbf{E}_t$ and $\mathbf{E}_{nl}$ are respectively the Green-Lagrange linear and nonlinear strains. The nonlinear term $\mathbf{E}_{nl}$ takes into account the geometrical nonlinearities. The strain fields depend on the displacement fields as following:

$$\underline{\underline{\mathbf{E}}}_l = \begin{Bmatrix} \dfrac{\partial u_X}{\partial X} \\ \dfrac{\partial u_Y}{\partial Y} \\ \dfrac{\partial u_Z}{\partial Z} \\ \dfrac{\partial u_X}{\partial Y} + \dfrac{\partial u_Y}{\partial X} \\ \dfrac{\partial u_X}{\partial Z} + \dfrac{\partial u_Z}{\partial X} \\ \dfrac{\partial u_Y}{\partial Z} + \dfrac{\partial u_Z}{\partial Y} \end{Bmatrix}, \underline{\underline{\mathbf{E}}}_{nl} = \begin{Bmatrix} \dfrac{1}{2}\underline{\mathbf{u}}_{,X}^T \underline{\mathbf{u}}_{,X} \\ \dfrac{1}{2}\underline{\mathbf{u}}_{,Y}^T \underline{\mathbf{u}}_{,Y} \\ \dfrac{1}{2}\underline{\mathbf{u}}_{,Z}^T \underline{\mathbf{u}}_{,Z} \\ \dfrac{1}{2}\underline{\mathbf{u}}_{,X}^T \underline{\mathbf{u}}_{,Y} + \dfrac{1}{2}\underline{\mathbf{u}}_{,Y}^T \underline{\mathbf{u}}_{,X} \\ \dfrac{1}{2}\underline{\mathbf{u}}_{,X}^T \underline{\mathbf{u}}_{,Z} + \dfrac{1}{2}\underline{\mathbf{u}}_{,Z}^T \underline{\mathbf{u}}_{,X} \\ \dfrac{1}{2}\underline{\mathbf{u}}_{,Y}^T \underline{\mathbf{u}}_{,Z} + \dfrac{1}{2}\underline{\mathbf{u}}_{,Z}^T \underline{\mathbf{u}}_{,Y} \end{Bmatrix} \qquad 3.30$$

The higher-order nonlinear terms are the product of the vectors that are defined as follows

$$\underline{\mathbf{u}}_{,X} = \begin{Bmatrix} u_{X,X} \\ u_{Y,X} \\ u_{Z,X} \end{Bmatrix}, \underline{\mathbf{u}}_{,Y} = \begin{Bmatrix} u_{X,Y} \\ u_{Y,Y} \\ u_{Z,Y} \end{Bmatrix}, \underline{\mathbf{u}}_{,Z} = \begin{Bmatrix} u_{X,Z} \\ u_{Y,Z} \\ u_{Z,Z} \end{Bmatrix} \qquad 3.31$$

3.2.2.2 Constitutive equations

In this study, the Saint Venant-Kirchhoff orthotropic material is employed. The energy function $\Phi_E = \Phi\left(\underline{\underline{\mathbf{E}}}\right)$ related to this case is known as the Helmholtz free-energy function.

To describe the behavior of the inflating beam, we define two coordinate systems: A local warp and weft direction coordinate system related to each point of the membrane coincident with the principal directions of the fabric **Figure 3.14a**. And the other is the Cartesian coordinate system attached to the beam **Figure 3.14b**.

The components of the second Piola-Kirchhoff tensor $\underline{\underline{S}}$ are given by the nonlinear Hookean stress-strain relationships

$$\underline{\underline{\mathbf{S}}} = \underline{\underline{\mathbf{S}}}^o + \frac{\partial \Phi}{\partial \underline{\underline{\mathbf{E}}}} = \underline{\underline{\mathbf{S}}}^o + \underline{\underline{\underline{\underline{\mathbf{C}}}}}.\underline{\underline{\mathbf{E}}} \qquad 3.32$$

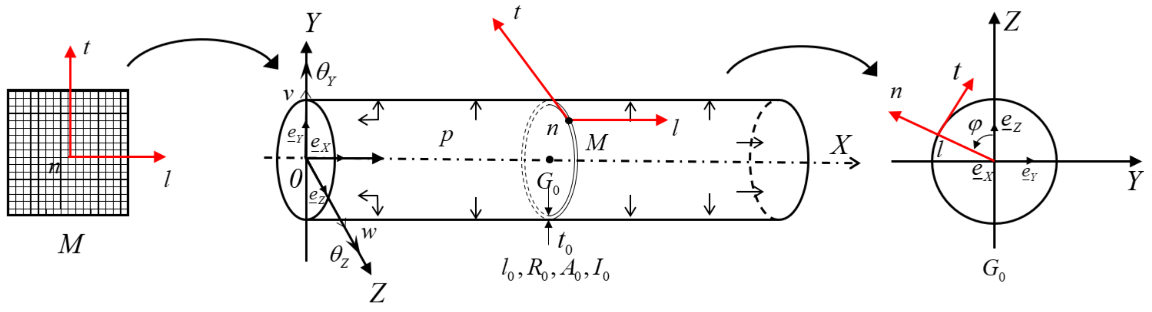

Figure 3.14 (a) Fabric local coordinate system, (b) Beam Cartesian coordinate system

where

- $\underline{\underline{\mathbf{S}}}^o$ is the inflation pressure prestressing tensor.

- the second Piola-Kirchhoff tensor is written in the beam coordinate system as

$$\underline{\underline{\mathbf{S}}} = \begin{bmatrix} S_{XX} & S_{XY} & S_{XZ} \\ & S_{YY} & S_{YZ} \\ symmetrical & & S_{ZZ} \end{bmatrix} \qquad 3.33$$

- $\underline{\underline{\underline{\underline{\mathbf{C}}}}}$ is the fourth-order elasticity tensor expressed in the beam axes.

In general, the inflation pressure prestressing tensor is assumed spheric and isotropic Wielgosz [44]. So,

$$\underline{\underline{\mathbf{S}}}^o = S^o \underline{\underline{\mathbf{I}}} \qquad 3.34$$

Where $\underline{\underline{\mathbf{I}}}$ is the identity second order tensor and $S^o = \dfrac{N_o}{A_o}$ is the prestressing scalar. The elasticity tensor expressed in the beam axes can be calculated from the local orthotropic elasticity tensor using the rotation matrix R (see Apedo [45]):

$$C_{ijkl} = R_{im} R_{jn} R_{kp} R_{lq} C^{loc}_{mnpq} \qquad 3.35$$

With i, j, k, m, n, p, q = 1, …, 3, where

$$\underline{\underline{\mathbf{R}}} = \begin{bmatrix} 1 & 0 & 0 \\ 0 & \cos\varphi & -\sin\varphi \\ 0 & \sin\varphi & \cos\varphi \end{bmatrix} \qquad 3.36$$

and

$$\underline{\underline{\underline{\mathbf{C}}}}^{loc} = \begin{bmatrix} C_{11} & C_{12} & 0 \\ C_{12} & C_{22} & 0 \\ 0 & 0 & C_{66} \end{bmatrix} \quad 3.37$$

The elasticity tensor in the beam axes then obtained as

$$\underline{\underline{\underline{\mathbf{C}}}} = \begin{bmatrix} C_{11} & c^2C_{12} & s^2C_{12} & csC_{12} & 0 & 0 \\ & c^4C_{22} & c^2s^2C_{22} & c^3sC_{22} & 0 & 0 \\ & & s^4C_{22} & cs^3C_{22} & 0 & 0 \\ & & & c^2s^2C_{22} & 0 & 0 \\ & & & & s^2C_{66} & csC_{66} \\ symmetrical & & & & & c^2C_{66} \end{bmatrix} \quad 3.38$$

Where $c = \cos\varphi$ and $s = \sin\varphi$ with $\varphi = (e_Z, n)$ being the angle between the Z-axis and the normal of the membrane. The components of the elasticity tensor are given by

$$C_{11} = \frac{E_t}{1 - \nu_{lt}\nu_{tl}}; C_{12} = \frac{E_l \nu_{tl}}{1 - \nu_{lt}\nu_{tl}};$$
$$C_{22} = \frac{E_t}{1 - \nu_{lt}\nu_{tl}}; C_{66} = G_{lt} \quad and \quad \frac{E_l}{\nu_{lt}} = \frac{E_t}{\nu_{tl}}$$

3.2.3 Virtual work principle

The balance equations of an inflating beam come from the virtual work principle (VWP). The VWP applied to the beam in its pressurized state is

$$\delta W_{\text{int}} = \delta W_{ext}^{d} + \delta W_{ext}^{p}, \forall \delta \underline{\mathbf{u}} \quad 3.39$$

$$\Leftrightarrow \int_{V_o} \underline{\underline{\mathbf{S}}} : \delta \underline{\underline{\mathbf{E}}} dV_o = \int_{V_o} \mathrm{f}.\delta \underline{\mathbf{u}} dV_o + \{R.\delta \underline{\mathbf{u}}\} + \int_{\partial V_o} \mathrm{t}\delta \underline{\mathbf{u}} dA, \forall \delta \underline{\mathbf{u}} \quad 3.40$$

where f and t are the body forces per unit volume and the traction forces per the left-hand-side of **Eq. 3.39** is formulated from the second Piola-Kirchhoff tensor $\underline{\underline{\mathbf{S}}}$ and the virtual Green strain $\delta \underline{\underline{\mathbf{E}}}$.

The virtual Green strain tensor is written in the beam coordinate system as

$$\delta \underline{\underline{\mathbf{E}}} = \delta \underline{\underline{\mathbf{E}}}_l + \delta \underline{\underline{\mathbf{E}}}_{nl} \quad 3.41$$

where

$$\delta \underline{\underline{\mathbf{E}}}_l = \left[\delta E^l_{XX} \quad \delta E^l_{YY} \quad \delta E^l_{ZZ} \quad \delta E^l_{YZ} \quad \delta E^l_{ZX} \quad \delta E^l_{XY} \right]^T \qquad 3.42$$

$$\delta \underline{\underline{\mathbf{E}}}_{nl} = \left[\delta E^{nl}_{XX} \quad \delta E^{nl}_{YY} \quad \delta E^{nl}_{ZZ} \quad \delta E^{nl}_{YZ} \quad \delta E^{nl}_{ZX} \quad \delta E^{nl}_{XY} \right]^T \qquad 3.43$$

with

$$\begin{aligned}
\delta E^l_{XX} &= \delta u_{,X} + Z\delta\theta_{Y,X} - Y\delta\theta_{Z,X} \\
\delta E^l_{YY} &= 0 \\
\delta E^l_{ZZ} &= 0 \\
\delta E^l_{YZ} &= 0 \\
\delta E^l_{XZ} &= \delta w_{,X} + \delta\theta_{Y,X} \\
\delta E^l_{XY} &= \delta v_{,X} - \delta\theta_Z
\end{aligned} \qquad 3.44$$

and

$$\begin{aligned}
\delta E^{nl}_{XX} &= \left(u_{,X} + Z\theta_{Y,X} - Y\theta_{Z,X} \right)\delta u_{,X} + v_{,X}\delta v_{,X} \\
&\quad + w_{,X}\delta w_{,X} + Z\left(u_{,X} + Z\theta_{Y,X} - Y\theta_{Z,X} \right)\delta\theta_{Y,X} \\
&\quad - Y\left(u_{,X} + Z\theta_{Y,X} - Y\theta_{Z,X} \right)\delta\theta_{Z,X} \\
\delta E^{nl}_{YY} &= \theta_Z \delta\theta_Z \\
\delta E^{nl}_{ZZ} &= \theta_Y \delta\theta_Y \\
\delta E^{nl}_{YZ} &= \left(\theta_Z\delta\theta_Y + \theta_Y\delta\theta_Z \right) \\
\delta E^{nl}_{XZ} &= \theta_Y\delta u_{,X} + \left(u_{,X} + Z\theta_{Y,X} - Y\theta_{Z,X} \right)\delta\theta_Y \\
&\quad + Z\theta_Y\delta\theta_{Y,X} - Y\theta_Y\delta\theta_{Z,X} \\
\delta E^{nl}_{XY} &= -\theta_Z\delta u_{,X} - Z\theta_Z\delta\theta_{Y,X} \\
&\quad - s\left(u_{,X} + Z\theta_{Y,X} - Y\theta_{Z,X} \right)\delta\theta_Z + Y\theta_Z\delta\theta_{Z,X}
\end{aligned} \qquad 3.45$$

The generalized resultant forces and moments, and the quantities $Q_i\left(i = 1,...,10\right)$ acting over the reference cross-section A_o can be related to the stresses in the beam by

$$\begin{Bmatrix} N \\ T_y \\ T_z \\ M_y \\ M_z \end{Bmatrix} = \int_{A_o} \begin{Bmatrix} S_{XX} \\ S_{XY} \\ S_{XZ} \\ ZS_{XX} \\ -YS_{XX} \end{Bmatrix} dA_o, \tag{3.46}$$

$$Q_i = \int_{A_o} \begin{Bmatrix} -YZS_{XX} \\ Z^2 S_{XX} \\ -ZS_{XY} \\ ZS_{XZ} \\ Y^2 S_{XX} \\ YS_{XY} \\ -YS_{XZ} \\ S_{YY} \\ S_{ZZ} \\ -S_{YZ} \end{Bmatrix} dA_o, \qquad i = 1,\ldots,10 \tag{3.47}$$

where, N corresponds to the axial force, T_y and T_z to the shear force in Y and Z directions respectively, M_y and M_z to the bending moments about the Y and Z-axis. Quantities Q_i depend on the initial geometry of the cross-section:

$$\begin{aligned} N = \int_{A_0} S_{XX}\, dA = N^0 + \Big\{ C_{11}\Big[u_{,X} + \frac{1}{2}\left(u_{,X}^2 + v_{,X}^2 + w_{,X}^2\right)\Big] \\ + \frac{1}{4} C_{12}\left(\theta_Y^2 + \theta_Z^2\right)\Big\} A_0 + \frac{1}{2} C_{11} I_0 \left(\theta_{Y,Z}^2 + \theta_{Z,X}^2\right) \end{aligned} \tag{3.48}$$

$$T_y = \int_{A_0} S_{XY}\, dA = \frac{1}{2} k_y A_0 C_{66} \left[v_{,X} - \theta_Z \left(1 + u_{,X}\right)\right] \tag{3.49}$$

$$T_z = \int_{A_0} S_{XZ}\, dA = \frac{1}{2} k_z A_0 C_{66} \left[w_{,X} - \theta_Y \left(1 + u_{,X}\right)\right] \tag{3.50}$$

$$M_y = \int_{A_0} ZS_{XX}\, dA = \left(1 + u_{,X}\right) C_{11} \theta_{Y,X} I_0 \tag{3.51}$$

$$M_z = -\int_{A_0} YS_{XX}\, dA = \left(1 + u_{,X}\right) C_{11} \theta_{Z,X} I_0 \tag{3.52}$$

and

$$Q_1 = -\int_{A_0} YZS_{XX}\,dA = \frac{1}{4} I_0 \left(C_{11} R_0^2 \theta_{Z,X} \theta_{Y,X} - C_{12} \theta_Z \theta_Y \right) \tag{3.53}$$

$$\begin{aligned} Q_2 = \int_{A_0} Z^2 S_{XX}\,dA = \Bigg\{ \frac{N^0}{A_0} + C_{11} \bigg[u_{,X} + \frac{1}{2}\left(u_{,X}^2 + v_{,X}^2 + w_{,X}^2 \right) \\ + \frac{1}{8} R_0^2 \left(3\theta_{Y,X}^2 + \theta_{Z,X}^2 \right) \bigg] + \frac{1}{8} C_{12} \left(3\theta_Z^2 + \theta_Y^2 \right) \Bigg\} I_0 \end{aligned} \tag{3.54}$$

$$Q_3 = -\int_{A_0} ZS_{XY}\,dA = \frac{1}{4} C_{66} I_0 \left(3\theta_Z \theta_{Y,X} - \theta_Y \theta_{Z,X} \right) \tag{3.55}$$

$$Q_4 = \int_{A_0} ZS_{XZ}\,dA = \frac{1}{4} C_{66} I_0 \left(\theta_Y \theta_{Y,X} - \theta_Z \theta_{Z,X} \right) \tag{3.56}$$

$$\begin{aligned} Q_5 = \int_{A_0} Y^2 S_{XX}\,dA = \Bigg\{ \frac{N^0}{A_0} + C_{11} \bigg[u_{,X} + \frac{1}{2}\left(u_{,X}^2 + v_{,X}^2 + w_{,X}^2 \right) \\ + \frac{1}{8} R_0^2 \left(\theta_{Y,X}^2 + 3\theta_{Z,X}^2 \right) \bigg] + \frac{1}{8} C_{12} \left(\theta_Z^2 + 3\theta_Y^2 \right) \Bigg\} I_0 \end{aligned} \tag{3.57}$$

$$Q_6 = \int_{A_0} YS_{XY}\,dA = \frac{1}{4} C_{66} I_0 \left(\theta_Z \theta_{Z,X} - \theta_Y \theta_{Y,X} \right) \tag{3.58}$$

$$Q_7 = -\int_{A_0} YS_{XZ}\,dA = \frac{1}{4} C_{66} I_0 \left(3\theta_{Z,X} \theta_Y - \theta_Z \theta_{Y,X} \right) \tag{3.59}$$

$$\begin{aligned} Q_8 = \int_{A_0} S_{YY}\,dA = N^0 + \frac{1}{2} A_0 \bigg\{ C_{12} \left[u_{,X} + \frac{1}{2}\left(u_{,X}^2 + v_{,X}^2 + w_{,X}^2 \right) \right] \\ + \frac{1}{8} C_{22} \left(3\theta_Z^2 + \theta_Y^2 \right) \bigg\} + \frac{1}{8} C_{12} I_0 \left(3\theta_{Y,X}^2 + \theta_{Z,X}^2 \right) \end{aligned} \tag{3.60}$$

$$\begin{aligned} Q_9 = \int_{A_0} S_{ZZ}\,dA = N^0 + \frac{1}{2} A_0 \bigg\{ C_{12} \left[u_{,X} + \frac{1}{2}\left(u_{,X}^2 + v_{,X}^2 + w_{,X}^2 \right) \right] \\ + \frac{1}{8} C_{22} \left(3\theta_Y^2 + \theta_Z^2 \right) \bigg\} + \frac{1}{8} C_{12} I_0 \left(3\theta_{Z,X}^2 + \theta_{Y,X}^2 \right) \end{aligned} \tag{3.61}$$

$$Q_{10} = -\int_{A_0} S_{YZ} dA = \frac{1}{8} C_{22} A_0 \theta_Y \theta_Z - \frac{1}{4} C_{12} I_0 \theta_{Y,X} \theta_{Z,X} \tag{3.62}$$

Then the internal virtual work may be written as:

$$-\delta W_{\text{int}} = \int_0^{l_o} \begin{Bmatrix} A_1(X) \\ B_1(X) \\ C_1(X) \\ D_1(X) \\ E_1(X) \\ F_1(X) \\ H_1(X) \end{Bmatrix}^T \times \begin{Bmatrix} \delta u_{,X} \\ \delta v_{,X} \\ \delta w_{,X} \\ \delta\theta_{,Y} \\ \delta\theta_{Y,X} \\ \delta\theta_Z \\ \delta\theta_{Z,X} \end{Bmatrix} dX \tag{3.63}$$

With the terms $A_1(X), B_1(X), C_1(X), D_1(X), E_1(X), F_1(X)$ and $H_1(X)$:

$$A_1(X) = \begin{Bmatrix} N \\ M_y \\ M_z \\ -T_y \\ T_z \end{Bmatrix}^T \times \begin{Bmatrix} 1+u_{,X} \\ \theta_{Y,X} \\ \theta_{Z,X} \\ \theta_Z \\ \theta_Y \end{Bmatrix} \tag{3.64}$$

$$B_1(X) = \begin{Bmatrix} N \\ T_y \end{Bmatrix}^T \times \begin{Bmatrix} v_{,X} \\ 1 \end{Bmatrix} \tag{3.65}$$

$$C_1(X) = \begin{Bmatrix} N \\ T_z \end{Bmatrix}^T \times \begin{Bmatrix} w_{,X} \\ 1 \end{Bmatrix} \tag{3.66}$$

$$D_1(X) = \begin{Bmatrix} T_z \\ Q_4 \\ Q_7 \\ Q_9 \\ Q_{10} \end{Bmatrix}^T \times \begin{Bmatrix} 1+u_{,X} \\ \theta_{Y,X} \\ \theta_{Z,X} \\ \theta_Y \\ \theta_Z \end{Bmatrix} \tag{3.67}$$

$$E_1(X)=\begin{Bmatrix} M_y \\ Q_1 \\ Q_2 \\ Q_3 \\ Q_4 \end{Bmatrix}^T \times \begin{Bmatrix} 1+u_{,X} \\ \theta_{Z,X} \\ \theta_{Y,X} \\ \theta_Z \\ \theta_Y \end{Bmatrix} \quad 3.68$$

$$F_1(X)=\begin{Bmatrix} -T_y \\ Q_3 \\ Q_6 \\ Q_8 \\ Q_{10} \end{Bmatrix}^T \times \begin{Bmatrix} 1+u_{,X} \\ \theta_{Y,X} \\ \theta_{Z,X} \\ \theta_Z \\ \theta_Y \end{Bmatrix} \quad 3.69$$

$$H_1(X)=\begin{Bmatrix} M_z \\ Q_5 \\ Q_1 \\ Q_6 \\ Q_7 \end{Bmatrix}^T \times \begin{Bmatrix} 1+u_{,X} \\ \theta_{Z,X} \\ \theta_{Y,X} \\ \theta_Z \\ \theta_Y \end{Bmatrix} \quad 3.70$$

The external virtual work δW_{ext} is due to the dead loads and to the pressure load.

The dead loads, which may include concentrated loads and moments as well as distributed loads, act like the body forces. The inflation pressure plays a role of a traction force acting on the cylindrical surface and on both ends. The first term on the right side of **Eq. 3.40** can be rewritten as

$$\begin{aligned}\delta W_{ext}^d &= \int_0^{l_o} \begin{Bmatrix} f_x \\ f_y \\ f_z \end{Bmatrix} \times \begin{Bmatrix} \delta u \\ \delta v \\ \delta w \end{Bmatrix} dX \\ &+ \sum_{i=1}^{n} \begin{Bmatrix} F_X(X_i) \\ F_Y(X_i) \\ F_Z(X_i) \\ M_Y(X_i) \\ M_Z(X_i) \end{Bmatrix} \times \begin{Bmatrix} \delta u(X_i) \\ \delta v(X_i) \\ \delta w(X_i) \\ \delta\theta_Y(X_i) \\ \delta\theta_Z(X_i) \end{Bmatrix}\end{aligned} \quad 3.71$$

In which f_x, f_y and f_z are respectively the distributed loads along the X, *Y*, and *Z* axes, while $F_a(b)$, and $M_a(b)$ (With $a = X, Y, Z; b = X_1, ..., X_n$) are the external support reactions and the external loads and moments.

The second term on the right side of **Eq. 3.40** is the external virtual work due to the inflation pressure. This virtual work includes the pressure virtual work on the cylindrical surface δW^p_{cyl} and on both ends δW^p_{end}, **Figure 3.15** shows a reference cylindrical inflating beam with an applied uniform pressure *p* acting on the cylindrical surface *A* which has a pointwise normal $\underline{\mathbf{n}}$ in the current configuration. The traction force vector **t** in **Eq. 3.40** is therefore $p\underline{\mathbf{n}}$ and the virtual work due to the inflation pressure δW^p_{ext} is then given by

$$\delta W^p_{ext} = \delta W^p_{cyl} + \delta W^p_{end} = \int_A p\underline{\mathbf{n}}.\delta\underline{\mathbf{u}} dA \qquad 3.72$$

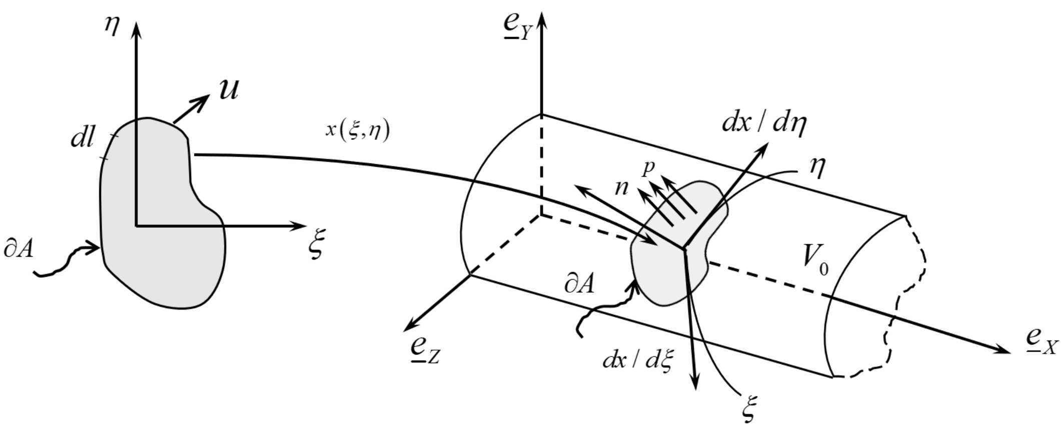

Figure 3.15 Uniform pressure on the cylindrical surface (Nguyen [52])

To determine the pressure virtual work δW^p_{cyl}, the curvilinear coordinates (ξ, η) are used **Figure 3.16**:

$$\begin{cases} \xi = R_o \alpha \\ \eta = X \end{cases} \qquad 3.73$$

where α is the polar angle between the normal $\underline{\mathbf{n}}$ at a current position $\underline{\mathbf{x}}$ and the $\underline{\mathbf{e}}_Y$. The coordinates of a material point M_o are given by

$$\underline{OM}_o = \underline{\mathbf{X}} = \begin{vmatrix} X \\ R_o \cos\alpha \\ R_o \sin\alpha \end{vmatrix} \qquad 3.74$$

The position vector at the current configuration is then given by

$$\underline{\mathbf{OM}} = \underline{\mathbf{x}} = \underline{\mathbf{X}} + \underline{\mathbf{U}} = \begin{vmatrix} X + u(X) - R_o\theta_Z \cos\alpha + R_o\theta_Y \sin\alpha \\ v(X) + R_o \cos\alpha \\ w(X) + R_o \sin\alpha \end{vmatrix} \qquad 3.75$$

By using an arbitrary parameterization of the surface as shown in **Figure 3.15**, the

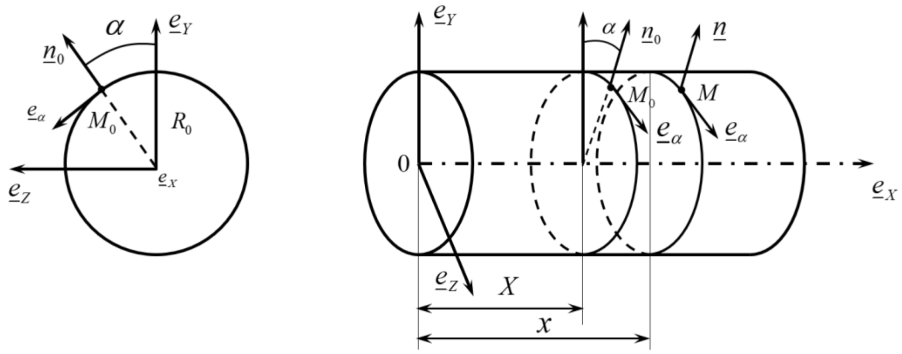

Figure 3.16 Definition of the curvilinear coordinate system

normal and area elements can be obtained in terms of the tangent vectors $\dfrac{\partial x}{\partial \xi}$ and $\dfrac{\partial x}{\partial \eta}$ as

$$\underline{\mathbf{n}} = \frac{\dfrac{\partial x}{\partial \xi} \times \dfrac{\partial x}{\partial \eta}}{\left\| \dfrac{\partial x}{\partial \xi} \times \dfrac{\partial x}{\partial \eta} \right\|} = \frac{\dfrac{\partial x}{R_o \partial \alpha} \times \dfrac{\partial x}{\partial X}}{\left\| \dfrac{\partial x}{R_o \partial \alpha} \times \dfrac{\partial x}{\partial X} \right\|}; \qquad 3.76$$

and

$$\begin{aligned} dA &= \left\| \frac{\partial x}{\partial \xi} \times \frac{\partial x}{\partial \eta} \right\| d\xi d\eta \\ &= \left\| \frac{\partial x}{R_o \partial \alpha} \times \frac{\partial x}{\partial X} \right\| R_o d\alpha dX \end{aligned} \qquad 3.77$$

Then δW_{cyl}^{p} is:

$$\delta W_{cyl}^{p} = \int_A p.\delta \underline{\mathbf{u}} \left(\frac{\partial x}{\partial \xi} \times \frac{\partial x}{\partial \eta} \right) d\xi d\eta \qquad 3.78$$

$$= F_p \int_0^{l_o} \begin{bmatrix} -\theta_{Z,X} & \theta_{Y,X} & -w_{,X} & v_{,X} \end{bmatrix} \times \begin{Bmatrix} \delta v \\ \delta w \\ \delta \theta_Y \\ \delta \theta_Z \end{Bmatrix} dX \qquad 3.79$$

The pressure virtual work at the ends of the beam can be determined in the same way: the reference circular end surfaces ($X = 0$ and $X = l_o$) can be represented by the curvilinear coordinates $(\xi, \eta) = (r, r\alpha)$ **Figure 3.17**. Then,

$$\delta W_{end}^{p} = \int_A p\underline{\mathbf{n}}.\delta \underline{\mathbf{u}}(l_o) dA - \int_A p\underline{\mathbf{n}}.\delta \underline{\mathbf{u}}(0) dA \qquad 3.80$$

$$= \left[\begin{bmatrix} 1 & \theta_Z(X_o) & -\theta_Y(X_o) \end{bmatrix} \times \begin{Bmatrix} \delta u(X_o) \\ \delta v(X_o) \\ \delta w(X_o) \end{Bmatrix} \right]_0^{l_o} \qquad 3.81$$

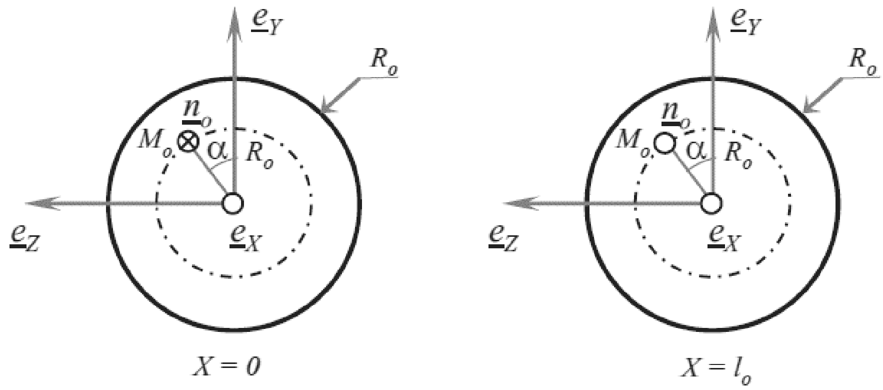

Figure 3.17 Definition of the curvilinear basis at the beam ends.

From **Eq. 3.78** and **Eq. 3.80** δW_{ext}^{p} is given by

$$\delta W_{ext}^{p} = F_p \int_0^{l_o} \begin{bmatrix} -\theta_{Z,X} & \theta_{Y,X} & -w_{,X} & v_{,X} \end{bmatrix} \times \begin{Bmatrix} \delta v \\ \delta w \\ \delta \theta_Y \\ \delta \theta_Z \end{Bmatrix} dX$$
$$+ \left[\begin{bmatrix} 1 & \theta_Z(X_o) & -\theta_Y(X_o) \end{bmatrix} \times \begin{Bmatrix} \delta u(X_o) \\ \delta v(X_o) \\ \delta w(X_o) \end{Bmatrix} \right]_0^{l_o} \qquad 3.82$$

where $F_p = p\Pi R_o^2$ is the pressure force due to the inflation pressure.

One can note that, according to **Eq. 3.82**, the follower force effect of the external load due to the inflation pressure depends on the displacements and the rotations.

3.3 Conclusion

In this chapter, the fundamental concepts of IGA and its general implementation as an alternaltive finite element approach are instroduced. In addition, an analytical approach is presented to develop the governing equations of the inflating beams based on HOWF 3D Timoshenko theory.

For the IGA, some prominent features of the approach are summarized as follows:

1) A concept explaining the ultimate goal of eliminating the conversion from CAD files to CAE codes is IGA. It is accomplished by employing the same basis functions of CAD for analysing.

2) B-spline basis functions from the so-called knot vector can readily be computed by the Cox-de Boor algorithm. Its associating derivatives can be expressed as linear combination of the lower order bases.

3) B-spline curve is defined by a linear combination of basis functions and corresponding control points. B-spline surface and volume are defined analogously by taking advantage of tensor product structure of B-splines.

4) B-splines offers three kinds of mesh refinement which are named h-refinement, p-refinement and k-refinement. While the first two techniques are fairly

equivalent to element subdivision and order rising in FEA, respectively, the third one is exclusive to B-splines which results in higher interelement continuity.

5) NURBS in d is defined by conic projecting B-splines in d+1, where the coordinates of the (d+1)th dimension are the strictly positive weights. This transformation has the ability to represent exact conic sections.

6) NURBS geometry therefore is defined similarly as B-spline one.

7) Numerical integration in NURBS-based IGA is performed via two successive mappings, the first one is from natural/parent space to parametric space and the second one is from parametric space to physical space.

8) Since the same B-spline/NURBS curve can be represented by concatenated.

9) Bézier curves, one can decompose the B-spline/NURBS curve into several C^0 Bézier elements for using in the analysis. This procedure makes the IGA approach backward compatible with conventional FEM codes.

In the theoretical development of stability governing equations, the total Lagrangian form of the virtual work principle and Timoshenko kinematics were employed. These equations are then discretized to develop the global buckling equations in the next chapter. By taking into account the orthotropic character in the present model, the study pointed out that only the mechanical properties E_l and G_{lt} intervene explicitly in the solution of critical load through C_{11} and C_{66} while E_t intervenes implicitly through the reference dimensions of the beam. Only the level of orthotropy of the fabric causes noticeable discrepancies in the buckling behavior of the inflating beam. This comes from the inequality of the mechanical properties in the yarn directions. The differences between the models studied also come from the way of the establishment of the constitutive equations. In previous studies, the material is assumed to be hyper-elastic isotropic and obeying the Saint Venant-Kirchhoff law in which only S_{XX} and S_{YY} are considered. The Young modulus E is also used directly in the Hookean stress-strain relationship. In the present model, we consider all components of the second Piola-Kirchhoff tensor. The elasticity tensor with the tensor components described the mechanical properties of the orthotropic material is used instead of the Young modulus E.

CHAPTER 4: IGA-BASED BUCKLING ANALYSIS OF INFLATING COMPOSITE BEAMS

4.1 Introduction

The finite element analyses of inflating fabric structures are challenging on both material and geometric nonlinearitie, which arise due to the nonlinear load, deflection behavior of the fabric, stiffening pressure of the inflating fabric, fabric-tofabric contact, and fabric wrinkling on the structural surface.

In the literature, only the inflating tensile structures are currently addressed and the inflating lightweight structure are responsed to examine by service loads. Previous studies assumed that the beams's materials are homogeneous isotropic and employed the membrane or thin shell theory determine the structural response. In earlier work, Libai [46] found the governing equations about incremental stress state in a membrane tube shaped orthotropic circular. In studying details, the membrane was taken to be hyperelastic and was not specified. Changing in load that includes uniform internal pressure and longitudinal extension are regarded as a small perturbation on initial homogeneous stress state. The approach about a known homogeneous reference state was based on the linearization of the equations. Functions of rectangular elements with Hermite cubic shape were used in conjunction with the variational principles. Wielgosz [10] and Wielgosz [14]; Thomas [11] implemented an inflating beam finite elementingand it was used to compute deflection of hyperstatic beams. The membrane of element was used as well. Then, Bouzidi [15] expressed two finite elements for 2D problems of inflating membranes: axisymmetric and cylindrical bending. The elements are built by large deflections hypothesis, finite strains and related pressure load. By solving directly opti-mization problem formulated and by the theorem of the minimum of the total potential energy, the numerical solution is obtained. By employing membrane elements and experimental results, Cavallaro [13] showed that pressurising structural tube differs from conventional metal fundamentally and fiber/matrix composite structures. The study commands a note that the plain-woven fabric appears to be an orthotropic material, the fabric does not behave as a continuum. However, effective material properties depend on the internal pressure of the beam as a discrete assemblage of individual tows. Weave geometry and the contact area of interacting tows. Suhey [6] presented the finite elementing model of an inflating open-oceanaquaculture cage using membrane elements with assuming the material is anisotropic.

Various authors used nonlinear elements to model the tension-only behavior of the fabric material in order to calculate the magnitudes of the deflection and the stress at the onset of wrinkling. The results were verified by the modified conventional beam theory Main [43] and Main [5]. Le van [12] and Le van [16] obtained the numerical results with a beam element developed from the earlier work of Fichter [7] and the 3D isotropic fabric membrane finite element. In their approach, the governing equations were discretized by the use of the virtual work principle with Timoshenko's kinematics, finite rotations and small strains. The linear eigen buckling analysis were carried out through a mesh convergence test using the 3D membrane finite elementingcomputations. Fichter [7] investigated linear and nonlinear finite elementingsolutions in bending by discretizing nonlinear equilibrium equations obtained from his previous analytical model in which a homogeneous orthotropic fabric was considered.

In inflating structures, with the arising of the local buckling that leads to the formation of the wrinkles, nonlinear problems pose the difficulty of solving the resulting nonlinear equations that result. Problems in these categories are geometric nonlinearity, in which deformation is large enough that equilibrium equations must be written with respect to the deformed structural geometry. Few works have dealt with buckling analysis of inflating structures. By means of the total Lagrangian formulation developed by Le van [12] and Le van [16], Diaby [47] proposed a numerical computation of buckles and wrinkles appearing in membrane structures. The bifurcation analysis is carried out without assuming any imperfections in the structure. In consideration of an inflating beam, Davids [18] progressed a quadratic Timoshenko beam element based on an incremental virtual work principle that accounts for fabric wrinkling via a moment-curvature nonlinearity. However, the materials were assumed to be isotropic in these studies.

In general, it is seen that the Finite element analyses of inflating fabric structures show a challenging in both material and geometric nonlinearities. The nonlinearities arise due to the nonlinear load/deflection behavior of the fabric (at low loads), pressure stiffening of the inflating fabric, fabric-to-fabric contact, and fabric wrinkling on the structural surface. In addition to check loads of fabric element, the finite elementing model is applied to anticipate the fundamental mode of the inflating fabric beam. Apedo [45] performed a theoretical analysis of inflating beams in which a homogeneous orthotropic fabric was considered. A 3D Timoshenko beam model has been developed and the nonlinear equations for the bending problem has been investigated by Apedo [48].

It can be seen that there are only a few works regarding to stability of inflating structures, and there is no work using the advanced numerical method, such as IGA, to investigate the buckling behavior of inflating composite beams. Therefore, this study has devoted linear and nonlinear buckling analysis of inflating beams where isogeometric analysis used to make orthotropic technical textiles. The method of analysis is based on a 3D Timoshenko beam model with a homogeneous orthotropic woven fabric (HOWF). The IGA-based numerical model use the quadratic NURBS-based Timoshenko elements with C^1-type continuity. The effects of geometric nonlinearities and the inflation pressure on the stable behavior of inflating beam with differently assessed boundary conditions. The influence of the beam aspect ratios on the buckling load coefficient are also pointed out. The obtained results are also compared with ones available in literature as well as experimental results.

4.2 IGA-based formulations for the buckling problems of inflating composite beams

4.2.1 Linear eigen buckling

In linear buckling analysis situation, the beam is subjected to the inflatedly prestressing pressure $\underline{\underline{\mathbf{S}}}^{\mathbf{0}}$ tensor. The very first step is to load the inflating beam by arbitrary reference level of external load, $\{\mathbf{F_{ref}}\}$ and to perform a standard linear analysis to determine the finite elementing stresses on the beam. It is also desired to have a general formula for finite elementingstress stiffness matrix $[\mathbf{k}_\sigma]$ and finite elementing elastic stiffness matrix $[\mathbf{k}]$. The strain energy of beam per volume unit is $\frac{1}{2}\underline{\underline{\mathbf{S}}}^{\mathrm{T}}\underline{\underline{\mathbf{E}}}$. As discuss in the previous chapter, the governing equations are derived based on the principle of virtual work. By integrating through the volume of the beam with respect to cross-sectional area A_o and the length l_o, an expression for the virtual strain energy of a finite inflating beam is:

$$\delta \mathrm{U_e} = \int_{\mathrm{V_o}} \left\{ \left(\underline{\underline{\mathbf{S}}}^0 \right)^{\mathrm{T}} \delta \underline{\underline{\mathbf{E}}} + \underline{\underline{\mathbf{E}}}^{\mathrm{T}} . \underline{\underline{\underline{\mathbf{C}}}} . \delta \underline{\underline{\mathbf{E}}} \right\} \mathrm{dV_0} = \delta \mathrm{U_m} + \delta \mathrm{U_b} \qquad 4.1$$

where U_m and U_b is membrane changing energy and the strain bending energy, sequently. To develop the element stiffness matrix for the beam, a displacement field $[u] = \{u, v, w, \theta_Y, \theta_z\}$ needs to be interpolated within each element. For the use of element for inflating beam, it is noted that the two-noded element often used for Euler-Bernoulli kinematics with Hermite polynomial as shape functions Bhatti [49], or a higher order element such as the three-node quadratic beam with reduced integration Le van [16] or the three-node Timoshenko beam that has quadratic shape functions for transverse displacement and linear shape functions for bending rotation and axial displacement Davids [17]; Davids [18]. In this quadratic NURBS basis functions are used as interpolation functions.

There are five degrees of freedom (DOF) associtated with an control point. The displacement vector is defined as $\{\mathbf{d}\}$ defines DOF vector $\{\mathbf{d}\} = \{u_j \quad v_j \quad w_j \quad \theta_{Yj} \quad \theta_{Zj}\}^T$. Then

$$\begin{Bmatrix} u \\ v \\ w \\ \theta_Y \\ \theta_Z \end{Bmatrix} = \begin{Bmatrix} \sum_{j=1}^{ncp} N_j u_j \\ \sum_{j=1}^{ncp} N_j v_j \\ \sum_{j=1}^{ncp} N_j w_j \\ \sum_{j=1}^{ncp} N_j \theta_{Yj} \\ \sum_{j=1}^{ncp} N_j \theta_{Zj} \end{Bmatrix} = [\mathbf{N}]\{\mathbf{d}\} \qquad 4.2$$

where index *j* defines the control point *j*, [**N**] the matrix of NURBS functions, which are discussed in the previous chapter, and *ncp* is the total number of control points.

The strain energy component δU_m of the beam is associated with the stress stiffness matrix $[\mathbf{k}_\sigma]$ and δU_b relates to the conventional elastic stiffness $[\mathbf{k}]$ of the beam, as

$$\begin{aligned} \delta \mathrm{U_e} &= \int_{\mathrm{V_o}} \left\{ \left(\underline{\underline{\mathbf{S}}}^0 \right)^{\mathrm{T}} \delta \underline{\underline{\mathbf{E}}} + \underline{\underline{\mathbf{E}}}^{\mathrm{T}} . \underline{\underline{\underline{\mathbf{C}}}} . \delta \underline{\underline{\mathbf{E}}} \right\} \mathrm{dV_0} \\ &= \int_{\mathrm{V_o}} \left[\{\delta \mathbf{d}\}^{\mathrm{T}} S^0 \left[\underline{\underline{\mathbf{I}}}^{\mathrm{T}} \right] \left[\underline{\underline{\mathbf{B}}}_\sigma \right] \{\delta \mathbf{d}\} + \{\delta \mathbf{d}\}^{\mathrm{T}} \left[\underline{\underline{\mathbf{B}}} \right]^T \left[\underline{\underline{\underline{\mathbf{C}}}} \right] \left[\underline{\underline{\mathbf{B}}} \right] \{\delta \mathbf{d}\} \right] \mathrm{dV_0} \\ &= \delta \mathrm{U_m} + \delta \mathrm{U_b} \end{aligned}$$

$$\delta U_m = \left[\delta \mathbf{d}^T \right] [\mathbf{k}_\sigma] [\mathbf{d}] \qquad 4.3$$

$$\delta U_b = \left[\delta \mathbf{d}^T \right] [\mathbf{k}] [\mathbf{d}] \qquad 4.4$$

By applying the discretization procedure, the gclobal equation is obtained as follows

$$\delta U_e = \{\delta \mathbf{d}\}^T \left([\mathbf{k}] + \lambda \left[\mathbf{k}_{ref} \right] \right) \{\mathbf{d}\} \qquad 4.5$$

where λ is the proportionality coefficient such as $F = \lambda F_{ref}$, with *F* is the axial load. The two matrix coefficients $[\mathbf{k}]$ and $\left[\mathbf{k}_{ref} \right]$ are constant and dependent on the geometry, material properties and the inflatedly prestressing pressure conditions acting on the beam. The stiffness matrix are evaluated using the Gauss numerical integration scheme. The element stiffness matrix assembly for entire structure leads to the equilibrium matrix equation in global coordinates. The potential energy of the whole beam is simply summarizing the potential energies of the individual finite elements. A whole structural matrix is generated by following the standard FEM assembly procedure.

The structural equilibrium equations can be obtained by applying the principle of minimum potential energy. This is expressed in in the form of eigenvalue problem:

$$\left([\mathbf{K}]+\lambda_i\left[\mathbf{K}_{ref}\right]\right)\{\delta\mathbf{D}\}=0 \qquad 4.6$$

Eq. 4.6 is an eigenvalue problem where λ_i is the eigenvalue of first buckling mode. The smallest root λ_{cr} defines the smallest level of external load for which there is decomposing named:

$$\{\mathbf{F}\}_{cr}=\lambda_{cr}\{\mathbf{F}\}_{ref} \qquad 4.7$$

As the beam is loaded by an arbitrary reference level of external load $\{\mathbf{F}\}_{ref}$, the eigenvector $\{\delta\mathbf{D}\}$ associated with λ_{cr} is the buckling mode. The magnitude of $\{\delta\mathbf{D}\}$ is indeterminate in a linear buckling problem, so that it defines a specified shape but not an amplitude.

4.2.2 Nonlinear buckling

Let us consider geometrically nonlinear behavior of HOWF inflating beam made of presumed linear elastic material. A nonlinear finite elementing intrinflating beam (NLFEIB) model is established. The total Lagrangian approach is adopted in which displacements refer to the initial configuration, for the description of geometric nonlinearity. Accordingly, we can display a tangent stiffness matrix $[\mathbf{K}_{\mathrm{T}}]$, which includes the effect of changing geometry as well as the effect of inflated pressure. The axial load at i^{th} is signified in following formula:

$$\{\mathbf{f}_i\}=\{\mathbf{f}_{i-1}\}+i\{\Delta\mathbf{f}\} \qquad 4.8$$

With a known element, the nonlinear equilibrium equation is able to be formulated as

$$[\mathbf{k}_T]\{\Delta\mathbf{d}\}=\{\mathbf{f}_i\} \qquad 4.9$$

where $\left[\mathbf{k}_T\right]$ is symbol of element tangent stiffness matrix, $\left\{\mathbf{f}_i\right\}$ and $\left\{\Delta\mathbf{d}\right\}$ are typically the external load increments vector of an element and an unknown displacement increment needs to be solved. After all the elements are assembling in the model, the below equi- librium equation is shown:

$$\left[\mathbf{K}_T\right]\left\{\Delta\mathbf{D}\right\} = \left\{\mathbf{F}_i\right\} \tag{4.10}$$

Eq. 4.10 can be interpreted by an incremental scheme that based on the straightfoward Newton using nodal load increments $\left\{\Delta\mathbf{F}\right\}$, with load correction terms and updates of $\left[\mathbf{K}_T\right]$ after each incremental step. Here, the model displacement vector $\left\{\mathbf{D}\right\}_i = \left\{\mathbf{D}\right\}_{i-1} + \left\{\Delta\mathbf{D}\right\}$, where $\left\{\Delta\mathbf{D}\right\}$ is the unknown node displacement increment at increment step *i* and $\left\{\mathbf{D}\right\}_{i-1}$ is node-beam displacement vector from the previous solution step. The equilibrium solution tolerance was taken as

$$\left\|\left\{\Delta\mathbf{D}\right\}_i\right\| = \left(\left\{\Delta\mathbf{D}\right\}_i^T \left\{\Delta\mathbf{D}\right\}_i\right)^{\frac{1}{2}} \le 0.0001 \tag{4.11}$$

or

$$\left\|\left\{\mathbf{R}\right\}_i\right\| = \left(\left\{\mathbf{R}\right\}_i^T \left\{\mathbf{R}\right\}_i\right)^{\frac{1}{2}} \le 0.0001 \tag{4.12}$$

with $\left\{\mathbf{R}\right\}_i = \left\{\mathbf{R}\left(\mathbf{D}_{i-1}\right)\right\} = \left[\mathbf{K}_T\right]\left\{\Delta\mathbf{D}_i\right\}$ being the globally unbalanced residual force vector from the previous increment. As a limit point is approached, displacement increments $\left\{\Delta\mathbf{D}\right\}$ become very large. Either at a limited point or bifurcationpoint, $\left[\mathbf{K}_T\right]$ becomes singular.

The outline of the algorithm at element level developed by Nguyen et al. [130] is empoyed in this study, (numerical integration procedure for calculating the element stiffness matrix at the jth element). The algorithm is describe as follows:

Require: Nodal unknown displacements $\left\{\Delta\mathbf{D}_i\right\}$, element number *j*th, model description.

Ensure: Element stiffness matrix $\left[\mathbf{K}_T^e\right]$, element load vectors $\left\{\mathbf{F}_{\text{int}}^e\right\}$ and $\left\{\mathbf{F}_{ext}^e\right\}$.

Loop on 1D Gauss integration *m* point(s) in the ξ direction:

for m = 1 to 3 do

Set sampling point location $\xi = \xi_m$ and associated weight factor W_m,

Call shape function subroutine to calculate element matrix $\left[\mathbf{B}\right]$ and Jacobian operator *J*, all at point ξ_m.

Calculate product $\left[[\mathbf{B}]^T\left(\left[\Psi_{\text{int}}\right]-\left[\Psi_{\text{ext}}\right]\right)[\mathbf{B}]\cdot W_m\right]$ and add it to array $\left[\mathbf{K}_T^e\right]$

Calculate element internal load factor and $\left\{T_{int}^e\right\}\cdot W_k$ add it to $\left\{\mathbf{F}_{\text{int}}^e\right\}$

Calculate element external load factor $\left(\left\{T_{ext}^d\right\}+\left\{T_{ext}^p\right\}\right).W_k$ and add it to array $\left\{\mathbf{F}_{ext}^e\right\}$.

end for

The matrices concerning internal and external forces for calculating the tangent stiffness, respectively, are

$$[\Psi_{int}] = \begin{bmatrix}
\frac{\partial A_1}{\partial u_{,\xi}} & \frac{\partial A_1}{\partial v_{,\xi}} & \frac{\partial A_1}{\partial w_{,\xi}} & \frac{\partial A_1}{\partial \theta_Y} & \frac{\partial A_1}{\partial \theta_{Y,\xi}} & \frac{\partial A_1}{\partial \theta_Z} & \frac{\partial A_1}{\partial \theta_{Z,\xi}} \\
\frac{\partial B_1}{\partial u_{,\xi}} & \frac{\partial B_1}{\partial v_{,\xi}} & \frac{\partial B_1}{\partial w_{,\xi}} & \frac{\partial B_1}{\partial \theta_Y} & \frac{\partial B_1}{\partial \theta_{Y,\xi}} & \frac{\partial B_1}{\partial \theta_Z} & \frac{\partial B_1}{\partial \theta_{Z,\xi}} \\
\frac{\partial C_1}{\partial u_{,\xi}} & \frac{\partial C_1}{\partial v_{,\xi}} & \frac{\partial C_1}{\partial w_{,\xi}} & \frac{\partial C_1}{\partial \theta_Y} & \frac{\partial C_1}{\partial \theta_{Y,\xi}} & \frac{\partial C_1}{\partial \theta_Z} & \frac{\partial C_1}{\partial \theta_{Z,\xi}} \\
\frac{\partial D_1}{\partial u_{,\xi}} & \frac{\partial D_1}{\partial v_{,\xi}} & \frac{\partial D_1}{\partial w_{,\xi}} & \frac{\partial D_1}{\partial \theta_Y} & \frac{\partial D_1}{\partial \theta_{Y,\xi}} & \frac{\partial D_1}{\partial \theta_Z} & \frac{\partial D_1}{\partial \theta_{Z,\xi}} \\
\frac{\partial E_1}{\partial u_{,\xi}} & \frac{\partial E_1}{\partial v_{,\xi}} & \frac{\partial E_1}{\partial w_{,\xi}} & \frac{\partial E_1}{\partial \theta_Y} & \frac{\partial E_1}{\partial \theta_{Y,\xi}} & \frac{\partial E_1}{\partial \theta_Z} & \frac{\partial E_1}{\partial \theta_{Z,\xi}} \\
\frac{\partial F_1}{\partial u_{,\xi}} & \frac{\partial F_1}{\partial v_{,\xi}} & \frac{\partial F_1}{\partial w_{,\xi}} & \frac{\partial F_1}{\partial \theta_Y} & \frac{\partial F_1}{\partial \theta_{Y,\xi}} & \frac{\partial F_1}{\partial \theta_Z} & \frac{\partial F_1}{\partial \theta_{Z,\xi}} \\
\frac{\partial H_1}{\partial u_{,\xi}} & \frac{\partial H_1}{\partial v_{,\xi}} & \frac{\partial H_1}{\partial w_{,\xi}} & \frac{\partial H_1}{\partial \theta_Y} & \frac{\partial H_1}{\partial \theta_{Y,\xi}} & \frac{\partial H_1}{\partial \theta_Z} & \frac{\partial H_1}{\partial \theta_{Z,\xi}}
\end{bmatrix}$$

and

$$[\Psi_{\text{ext}}] = \begin{bmatrix} 0 & 0 & 0 & 0 & 0 & 0 & 0 \\ 0 & 0 & 0 & 0 & 0 & F_p & 0 \\ 0 & 0 & 0 & -F_p & 0 & 0 & 0 \\ 0 & 0 & -F_p & 0 & 0 & 0 & 0 \\ 0 & 0 & 0 & 0 & 0 & 0 & 0 \\ 0 & F_p & 0 & 0 & 0 & 0 & 0 \\ 0 & 0 & 0 & 0 & 0 & 0 & 0 \end{bmatrix}$$

The strain–displacement matrix is given by

$$[B]^T = \begin{bmatrix} JN_{1,\xi} & 0 & 0 & 0 & 0 & 0 & 0 \\ 0 & JN_{1,\xi} & 0 & 0 & 0 & 0 & 0 \\ 0 & 0 & JN_{1,\xi} & 0 & 0 & 0 & 0 \\ 0 & 0 & 0 & N_1 & JN_{1,\xi} & 0 & 0 \\ 0 & 0 & 0 & 0 & 0 & N_1 & JN_{1,j} \\ JN_{2,5} & 0 & 0 & 0 & 0 & 0 & 0 \\ 0 & JN_{2,5} & 0 & 0 & 0 & 0 & 0 \\ 0 & 0 & jN_{2,5} & 0 & 0 & 0 & 0 \\ 0 & 0 & 0 & N_2 & JN_{2,\xi} & 0 & 0 \\ 0 & 0 & 0 & 0 & 0 & N_2 & JN_{2,\xi} \\ JN_{3,\xi} & 0 & 0 & 0 & 0 & 0 & 0 \\ 0 & JN_{3,\xi} & 0 & 0 & 0 & 0 & 0 \\ 0 & 0 & JN_{3,\xi} & 0 & 0 & 0 & 0 \\ 0 & 0 & 0 & N_3 & JN_{3,\xi} & 0 & 0 \\ 0 & 0 & 0 & 0 & 0 & N_3 & JN_{3,5} \end{bmatrix}$$

4.2.3 Implementation of an iterative algorithm in solving nonlinear model

In the following section, the iterative procedure using the straight forward Newton-Raphson iteration with adaptive load stepping for solving the nodal displacement incrementation solution $\{\Delta\mathbf{D}\}$ is summarized. Suppose that at increment $(i-1)$, one obtained an approximation $\{\mathbf{D}_{i-1}\}$ of the solution as the residual is not zero.

$$\{\mathbf{R}(\mathbf{D}_{i-1})\} = \{\mathbf{F}\} - [\mathbf{K}(\mathbf{D}_{i-1})]\{\mathbf{D}_{i-1}\} \neq \{0\} \tag{4.13}$$

At increment step *i*, one seeks an approximation $\{\mathbf{D}_i\}$ of the solution such that:

$$\{\mathbf{R}(\mathbf{D}_i)\} = \{\mathbf{R}(\mathbf{D}_{i-1} + \Delta\mathbf{D}_i)\} \approx \{0\} \qquad 4.14$$

The algorithm is obtained by using the first-order Taylor series in the vicinity of $\{\mathbf{D}_i\}$

$$\{\mathbf{R}(\mathbf{D}_{i-1} + \Delta\mathbf{D}_i)\} = \{\mathbf{R}(\mathbf{D}_{i-1})\} + \left[\frac{\partial\mathbf{R}}{\partial\mathbf{D}}\right]_{D=D_{i-1}} \{\Delta\mathbf{D}_i\} = \{0\} \qquad 4.15$$

The model with linearizable and incremental iterative schemes is implemented using MATLAB - the numerical computing package. An iterative equation solution is also performed. During this structural loop, the incremental-iterative algorithm will be called at each material (Gaussian) point. In every loop within an incremental loading step $\Delta\mathbf{F}$, the beam parameters

Table 4.3 and the boundary conditions are prescribed, which are the input variables to the global level routine. The equation **Eq. 4.10** gives the output results from the global level routine. It solved iteratively inside the structural level. In the elementing level sub-routine, each element are calculated to get tangently stiffness matrix $\left[\mathbf{K}_T^e\right]$ and loading vectors $\{\mathbf{F}_{\text{int}}^e\}$ and $\{\mathbf{F}_{ext}^e\}$. The superscripts *(i, k, m)* denotes respectively the global counter including the current incremental loading step, number of elements and number of Gauss integration points. After the *i* loading step(s), the converged displacement solution $\{\Delta\mathbf{D}_i\}$ at the current load $\Delta\mathbf{F}$ will be utilized for providing incremental displacement to continuously take next loading step. In material level, the convergence criterion can be defined by using **Eq. 4.11** or **Eq. 4.12,** which are expressed respectively in terms of the displacement vectors.

The nonlinear solutions for tracing load–deflection response of the model is presented as follows:

Require: Beam geometry, material properties, external loads, and model description.

Ensure: Displacement incrementation solutions $\{\Delta\mathbf{D}_i\}$ for tracing load–deflection response.

Initialize $\{\mathbf{D}\} = \{\mathbf{D}_0\}$, $\{\mathbf{R}\} = \{\mathbf{F}_{\text{int}}\} - \{\mathbf{F}_{ext}\} = \{0\}$

Loop over load increments:

for i = 1 to n_{inc} do

Find $\{\Delta F\} : \{\Delta F\} = \dfrac{i}{n_{\text{inc}}} \times F_X$ in which i is the current load increment

Call global level routine for computing $[\mathbf{K}_T]$, $\{\mathbf{F}_{ext}\}$ and $\{\mathbf{F}_{\text{int}}\}$

Solve nonlinear equation $[\mathbf{K}_T]\{\Delta\mathbf{D}_i\} - (\{\mathbf{F}_{ext}\} - \{\mathbf{F}_{int}\}) = 0$ for $\{\Delta\mathbf{D}_i\}$

Calculate $\{\mathbf{D}_i\} = \{\mathbf{D}_{i-1} + \Delta\mathbf{D}_i\}$

Calculate the criterion $\left\|\{\Delta\mathbf{D}_i\}\right\| = \left[\dfrac{\langle\Delta\mathbf{D}_i\rangle\{\Delta\mathbf{D}_i\}}{\langle\mathbf{D}_i\rangle\{\mathbf{D}_i\}}\right]^{1/2}$

Convergence check for stopping the iteration loop: $\left\|\{\Delta\mathbf{D}_i\}\right\| \le 10^{-6}$

Save the current solution $\{\mathbf{D}_i\}$ in the global solution vector $\{\mathbf{D}\}$

end for

4.3 Numerical examples

In this section, some numerical examples are carried out and the results are presented. It is noted that in all cases under consideration, the convergence study with regard to the number of elements is accomplished before extracting the results. Cantilever and simply-supported inflating composite beams loaded by compressive concentrated F are investigated. The slenderness ratio is $\lambda_s = L/\rho$ where $L = \mu l_o$ is the beam effective length. The numerical results obtained from tradtional finite element method and the IGA approach are then compared to show the accuracy and efficiency of the approach. It is noted that the C^1 continuity of the IGA elements are naturally attained due to the fundamental characteristics of IGA, therefore, it could be considered as an advantage in numerical aspects in comparision to traditional Finite element approach.

4.3.1 Linear buckling analysis

The linear buckling analysis of inflating beams under compressive concentrated load is performed to derive the critical load parameters. In order to assess the influence of the inflation pressure, the inflating beam is pressurized. To examine the linear eigen buckling behavior, the normalized linear buckling load coefficient $\left(K_c^l = 10^5 \times \sigma_{cr} / E_{eq}\right)$ proposed by Ovesy [50] is introduced, in which σ_{cr} is the linear buckling critical stress of the beam and $E_{eq} = \sqrt{E_l E_t}$ is the equivalent Young's modulus of the current material Paschero [51]. The material, geometric parameters and pressure values used for LFEIB model are given in **Table 4.1**.

Table 4.1 Input parameters for modeling LFEIB model

Natural thickness, $t_\phi (m)$		125×10^{-6}
Correction shear coefficient, k_y		0.5
Boundary condition	Simply-supported	Fixed-free
Natural radius, $R_\phi (m)$	0.08	0.08
Natural length, $l_\phi (m)$	1.15	0.65
Young modulus, E (MPa)	250	250
Poisson ratio, v	0.3	0.3
Internal pressure (kPa)	p_1	10
	p_2	20
	p_3	30
	p_4	40

4.3.1.1 Simply-supported beam

Figure 4.1 illustrates a cylindrical inflating composite beam under simply-supported constrains and subjected to axial compression load.

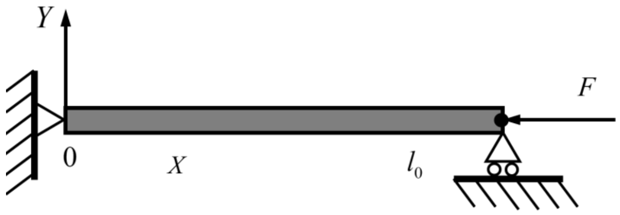

Figure 4.1 Model of a simply-supported inflating beam subjected to axial compression load.

The input paremeters are presented in **Table 4.1**. Simply-supported boundary condition is assigned by,

$u = v = 0$ at $x = 0$ and $v = 0$ at $x = l_0$

As shown in **Figure 4.2**, the convergence studies on the normalized buckling coefficient K_c^l of LFEIB model reveal that about 4 quadratic NURBS-based Timoshenko elements are sufficient to obtain converged results. These results are in a good agreement with those derived by standard 3-node Timoshenko element used by Nguyen [52]. **Table 4.2** estimates the error of numerical solutions in comparison with closed-form ones derived from analytical approach Nguyen [52]. Obviously, better results are obtained by using IGA models compared to FEM models. It should be noted that less degrees of freedom (DOFs) required to construct finite mesh of 4 quadratic NURBS-based elements (6 control points, 30 DOFs) in comparison with standard finite elementingmesh (9 nodes, 45 DOFs). As a result, IGA model significantly improves computational efforts. Moreover, the proposed approach based on IGA produces a stable solutions especially in case of large inflation pressure (case p_4=40kPa). Further, the buckling load coefficient K_c^l gradient depends on the normalized pressure p_n : at higher of p_n, the gradient of K_c^l becomes larger.

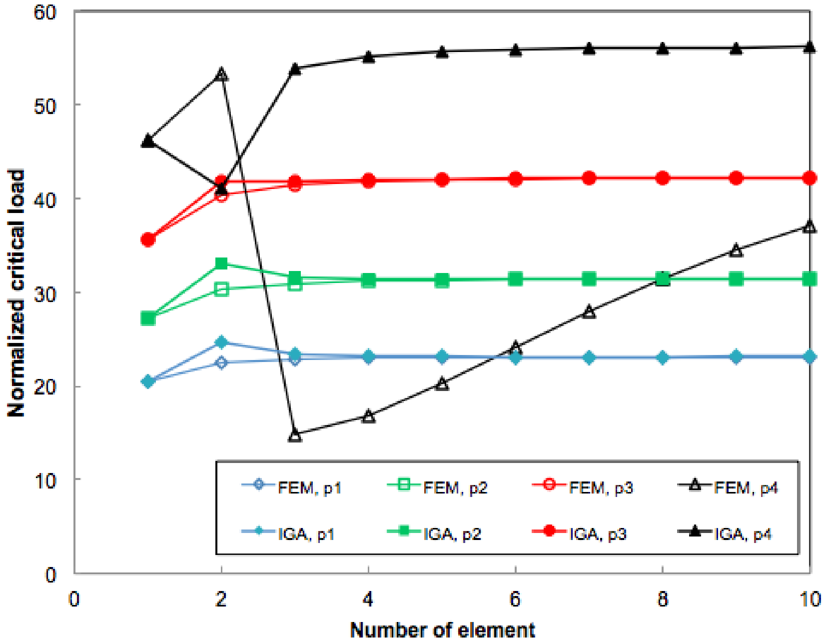

Figure 4.2 Linear eigen buckling: mesh convergence test of normalized linear buckling load coefficient $\left(K_c^l = 10^5 \times \sigma_{cr} / E_{eq}\right)$ for a simply-supported LFEIB model.

Table 4.2 Normalized critical loads K_c^l of simply-supported LFEIB inflating beam

Pressure (kPa)	**Closed-form [52] (1)**	**FEM (2)**	**IGA (3)**	**Error (%)**	
				(2) & (1)	**(3) & (1)**
10	25.31	23.11	23.12	8.69	8.65
20	33.48	31.42	31.43	6.15	6.12
30	43.27	42.22	42.22	2.43	2.43
40	54.72	31.15	56.18	43.07	2.67

*(2) & (1) denotes the differences between FEM and closed-form solutions, (3) & (1) denotes the differences between IGA and closed-form solution

4.3.1.2 Fixed – Free beam

A cantilever LFEIB model is illustrated in **Figure 4.3**.

Figure 4.3 Model of a cantilever inflating beam under axial compression load.

Material and geometric properties are assumed in **Table 4.1**. Clamped boundary condition is assigned by,

$$u = v = w = \theta_x = \theta_y = 0 \text{ at } x = 0$$

Buckling load of the cantilever inflating beam with different inflation pressures based on isogeometric analysis is plotted in the **Figure 4.4**.

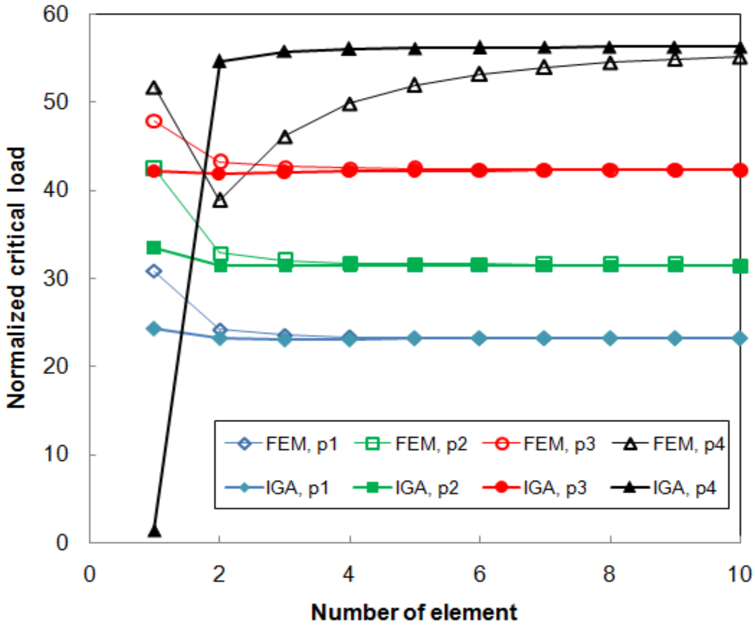

Figure 4.4 Linear eigen buckling: mesh convergence test of normalized linear buckling load coefficient $\left(K_c^l = 10^5 \times \sigma_{cr} / E_{eq}\right)$ for a cantilever LFEIB model.

The obtained results are in excellent agreement with ones derived using standard finite elementingmethods given by Nguyen [52]. Futhermore, it can be observed a fast convergence in isogeometric analysis due to the high continuity in finite elementingmesh. Addtionally, isogemetric analysis requires less total degrees of freedom (DOFs) than standard FEM and hence saving the computational effort that is significant in nonlinear analysis of the inflating composite beams.

The linear eigen buckling of the inflating composite beams is successfully obtained in the framework of NURBS-based isogeometric analysis. Numerical testings are conducted in various boundary conditions as well as geometric configurations. This reliable solution verifies the accuracy of the proposed method. The fast convergence and using less DOFs also show the robustness of the isogeometric analysis inflating composite beam models that promising in further analysis of geometric and material nonlinearity.

4.3.2 Nonlinear analysis

The critical load calculated in the linear buckling analysis above is appropriate only if there is little or no coupling between membrane deformation and bending. Consider the figure **Figure 4.5**, in which a small initial imperfection is introduced: either a slight initial curvature or a slight eccentricity of the compressive load *F*. With the increase of the initial imperfections, the beam implies large displacements rather than buckling. Hence, a linear bifurcation analysis may overestimate the actual collapse load. The normalized nonlinear load parameter at i^{th} increment of axial load is defined by,

$$K_c^{nl} = 10^6 \times \frac{F_i}{E_{eq} A_0} \tag{4.16}$$

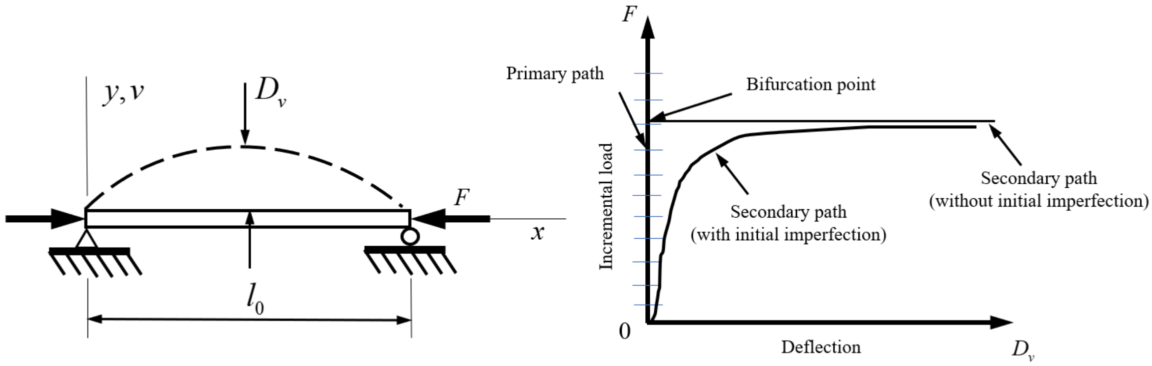

Figure 4.5 (a) Inflating beam subjected to compressive axial load *F*. (b) The effect of an initial imperfection (Nguyen [52])

The model is made up of the material 1 and 2 as defined in

Table 4.4 The deflection solutions D_v along Y axes obtained from the NLFEIB model are considered as the change in the flexion-to-radius ratio $\left(R_{fr}\right)$ as D_v / R_0, whereas the axial displacement solutions D_u along X axes are referred to the change in the length-to-radius ratio $\left(R_{lr}\right)$ as D_u / R_0. For the same normalized pressure and material properties, the smaller values of R_{lr} and R_{fr} represent the more stable beam.

Table 4.3 Input parameters for modeling models

Parameter type	Input	Physical interpretation	Value
Material properties	E_l	Young modulus in warp direction	See **Table 4.4**
	E_t	Young modulus in weft direction	
	G_{lt}	In-plane shear modulus	
	v_{lt}	Poisson ratio due to the loading in *l* direction and contraction in the *t* direction	
	v_{tl}	Poisson ratio due to the loading in *t* direction and contraction in the *l* direction	
Beam geometry (in the natural state)	l_ϕ	Length of the inflating beam	See **Table 4.4**
	R_ϕ	External radius of the inflating beam	
	t_ϕ	Thickness of the inflating beam	
External load	p	Inflation pressure	10-200 (kPa)
	F_X	Concentrated load in *X*-axis	1500 (N)

	$\{F_i\}$	Increment load vector	
	$\{n_{inc}\}$	Number of load increments	10
Model description	n_e	Number of elements	4
	e_n	Number of control points per element	3
	n_n	Number of control points in global	$n_e + \deg$
	n_{dof}	Number degrees of freedom per node	5
	e_{dof}	Number degrees of freedom per element	$e_n.n_{dof}$
	g_{dof}	Number of global degrees of freedom	$n_{dof}.n_n$
	m	Number of Gauss integration points	3

Table 4.4 Data set for inflating beam

Natural thickness, $t_\phi(m)$		5×10^{-4}
Correction shear coefficient, k_y		0.5
Natural radius, $R_\phi(m)$		0.14
Natural length, $l_\phi(m)$		3
Orthotropic fabric's mechanical properties:	Material 1 (Exp.)	Material 2 (Cheng et al.(2009))
Young modulus in warp direction, E_l (MPa)	2609	19300
Young modulus in weft direction, E_t (MPa)	2994	14240
In-plane shear modulus, G_{lt} (MPa)	1171	6450
Poisson ratio, v_{lt}	0.21	0.28
Poisson ratio, v_{tl}	0.18	0.22

Table 4.5 Normalized pressure $\left(p_n\right)$ for different values of internal pressure $\left(p\right)$ used in the study.

p (kPA)		p_n	
		Material 1	**Material 2**
p_1	10	324	43
p_2	20	648	85
p_3	30	972	128
p_4	40	1295	171

4.3.2.1 Simply-supported beam

In this problem, the nonlinear buckling of a simply supported inflating beam subjected to an axial compressive load F is investigated by the procedure proposed in **Section § 4.2.2**. The numerical examples contain large deformation analyses of NLFEIB model and illustrate the performance of the derived algorithm. A parametric study is carried out for studying the influence of normalized pressure on the NLFEIB model. At each level of normalized pressure, the corresponding crushing load $\left(F_{crush} = F_p\right)$ is the upper bound of the axial load applied to the beam. The displacements at the middle span of the beam are extracted from the global solution.

Figure 4.5 and **Figure 4.6** show the variation of flexion-to-radius ratio and length-to-radius ratio with increments of normalized load parameter K_c^{nl} in two cases of material. It is noted from the linear buckling analysis that 4 elements are sufficient to obtain converged results. At low pressure the model is unstable and therefore will fail first. At higher pressures, the R_{fr} ratio responses are quasi-linear for low increments of K_c^{nl}. The curves become nonlinear gradually at higher K_c^{nl}.

In another parametric study, the influence of the fabric properties in conjunction with the effect of the normalized pressure is pointed out. Two HOWF inflating beams made of material 1 and 2 are considered. As mentioned in **Section § 4.3**, the nonlinear iterative solutions are obtained with inputs of normalized pressure and are normalized by two aspect ratios R_{lr} and R_{fr}.

The effects of boundary condition and material properties are clearly illustrated by the responses of simply-supported (SS) inflating beams. In case of material 1 which has low elastic modulus than material 2, the buckling of SS beam is more sensitive at high level of internal pressure. It appears mode jump behavior when the beam withstanding increasing axial compression loads. In contrary, the distortion in load-deflection does not happen in the configuration of clamped inflating beams.

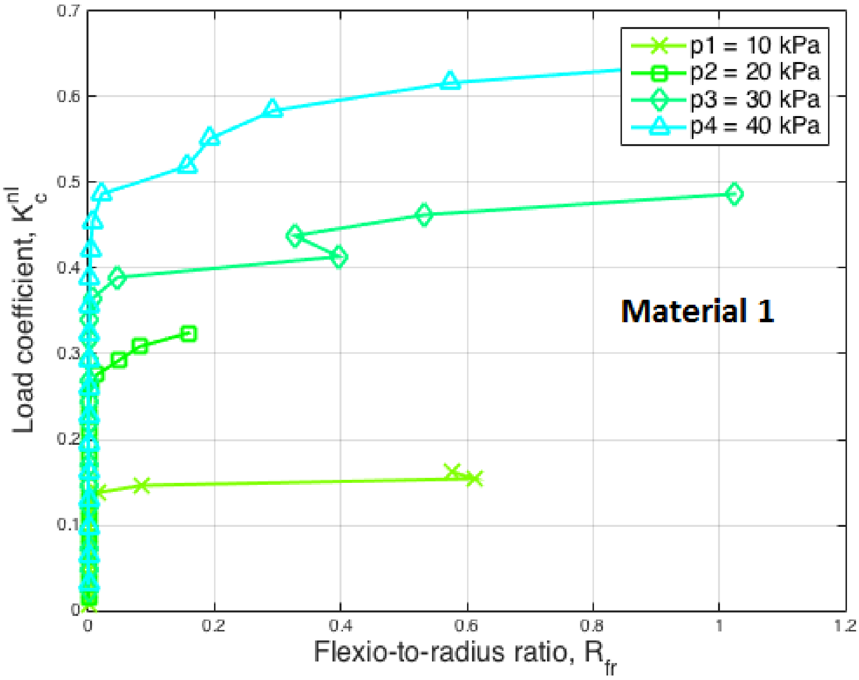

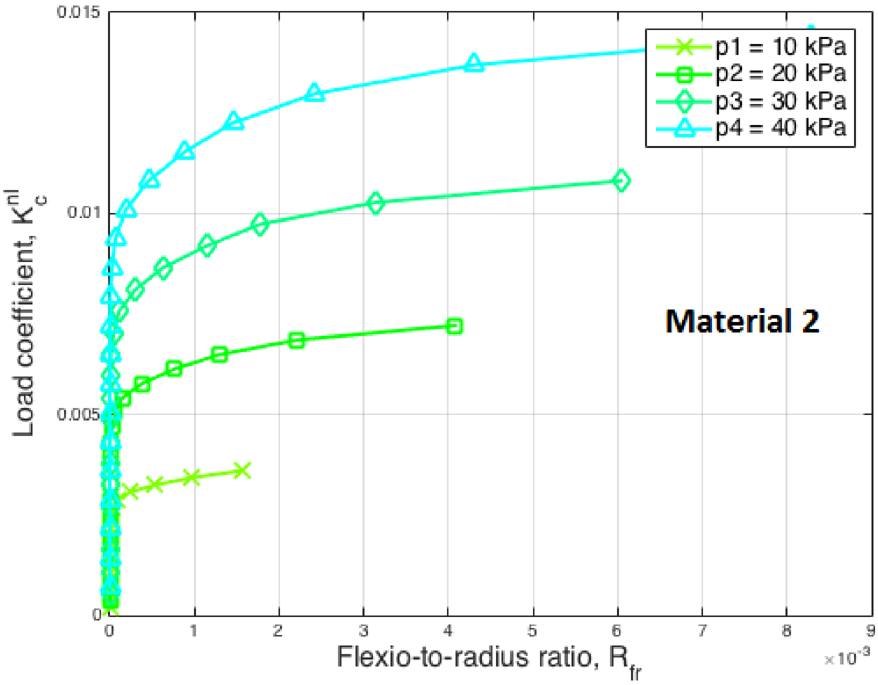

Figure 4.6 Nonlinear buckling: variation of flexion-to-radius ratio $\left(R_{fr} = D_v / R_o\right)$ with increasing normalized nonlinear load parameter $\left(K_c^{nl} = 10^6 \times F_i / \left(E_{eq} A_0\right)\right)$ for a simply supported NLFEIB model.

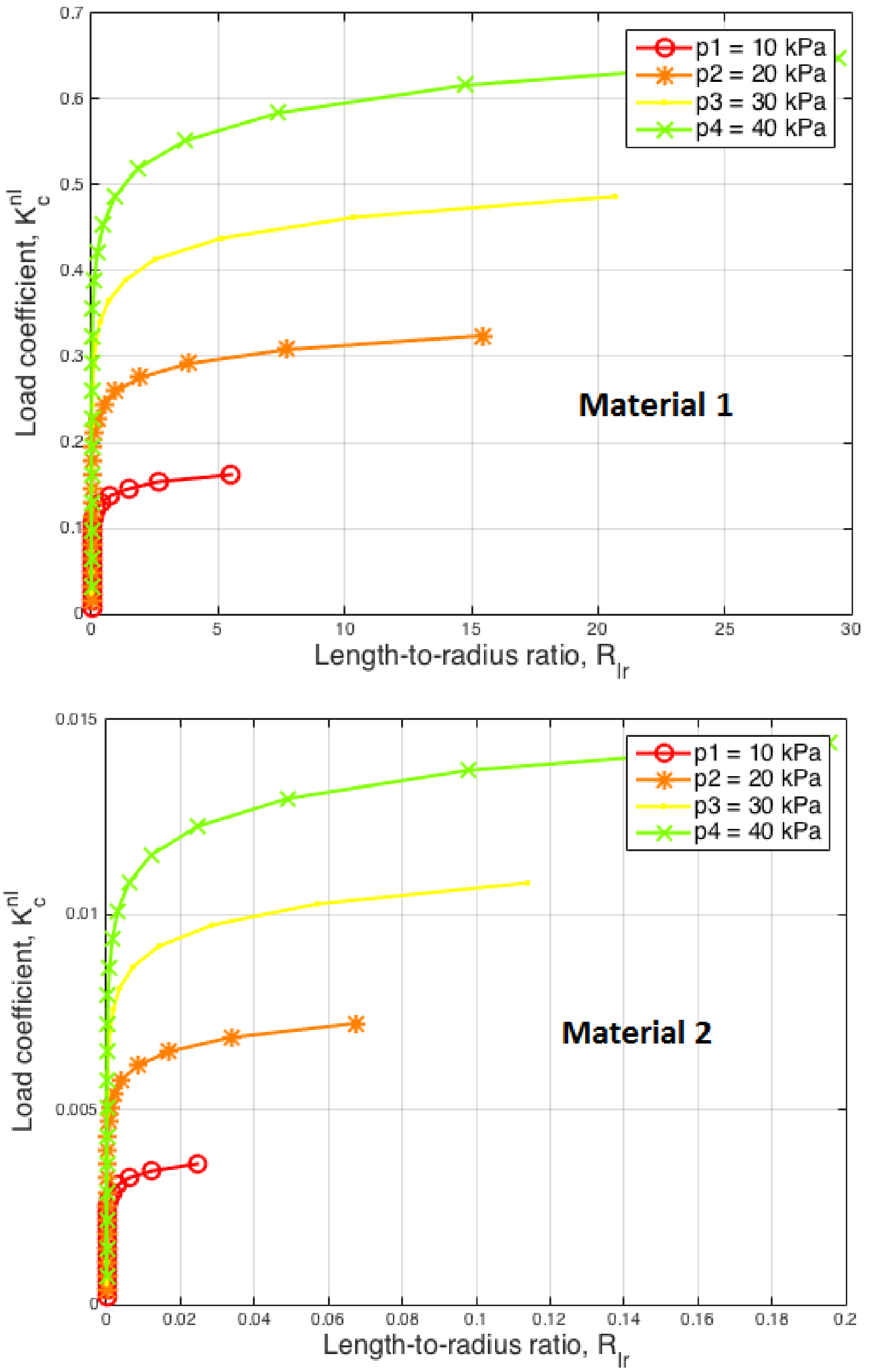

Figure 4.7 Nonlinear buckling: variation of length-to-radius ratio $\left(R_{lr} = D_u / R_o\right)$ with increasing normalized nonlinear load parameter K_c^{nl} for a simply supported NLFEIB model.

4.3.2.2 Fixed-free beam

In this example, the nonlinear buckling of a cantilever inflating beam subjected to an axial compressive load F is investigated. The discrepancy due to the normalized pressure between the results is clearly shown. The variation of flexion-to-radius ratio with increments of normalized load parameter K_c^{nl} in two cases of material is given in **Figure 4.7**. Additionally, **Figure 4.8** presents length-to-radius ratio R_{lr} versus the incremental load ratio K_c^{nl}. The results show that the beam pressurized to higher pressures exhibits a better load-carrying capacity (more stable).

It is also shown that in both cases of normalized pressure, the beams made of high moduli fabric (material 2) exhibit more stability (lower values of R_{lf} and R_{fr}). The comparison between the beam response curves in two different inputs of normalized pressure also illustrates well that the beams with higher normalized pressures have the larger limits of R_{lr} and R_{fr} ratios before crushing than those with lower pressures. This is attributed to the fact that once the tows are sufficiently stressed, the inflating beam possesses flexural stiffness capable of resisting a combination of direct compressive stress and bending.

Again, the nonliear buckling of inflactable composite beams is successfully obtained by using isogeometric analsys model. In this section, the variation of not only boundary condition but also material is taken into acount and the numerical algorithm sucessfully traced the load-deflection response of inflating beams.

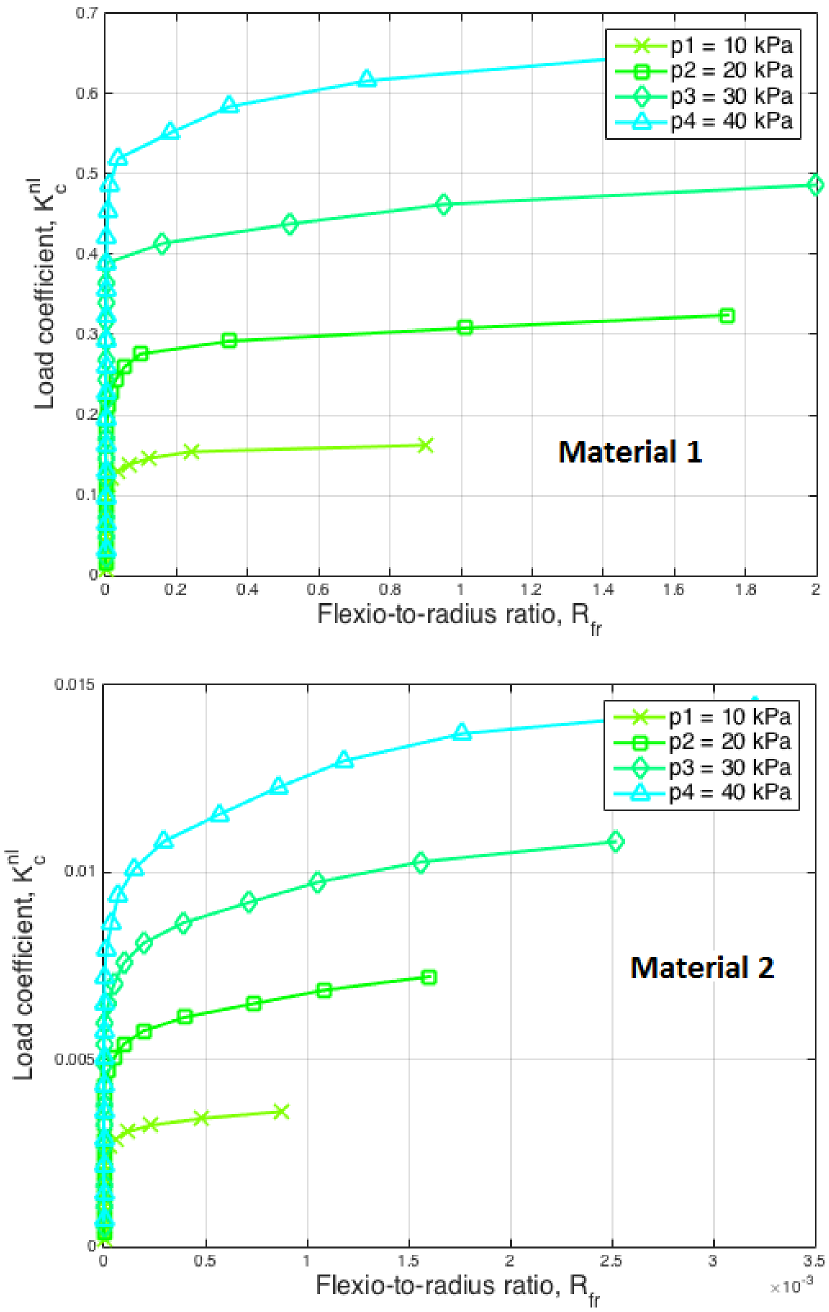

Figure 4.8 Nonlinear buckling: variation of flexion-to-radius ratio $\left(R_{fr} = D_v / R_o\right)$ with increasing normalized nonlinear load parameter $\left(K_c^{nl} = 10^6 \times F_i / \left(E_{eq} A_0\right)\right)$ for a cantilever beam.

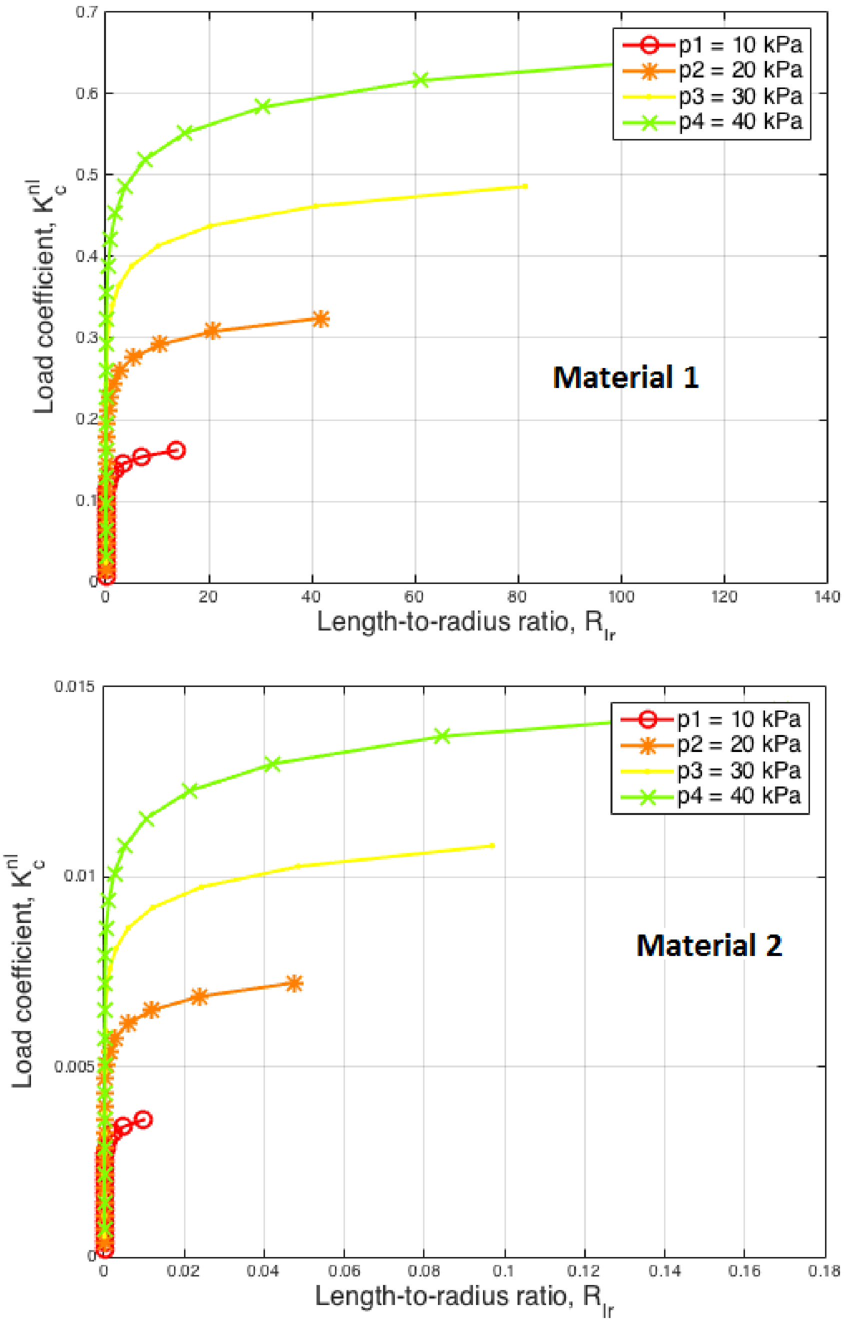

Figure 4.9 Nonlinear buckling: variation of length-to-radius ratio $\left(R_{lr} = D_u / R_o\right)$ with increasing increasing normalized nonlinear load parameter K_c^{nl} for a cantilever beam

4.4 Conclusions

In this chapter, the linear and nonlinear buckling analyses of inflating beam are conducted. The governing equations are derived based the energy approach that the changing in membrane energy and the bending strain energy accounted. The governing equations are then are discretized based on the IGA approach, in which the NURBS basis functions are used to construct exact geometry and act as interpolation functions.

In the linear buckling analysis, a mesh convergence test on the beam critical force showed the significant improvement of the proposed numerical model in comparison with standard finite element method. The results on the buckling coefficient were also in a good agreement with those available in literature. In the nonlinear buckling analysis, the method sucessfully traced the load-deflection response of inflating beams.

Two methods FEM and IGA have been applied to verify the numerical method for the inflating beam model. A simple beam model was simulated and calculated. The IGA method shows that building numerical models for the problem is relatively more accurate.

CHAPTER 5: BUCKLING EXPERIMENTS OF INFLATING BEAMS

5.1 Introduction

This chapter presents methodologies of materials selection and prototyping procedure. An experimental program for buckling behavior of inflating beams fabricated from woven fabric composites is presented, in which various values of internal pressure is also considered. The chapter begins with a brief review of buckling of thin-walled shell structures, followed by the material test of woven fabric composites. After that, the fabrication procedure of inflatable beams and the buckling testing setup are described in detail. Discusion and remarks on the results obtained are then given. In addition, the experimental results is used to calibrate the numerical model of inflatable beams to predict the buckling behaviour of the beam fabricated from orthogonal fibre laminated fabrics. The objective of the experiment and acquisition data include:

- Determine the load-displacement relation of the inflatable beam with different air pressures.

- Determine the maximum load-carrying capacity of the inflatable beam with respect to the appearance of the first wrinkle.

5.2 Material properties and selection of fabrics

Due to real conditions in Vietnam, several fabrics types are used to make the air beams but there are not enough techinical specifications. Therefore, before the air beams are proceeding to fabricate, the mechanical properties of the selected fabrics definitely be checked.

The mechanical properties of woven fabrics are examined prior to fabricating inflatable beams. The test procedure is based on ASTM-D638/Form IV as recommended, see **Table 5.1**, and following steps are adopted:

Step 1: Cut dog-bone shape specimens in longitudinal and transverse directions.

Step 2: Conduct axial tensile test for determining elasic modulus and ultimate tensile strength of the fabrics.

Table 5.1 Criteria and method for experiment of composite fiber

No.	Criteria	Experiment method	Unit
1	Thickness standard	ASTM-D5199	mm, mil
2	Proportion	ASTM-D792	kg/m^3
3	Tensile strength at break limitation Elastic module	ASTM-D638/Form IV	KN/m
4	Tensile strength at bending limitation	ASTM-D638/Form IV	KN/m
5	Stretch ratio at break limitation	ASTM-D638/Form IV	%
6	Stretch ratio at bending limitation	ASTM-D638/Form IV	%
7	Strength of puncture resistance	ASTM-D4833	N
8	Strength of tearing resistance	ASTM-D1004	N
9	Carbonate ratio	ASTM-D1603	%

5.2.1 The woven fabric materials

Table 5.1 shows some of fabric composite materials available in the market which can the used for making inflatable beams. Two of them in **Table 5.2** are widely used to make inflatable component are chosen for material tests.

Figure 5.1 Fabric type

Figure 5.2 Waterproof PVC Laminated Tarpaulin and Coated Vinyl Fabrics

The dog-bone shape coupon for tesile test has the geometric dimensions presented in **Figure 5.3** and **Table 5.3**.

Hydraulic Press Mold was employed to cut the dog-bone shape coupons. The equipment consists of a Toggle Press for Cutting Dies and Cutting Dies shown in **Figure 5.4**.

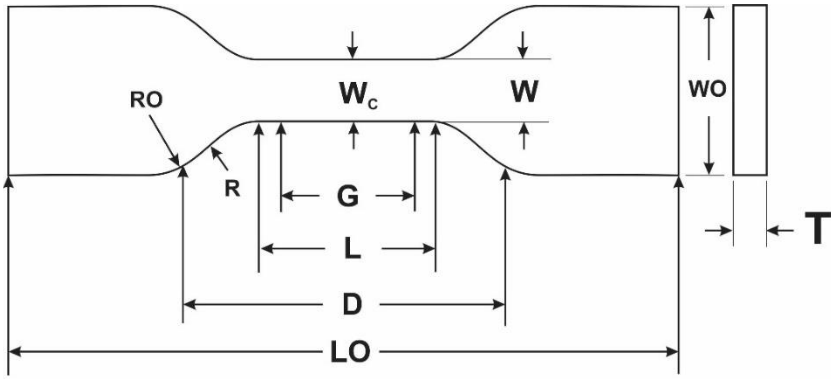

Figure 5.3 Samples after made looked like barbel

Thickness, T, shall be 0.5 ± 0.4 mm for type of molded specimen.

Table 5.2 Dimension of sample measurement

Notation	Description	Value (mm) (Type IV)
W	Section's width	6 ± 0.5
L	Section's length	33 ± 0.5
WO	Overall width	19 ± 6.4
LO	Overall length	≥ 115
G	Length measurement	25 ± 0.13
D	Distance between 2 vices	65 ± 5
R	Internal diameter	14 ± 1
RO	External diameter	25 ± 1

(a)

- Tensile Force: 20 kN
- Opening: 0-30mm
- Clamping Surface Size: 50x60mm, 50x100mm
- Clamping Surface: Plain, Rubber, Wave, Serrated

(b)

- Tensile Force: 20 kN
- Opening: 0-30mm
- Clamping Surface Size: 50x60mm, 50x100mm
- Clamping Surface: Plain, Rubber, Wave, Serrated

Figure 5.4 Cutting Dies: (a) Toggle Press for Cutting Dies, (b) Cutting Dies

The dog-bone tensile test samples after cutting are shown in **Figure 5.5**. The first fabric is made of Waterproof PVC Laminated Tarpaulin, and the second fabric is made of Coated Vinyl Fabrics.

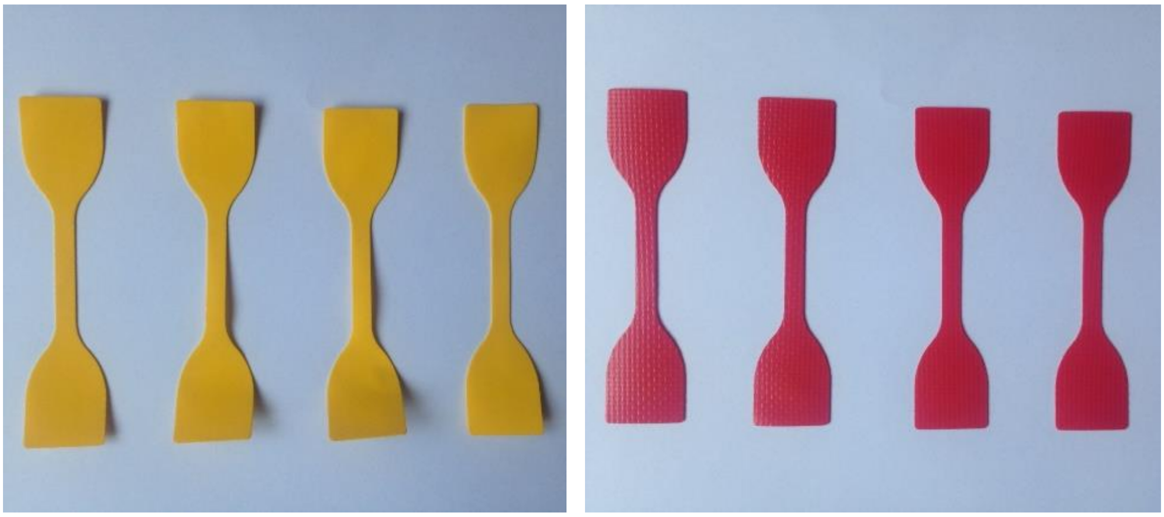

(a) (b)

Figure 5.5 Samples were cut with flat form: (a) Sample 01, (b) Sample 02

5.2.2 Testing equipments

The tensile test is conducted using the Instron 8801 Series Servohydraulic Fatique Testing Machine as presented in **Figure 5.6**.

Figure 5.6 Instron 8801 Series Servohydraulic Fatique Testing Machine.

(Location: National Key Lab. of Polymer & Composite Materials – Ho Chi Minh City University of Technology)

The testing procedure is following the guidance of ASTM D638 which covers the determination of the tensile properties of unreinforced and reinforced plastics in the form of standard dumbbell-shaped test specimens when tested under defined conditions of pretreatment, temperature, humidity, and testing machine speed, namely Speed of Testing: (5mm/min), Room temperature (25^0C), Humidity (<50%). In this method, sample with rectangle section was clamped into two vices of pulling tool. It would be pulled until broken. The tensile tests are shown in **Figure 5.7**.

(a) (b)

Figure 5.7 Tensile test for (a) sample 01 and (b) sample 02

5.2.3 Mechanical properties of woven fabric composites

The tensile dog-bone samples are cut in longitudinal as well as tranverse directions. Tensile test is repeated five times for each material in each cut-direction. The test results are presented in **Table 5.3** and **Table 5.4**.

Table 5.3 shows the material properties in longitudinal axis of the first woven fabric composite. It can be seen that the average ultimate tensile force was 290.36 N with respect to an average longitudinal extension of 11.37 mm, corresponding to the ultimate tensile strength in longitudinal axis of the first fabric of 73.32 MPa and the elastic modulus is 314.27 MPa.

Table 5.4 shows the material properties in longitudinal axis of the second woven fabric composite. It can be seen that the average ultimate tensile force was 139.01 N with respect to an average longitudinal extension of 22.36 mm, corresponding to the ultimate tensile strength in longitudinal axis of the second fabric of 35.01 MPa and the elastic modulus is 51.61 MPa.

Table 5.3 Result of sample 1's longitudinal grain

No.	Maximum Load (N)	Tensile stress at Maximum Load (MPa)	Tensile extension at Maximum Load (mm)	Modulus (E-modulus) (MPa)
1	286.770	72.417	11.357	246.347
2	268.829	67.886	10.432	275.595
3	332.427	83.946	12.387	383.451
4	275.540	69.581	11.679	186.772
5	288.248	72.790	10.984	479.192
Average	290.36	73.32	11.37	314.27

Table 5.4 Result of sample 2's longitudinal grain

No.	Maximum Load (N)	Tensile stress at Maximum Load (MPa)	Tensile extension at Maximum Load (mm)	Modulus (E-modulus) (MPa)
1	149.0831	37.6473	22.9861	42.0379
2	146.6751	37.0392	22.5536	49.1538
3	137.6748	34.7664	22.7325	59.1013
4	129.7951	32.7765	22.6066	53.9681
5	131.8216	33.2883	22.3945	53.7952
Average	139.01	35.10	22.65	51.61

The relation between the axial forces and the extensions of the sample is presented in **Figure 5.8** and **Figure 5.9**. For the first fabric, the load-extension curve is nonlinear as the load below 50 N, but when the load is increasing, the curve becomes linear until its failure. It also can be seen that the tensile strength of the first (yellow) fabric is much stronger than the the second (red) fabric.

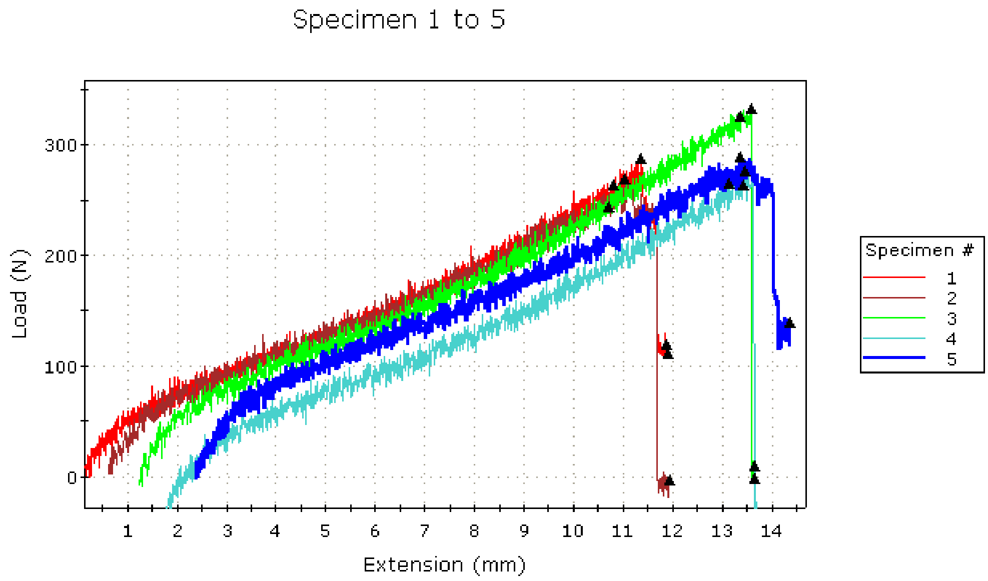

Figure 5.8 Graph of tensile strength of sample 1's longitudinal grain

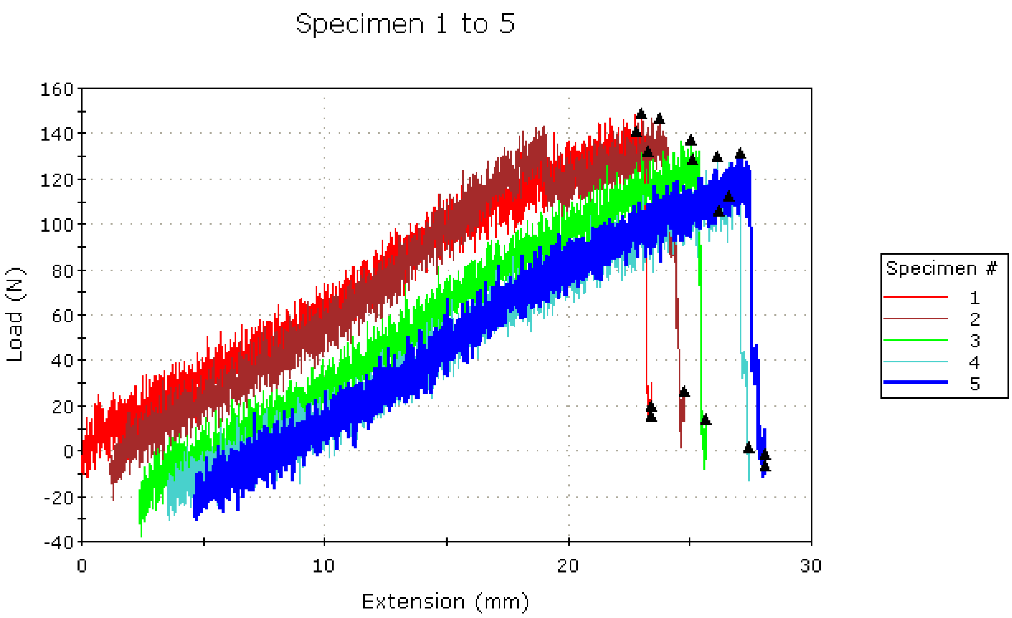

Figure 5.9 Graph of tensile strength of sample 2's longitudinal grain

Next, the tensile dog-bone samples cut in transverse grain are tested. The test results are presented in **Table 5.5** and **Table 5.6**.

The material properties in transverse axis of the first woven fabric composite are presented in **Table 5.5**. It can be seen that the average ultimate tensile force was 252.81 N with respect to an average transverse extension of 16.89 mm, corresponding to the ultimate tensile strength in transverse axis of the first fabric of 63.84 MPa and the elastic modulus is 246.06 MPa.

Table 5.6 presents the properties in transverse axis of the second woven fabric composite. It can be seen that the average ultimate tensile force was 151.10 N with respect to an average transverse extension of 16.16 mm, corresponding to the ultimate tensile strength in longitudinal axis of the second fabric of 38.16 MPa and the elastic modulus is 56.29 MPa.

Table 5.5 Result of sample 1's horizontal grain

	Maximum Load (N)	**Tensile stress at Maximum Load (MPa)**	**Tensile extension at Maximum Load (mm)**	**Modulus (E-modulus) (MPa)**
1	280.0942	70.7309	17.1736	637.7190
2	233.6860	59.0116	16.8591	72.2702
3	262.2843	66.2334	17.6091	79.5614
4	227.7255	57.5064	16.7840	115.0650
5	260.2816	65.7277	16.0069	325.6821
Average	252.81	63.84	16.89	246.06

Table 5.6 Result of sample 2's horizontal grain

	Maximum Load (N)	**Tensile stress at Maximum Load (MPa)**	**Tensile extension at Maximum Load (mm)**	**Modulus (E-modulus) (MPa)**
1	147.7361	37.3071	14.9831	68.3675
2	144.7439	36.5515	16.3522	67.3319
3	159.8239	40.3596	16.3607	47.4520
4	141.7041	35.7839	15.7577	49.8744
5	161.4928	40.7810	17.3269	48.4138
Average	151.10	38.16	16.16	56.29

Figure 5.10 and **Figure 5.11** demonstrate the load-extension relations of the first and second fabrics respectively. Similar to longitudinal axis, the load-extension relation become linear after a certain low value of extension. The linear relation develops until the fracture occurring suddenly without an obvious warning.

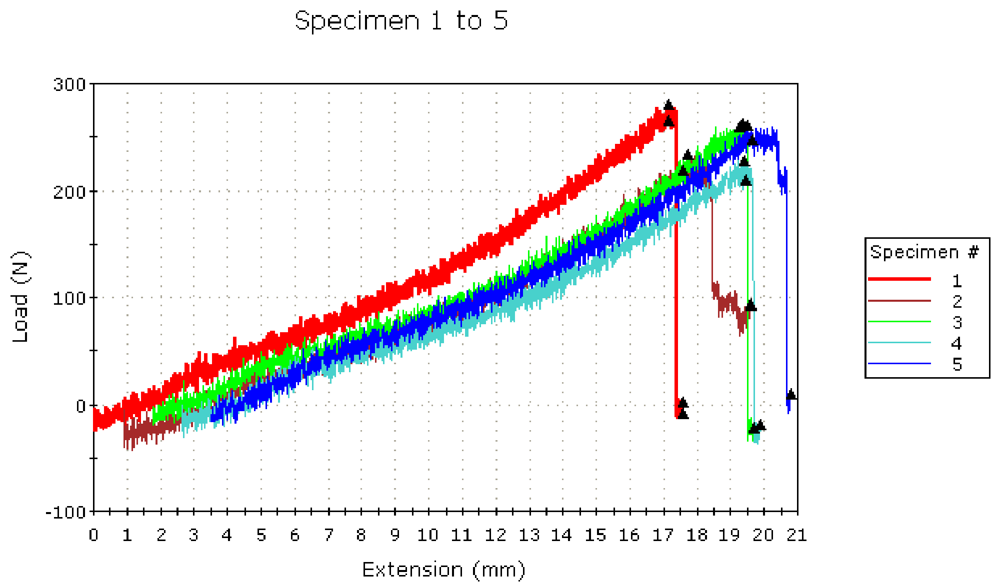

Figure 5.10 Graph of tensile strength of sample 1's horizontal grain

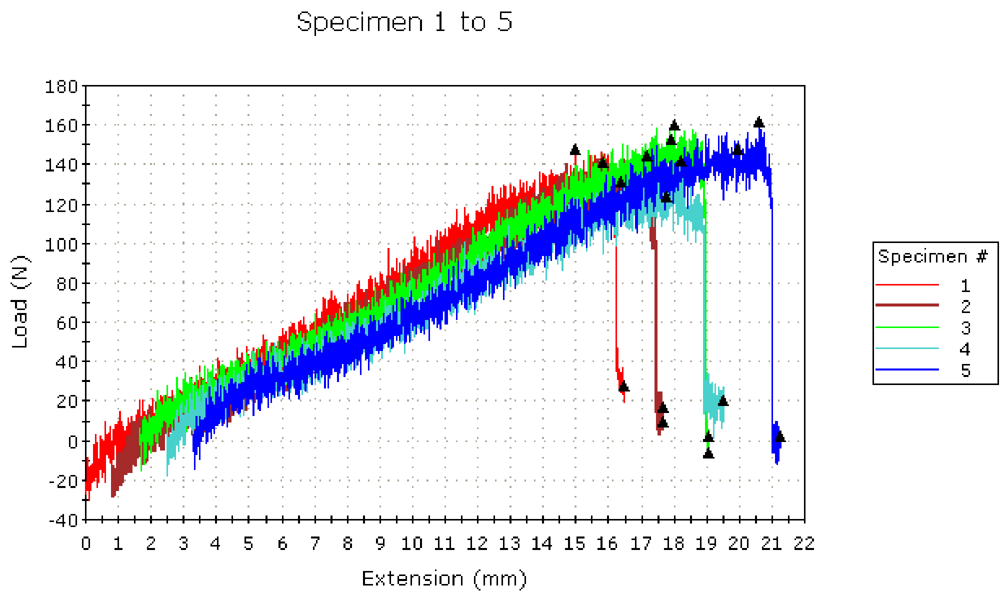

Figure 5.11 Graph of tensile strength of sample 2's horizontal grain

From the material tests, it can be seen that the first fabric has much higher tensile strengths in both longitudinal and transverse directions. Also, the leastic modula of the first (yellow) fabric in longitudinal and transverse axes are approximately five times the ones of the second (red) fabric. Therefore, the first fabric is to be the material for fabricating the inflatable beam specimens.

5.3 Test of joint’s durable strength

To fabricate inflatable beam specimens which meet engineering and aesthetic requirements, a special technology process to join fabric edges together is very important. To avoid air leaking under high pressure. In this study, two methods making fabric joints are investigated:

1) Glued joint.

2) Glued joint with thermal attachment.

Glued joint:

Firstly, a thin layer of PVC glue of approximately 15 µm was applied on the joined areas, then wait for 2 minutes for the glue to be settled. Secondly, lay the contact surfaces on each other and apply a compression force of 10 N until the glue being cured. Next, check if the joint has any defects: exessive of glues out of the joint areas, air bubbles, tears, etc; if not, redo the joint.

Glued joints with thermal attachment:

Firstly, a thin layer of PVC glue of approximately 15 µm was applied on the joined areas, then wait for 2 minutes for the glue to be settled. Secondly, lay the contact surfaces on each other and apply a compression force of 10 N and impose a heat of 100^0 C on the joint until the glue being cured. Next, check if the joint has any defects: exessive of glues out of the joint areas, air bubbles, tears, etc; if not, redo the joint.

Currently, there is not any study to determine which distance (d) is properly suitable for stacking joint and what method should be used to enhance joint’s durability, thus this experiment will use samples created following different methods and distinct joint’s widths so as to seek an optimal methodology of making joints and joint’s dimensions with the best durability. Besides, joint’s dimensions do not affect the process of making inflatable beam and the next experiments’ results.

Measure durability of 180^o flat joint (ASTM D903). This test method covers the determination of the comparative peel or stripping characteristics of adhesive bonds when tested on standard-sized specimens and under defined conditions of pretreatment, temperature, and testing machine speed. Preparation of Test Specimen:

Bond area by adhesive with pressure and heat. Testing Conditions: - Room Temperature: 25 ± 2^{0}C - Humidity: 50 ± 5% - Testing speed: 5 mm/min.

In order to choose the proper size of the glued joint and assess the quality og the glued joint, the glued joint test samples are fabricated as in **Figure 5.12**, in which: a is the grip length, b is the original length, d is the glued length and c is the width of the joint. The actual dimensions are provided in **Table 5.7**, with d taken as 1cm, 2cm và 2.5cm.

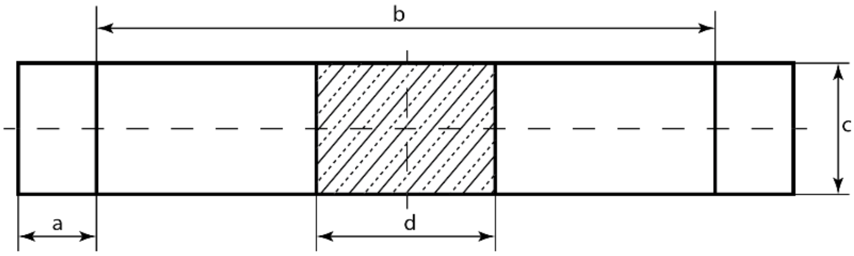

Figure 5.12 Shape of Samples: Test Specimen

Table 5.7 Sample's measurement. Sample dimensions (mm)

Distance of grip, a	15
Distance between of grips, b	$(40 \div 45) \times 2 + d$
Length of bond line, d	as required by each experiment
Width of specimen, c	25

5.3.1 Glued joint PVC 1cm

After the glued joint samples are made, the assessment of the glued joint is investigated by tensile test. Similar to the material test, the glued joint test also is taken with five samples.

Figure 5.13 presents the test results of glued joint without imposing heat. It can be seen the fracture occurred at the glued joint because the bonding of two surfaces in 1 cm length is not as strong as tensile strength of the fabric.

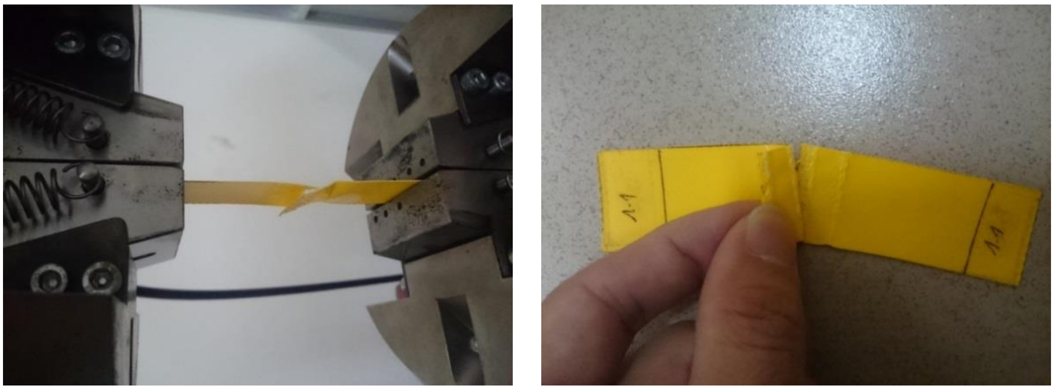

Figure 5.13 Glued joint test of 1 cm length

Figure 5.14 shows the load-extension relation of the glued joint sample with 1 cm length connection, and the

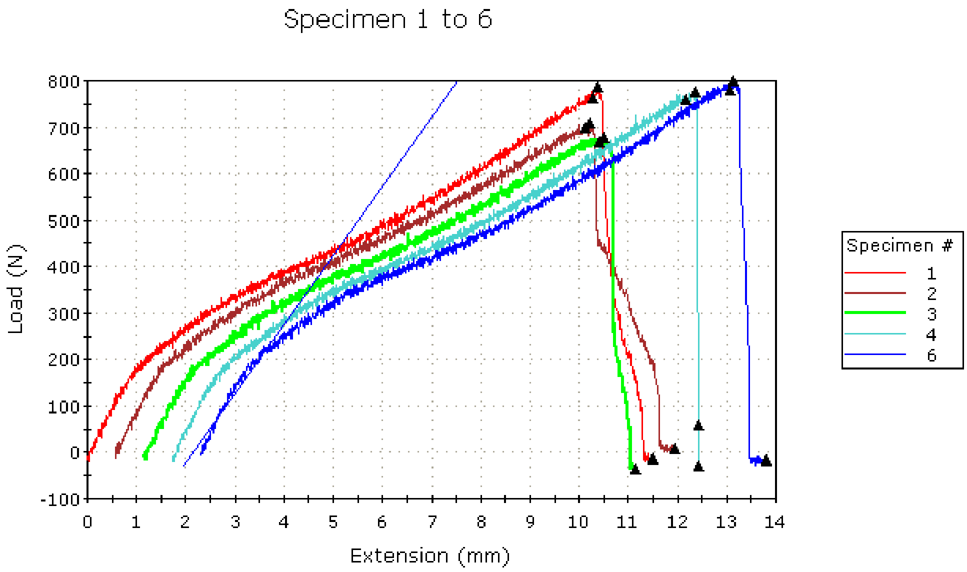

Figure 5.14 Glued joint PVC 1cm

Table 5.8 presents the result data. It can be seen that the joint was delaminated the load of 731 N, and the average tensile strength of the glued joint was 24.4 MPa which far lower and one of origin material (73.32 MPa). Accordingly, the glued joint area of 1 cm without thermal treatment is not adequate.

Table 5.8 Result of Glued joint PVC 1cm

	Maximum Load (N)	**Tensile stress at Maximum Load (MPa)**	**Tensile extension at Maximum Load (mm)**	**Modulus (E-modulus) (MPa)**	**Force/Width, N/mm**
1	785.160	26.172	10.389	220.560	785.160
2	707.126	23.571	9.644	221.692	707.126
3	677.049	22.568	9.371	218.432	677.049
4	774.992	25.833	10.640	205.948	774.992
6	799.286	26.643	10.824	219.006	799.286
Average	731.989	24.400	9.999	214.692	731.989

5.3.2 Glued joint PVC 1cm thermal

Similar to the previous test, the glued joint PVC 1 cm thermal was also fractured at the connection as can be seen in **Figure 5.15**. Therefore, the glued joint needs to be extened.

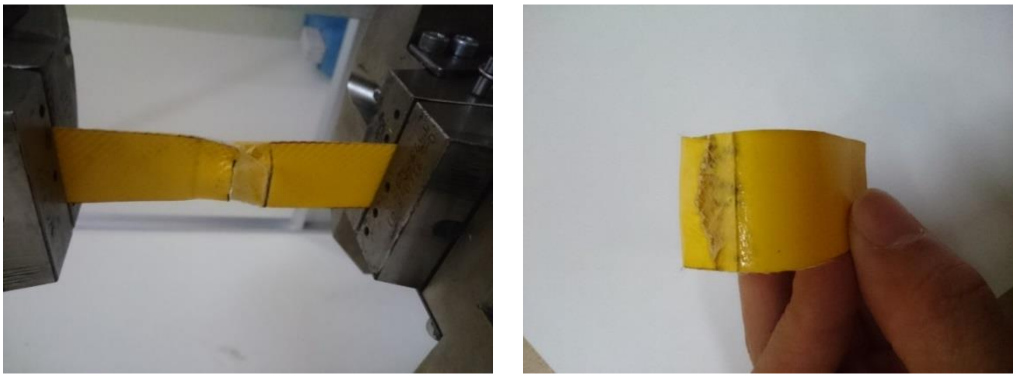

Figure 5.15 Experiment result

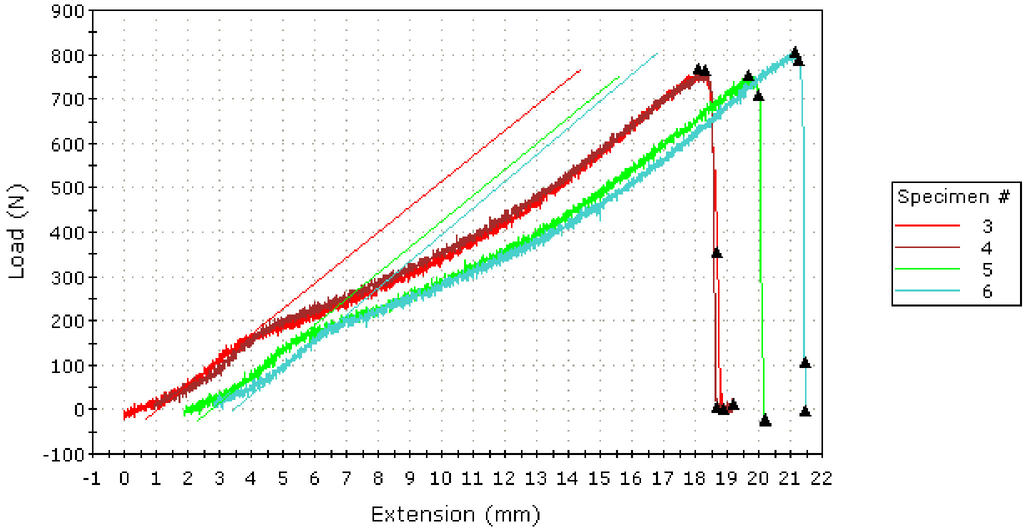

Figure 5.16 Glued joint PVC 1cm thermal

Table 5.9 Result Glued joint PVC 1cm thermal

	Maximum Load (N)	**Tensile stress at Maximum Load (MPa)**	**Tensile extension at Maximum Load (mm)**	**Modulus (E-modulus) (MPa)**	**Force/ Width, N/mm**
3	766.945	25.565	18.081	157.767	30.678
4	764.585	25.486	17.370	147.115	30.583
5	754.797	25.160	17.790	154.386	30.192
6	804.996	26.833	18.318	149.532	32.200
Average	772.831	25.761	17.890	152.200	30.913

5.3.3 Glued joint PVC 2cm thermal

For the glued joint PVC 2cm with imposing heat, the fracture was also occurred at the connection as shown in **Figure 5.17** and **Figure 5.18** with test data provided in **Table 5.10**.

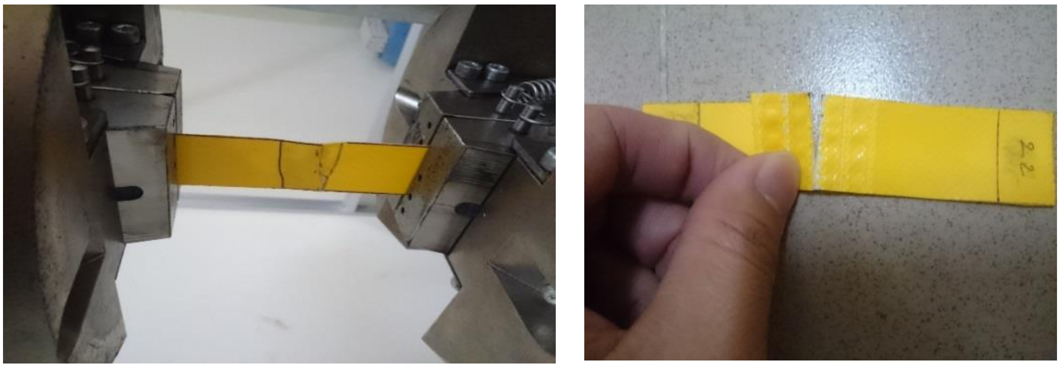

Figure 5.17 Experiment result

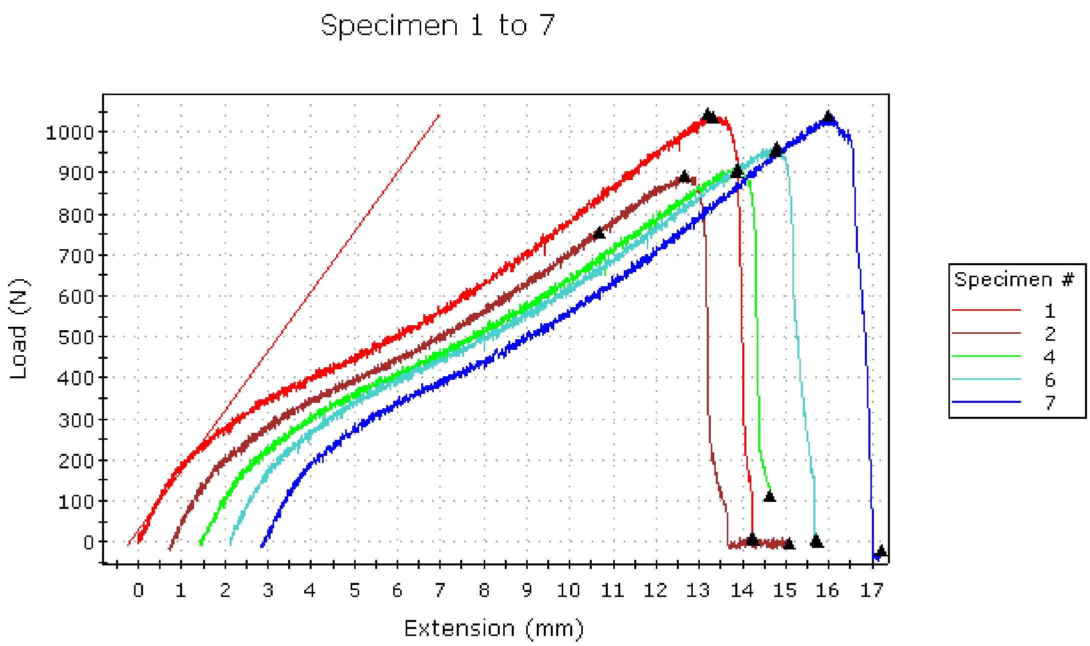

Figure 5.18 Glued joint PVC 2cm thermal

Table 5.10 Result of Glued joint PVC 2cm thermal

	Maximum Load (N)	Tensile stress at Maximum Load (MPa)	Tensile extension at Maximum Load (mm)	Modulus (E-modulus) (MPa)	Force/ Width, N/mm
1	1041.496	34.717	13.204	252.495	41.660
2	894.153	29.805	11.955	215.143	35.766
4	909.185	30.306	12.487	211.563	36.367
6	960.720	32.024	12.677	239.693	38.429

7	1039.243	34.641	13.148	207.452	41.570
Average	968.959	32.299	12.694	225.269	38.758

5.3.4 Glued joint PVC 2.5 cm with thermal attachment

The glued joint is extended to 2.5cm long and imposed thermal attachment. It can be seen that the joint is acceptable as the failure was occurred outside the overlapped joint. From consequence above, joints applied PVC glue and thermal attachment would improve much more when compared with the normal method (examined through force/width unit. Method using PVC glue and thermal attachment was better durable than normal one. To reinforce joint's strength, the method using PVC glue and thermal attachment (overlapped edges 2.5cm).

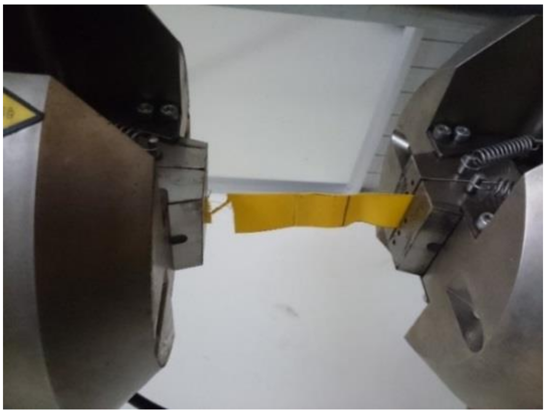

Figure 5.19 Experiment result

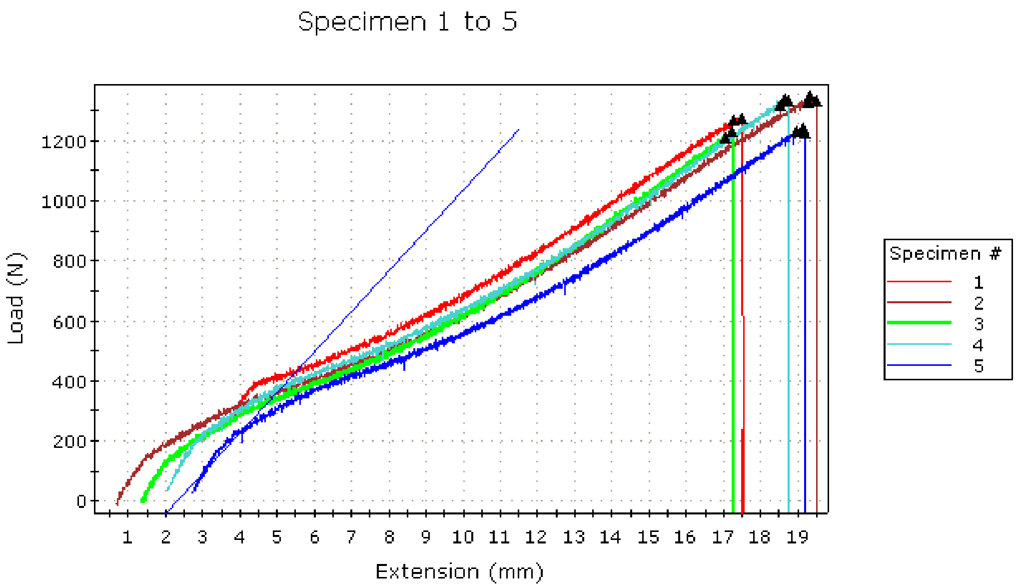

Figure 5.20 Glued joint PVC 2.5cm thermal

Table 5.11 Result of Glued joint PVC 2.5cm thermal

	Maximum Load (N)	**Tensile stress at Maximum Load (MPa)**	**Tensile extension at Maximum Load (mm)**	**Modulus (E-modulus) (MPa)**	**Force/Width, N/mm**
1	1275.480	42.516	17.508	652.449	51.019
2	1347.470	44.916	18.637	179.301	53.899
3	1229.393	40.980	15.878	181.337	49.176
4	1340.795	44.693	16.605	263.935	53.632
5	1242.626	41.421	16.381	245.781	49.705
Average	1287.153	42.905	17.002	304.560	51.486

5.4 Inflatable beam specimens

It is necessary to depend on the available fabric sizes in Vietnamese market and experimental experiences so that it can match the initial experimental conditions.

The fabrication of specimens requires extra cares to avoid air leaking. Firstly, the beam body is constructed by joining the fabric along the length of the cylinder with the glued PVC 2.5 cm joint. To connect the cap of the beam to cylinder body is more complicated. The geometric dimnesions of the inflatable beam specimens with cylinder form has parameters as below:

Natural length: L = 200cm (excluding 2 caps at its 2 ends)

Natural outer Radius: R = 10cm

Following tensile and stick experiment’s data, sample 1’s material (yellow fiber) was chosen for processing design of Inflatable beam samples. Method using PVC glue and thermal pressure 2.5cm. Two caps at two ends need machining so that they are very close, glued or sewed joining area can be suffered pneumatic pressure. Therefore, deployment may run into some issues, those are joint’s errors that make air leaking outside beam. Thus, sticking process must be done carefully, an amount of glue is absolutely enough, and the imposing heat must be correct so as to their unification.

Structure of 2 valves of pumping and manometer at the position 20cm from beam's end. One should be located far from another (60^0-90^0).

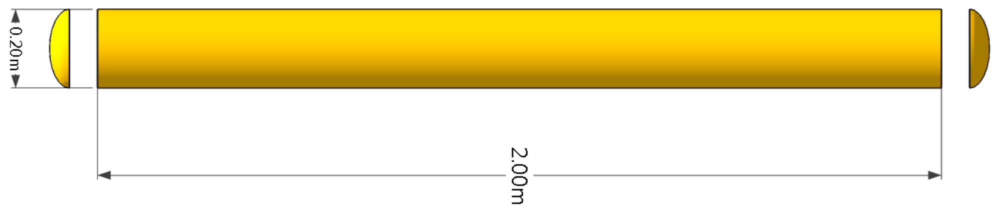

Figure 5.21 Design of inflatable beam

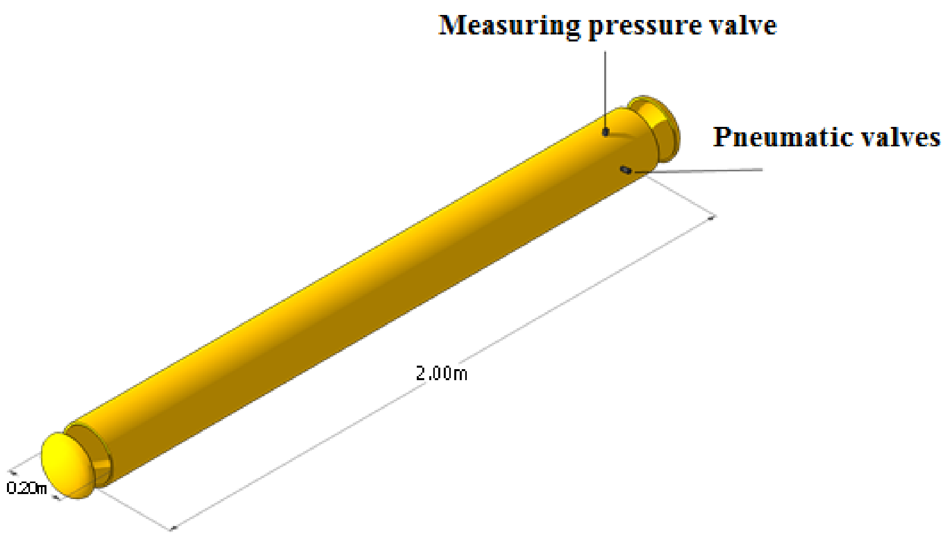

Figure 5.22 Valves of pumping and manometer

Figure 5.23 Inflatable beam after pumping

Figure 5.24 Inflatable beam's manometer

5.5 Buckling test set-up

In this study, three cylindrical inflatable beams are fabricated with the radius of R=100mm and the length of L=2m. A compressive load F is applied incrementally at one beam end: at first, one resets the load F to zero, and then gradually increases F. To visualize the lateral deflections of the beam during its axial compression loading, a tachometer with the precision order of 1 mm was used. The device was positioned about 4-5m of the testing beam.

This sequence is repeated until the first wrinkles appear which is called the critical point. At this point, the load F is the critical load of the beam. After passing the critical point, the beam rigidity has decreased, the axial displacement becomes very large and the compressive load cannot be increased.

The beam is subjected to an internal pressure p first under which the beam is in a prestressing state. An external load F is applied by a winch stacker at the end in the axial direction of the beam. A schematic view of the test set-up is shown in **Figure 5.15.**

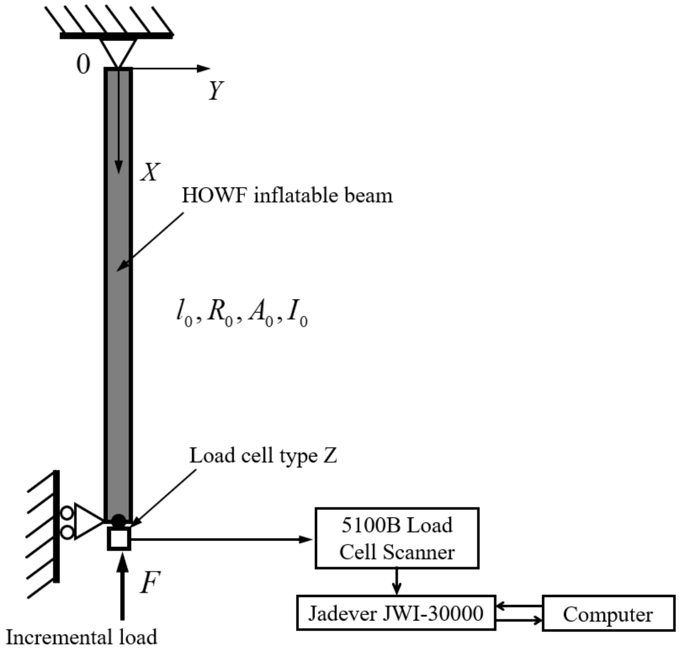

Figure 5.25 Schematic diagram of simply supported HOWF inflatable beam and instrumentation for buckling test

Due to the apparatus limitations, the boundary conditions applied to the structure are only simply supported. The beam is mounted in a vertical chassis with two supports at two ends. The support at bottom (the load applied end) is movable in axial direction. The experimental apparatus is shown in **Figure 5.26**.

The inflatable beams having the diameter of 200mm and the length of 2m is inflated with the air pressure of 1 kg/cm^2 (1kPa). The air pressure is monitored via a dial gauge attached to the valve built in the beam body.

One end of the beam is fixed to the test frame and the other end is only free to move in axial direction.

The test frame

The test frame as shown in **Figure 5.26** is made of standard alluminum uprights having a fixed top end and the bottom end can move following the alluminum guide. The whole frame is attached rigidly to the wall.

Figure 5.26 Frame system

Fixed-end and pin-end supports

Fixed-end support includes an alluminum plate fixed to the frame and a adjustable ring to fit the inflatable beam. The pin-end support at the bottom is also attached to an alluminum plate and has a ring to hold the bottom end. The bottom end is attached to the uprights with roller, allowing axis displatement of the bottom end. **Figure 5.27** illustrates detail of these supports.

Figure 5.27 The fixed-end and pin-end support

Instrumentation

- A load jack as shown in **Figure 5.28** is used to apply axial compressive load onto the beam and the load value is monitored by using a load-cell placed between the jack and the bottom alluminum plate, see **Figure 5.29**.

Figure 5.28 A load jack

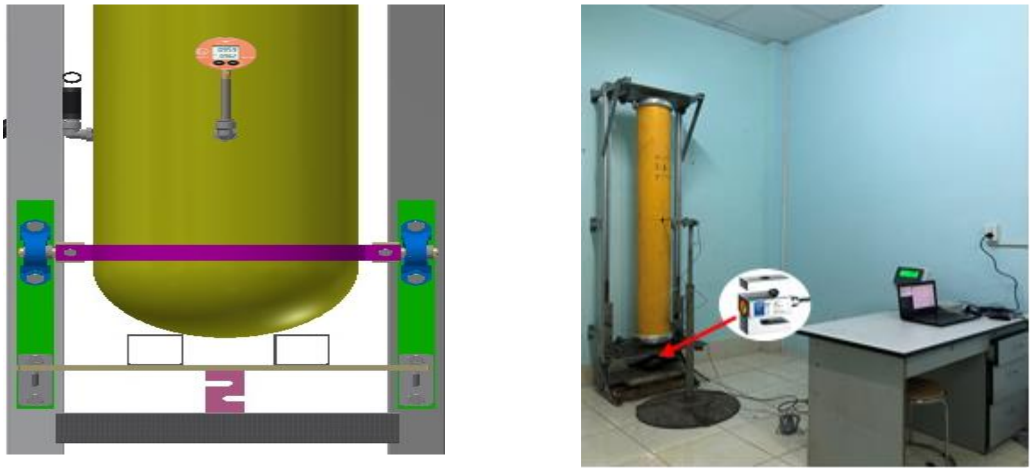

Figure 5.29 Mounting load cell type Z to the structure and restraints at top and bottom of an inflatable beam

Linear Variable Differential Transformer (LVDT) is used to measure the axial and transverse displacements of the beam under load. The LVDT is connected to a data acquisition computer to record the displacement variable as shown in **Figure 5.30**.

Figure 5.30 Linear Variable Differential Transformer

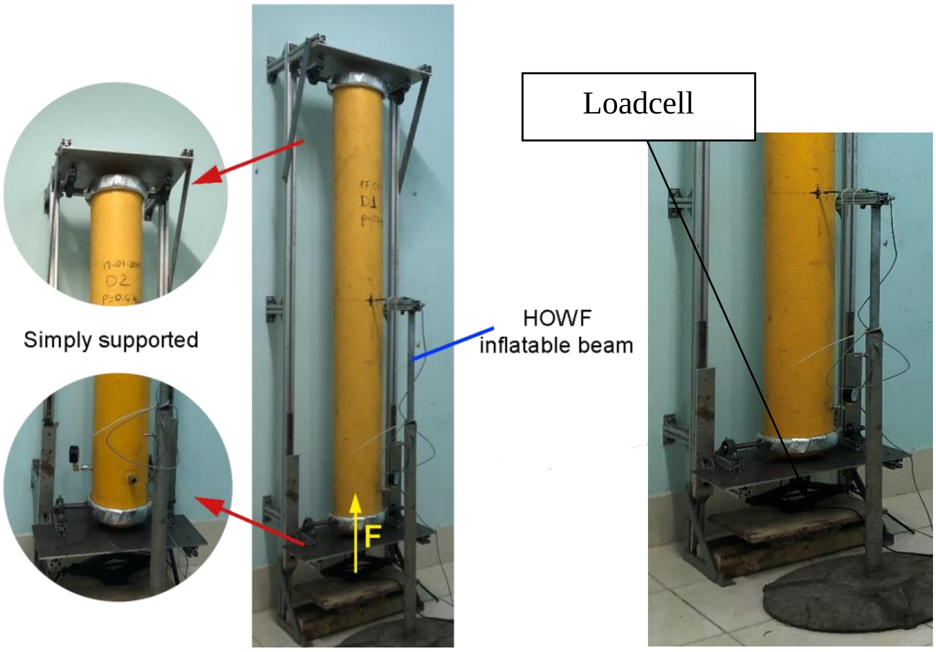

Figure 5.31 Experimental apparatus of HOWF simply supported inflatable beam for measuring the critical load

The pressure is measured twice per second and displayed by a precision digital manometer KK GAUGE **Figure 5.32**, which can measure up to 5 bar pressure with a precision of 0.01 bar. The pressures measured are in the range of 0.1- 0.3 bar.

(a) Pressure control valve (b) Pressure gauge

Figure 5.32 Digital Manometer KK GAUGE

After setting up the measuring equipments, the beam is inflated up to a certain pressure to maintain the shape of the beam, then position the beam into the test frame. The beam is then inflated to the designed pressure. As the diameter of the beam is enlarged when increasing air pressure, the top and bottom rings need to be adjusted to fit the beam, see **Figure 5.33.**

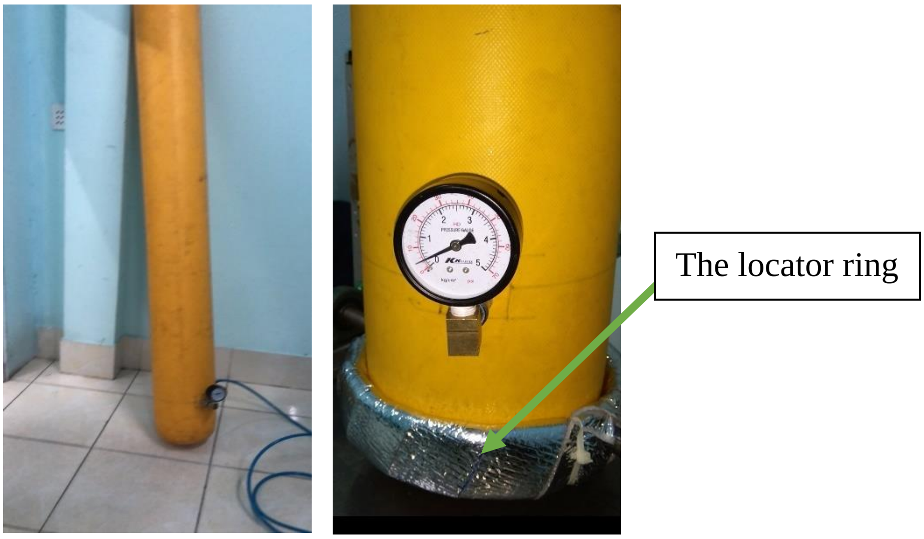

Figure 5.33 The locator ring can be adjusted in diameter

After inflating the beam, the axial compressive load is gradually applied at the bottom end. The load value is monitored via data acquisition to control the load rate. A beam specimen will be tested with four different values of air pressure, i.e. 20 kPa, 40 kPa, 60 kPa and 80 kPa. It can be seen in the **Figure 5.34** that the wrinkle appears at the same positon of the beam indepentable to the air pressure values. Therefore, it can be concluded that the wrinkle position is dependent to the beam's geometry and material properties rather than the air pressure.

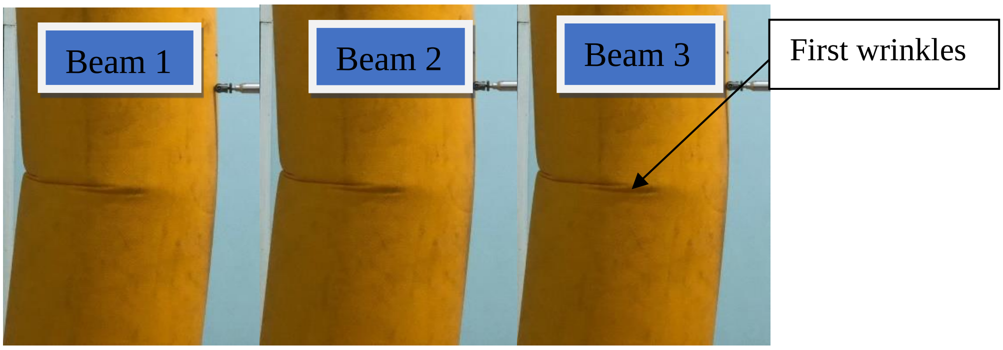

Figure 5.34 Position wrinkles begin to appear

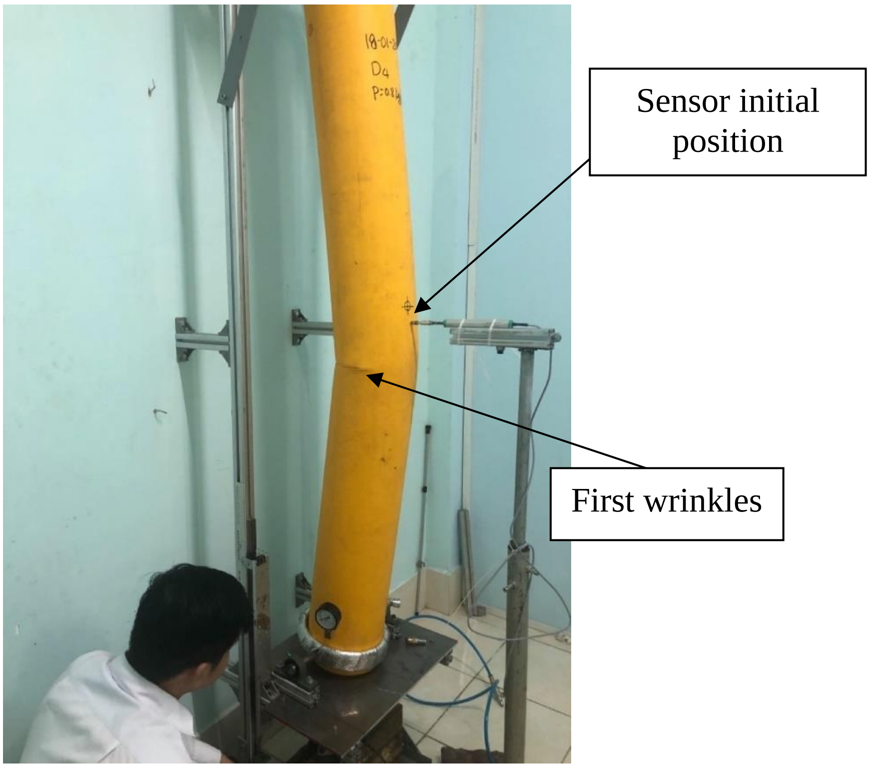

Figure 5.35 The first wrinkles appears

The first wrinkle indicates the instability configuration of the beam and the largest deflection occurs at the wrinkle position.

5.6 Experimental results and discussion

A typical test included the following steps:

1. Loading the beam until the first wrinkles of the skin appeared. Releasing the load.

2. Loading and unloading the beam above the first buckling load several times.

3. Loading the beam until collapse.

Strain gages, end-shortening and lateral readings as a function of the axial compression loading were recorded at each of above step, accompanied by video recording and photographs. It is also noted that the wrinkle magnitude is proportional to the beam rigidity. The beam must be relaxed in a reasonable time between the tests for the wrinkles disappear completely.

5.6.1 Load vs displacement u relation of beam at pressure

The experimental results determine the load-displacement relation of the inflatable beams with air pressures of 20 kPa, 40 kPa, 60 kPa and 80 kPa shown in **Table 5.12-Table 5.15 and Figure 5.36-Figure 5.39** respectively.

In **Table 5.12-Table 5.15**, it can be seen that the largest deviation is about 4.7% occuring as soon as the occurrence of the wrinkle. Such a small deviation indicates a good measurement method.

According to the **Figure 5.36-Figure 5.39**, it can be seen that the axial displacement increases linearly with the applied load, and the stiffness of the beam increases with the increase of the air pressure.

The first wrinkle appears when the axial displacement being about 70mm. The first wrinkle of the beam indicates the instablity of the beam, and soon enough the beam would buckle, leading to the significant decrease of load-carrying capacity of the inflatable beam.

The wrinkle occurs at a similar location in the beam, e.g. at the middle section. This can be explaned that the air pressure in the beam increases its load-carrying capacity, but the air pressure does not affect the buckling mode of the beam.

Each specimen is tested repeatedly four times for each air pressure magnitude. The critical load of the beam tends to be lower due to the fact that the the textile fibres have not fully recovered from the previous test. Therefore, it may be needed to investigate further into the composite material, as well as optimise the shape of the inflatable beam in order to obtain more accurate results.

a) p = 20 kPa

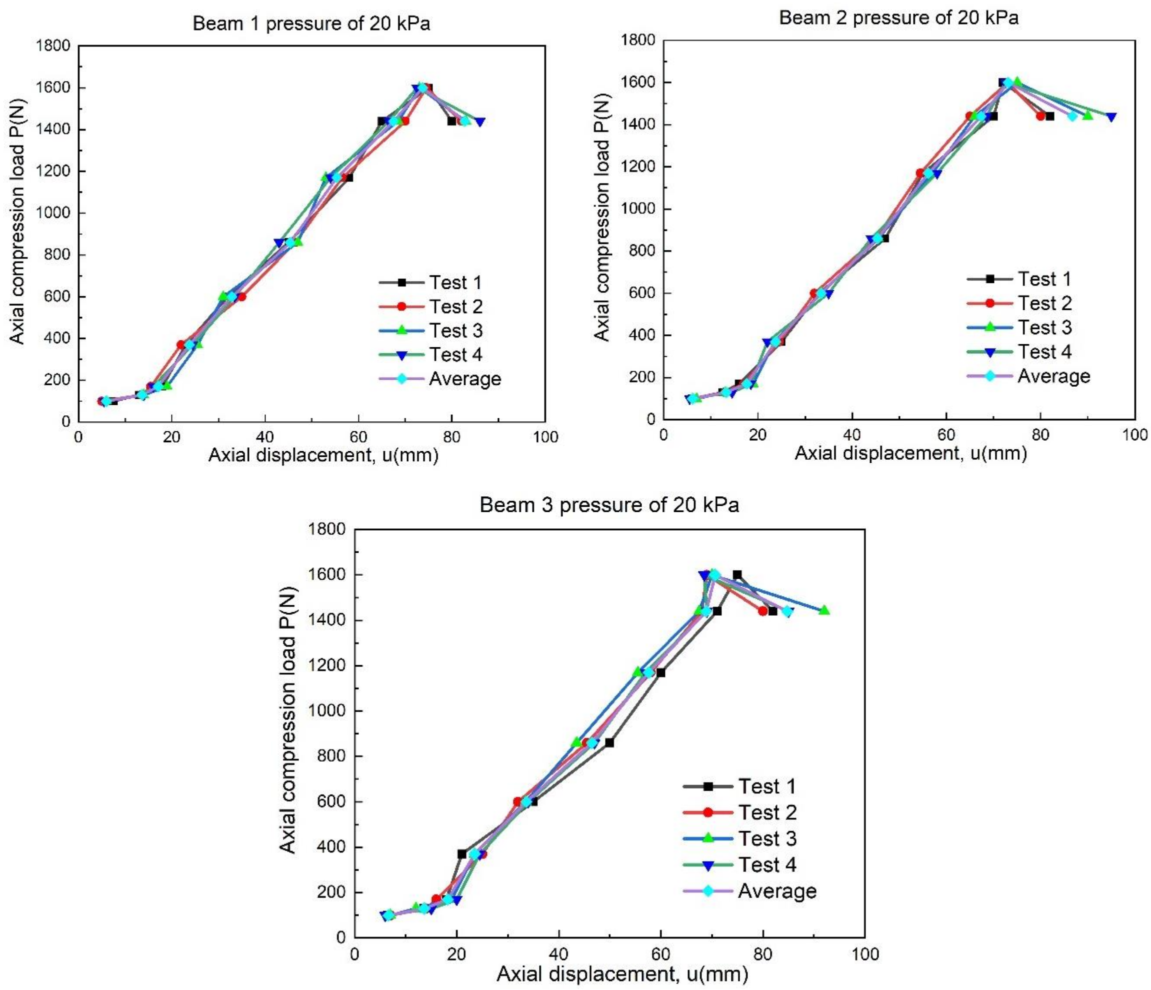

Figure 5.36 Load vs displacement relation of beam at pressure p = 20 kPa

Table 5.12 Load vs displacement relation of beam, p = 20 kPa

P(N)	**u (mm) Beam 1**				
	Test 1	**Test 2**	**Test 3**	**Test 4**	**Average**
100	7.5	5	6	5.5	6.0
130	13	13.5	14	14	13.6
170	18	15.5	19	16	17.1
370	23	22	25.5	24.5	23.8
600	32	35	31	33.5	32.9
860	45	46.5	47	43	45.4
1170	58	56.5	53	54	55.4
1440	65	70	68.5	66.5	67.5
1600	75	74.5	73	72.5	73.8

1440	80	82	83	86	82.8

P(N)	**u (mm) Beam 2**				
	Test 1	**Test 2**	**Test 3**	**Test 4**	**Average**
100	6	6	7	5.5	6.1
130	12.5	13	13	14.5	13.3
170	16	17	19	18.5	17.6
370	25	24.5	23.5	22	23.8
600	33	32	33.5	35	33.4
860	47	45	45.5	44	45.4
1170	55	54.5	57	58	56.1
1440	70	65	66	68.5	67.4
1600	72	73	75	72.5	73.1
1440	82	80	90	95	86.8

P(N)	**u (mm) Beam 3**				
	Test 1	**Test 2**	**Test 3**	**Test 4**	**Average**
100	6.5	7	7	6	6.6
130	13.5	14	12	15	13.6
170	18	16	19	20	18.3
370	21	25	23.5	24.5	23.5
600	35	32	33.5	34	33.6
860	50	45.5	43.5	47	46.5
1170	60	58	55.5	57	57.6
1440	71	68	67.5	69	68.9
1600	75	69	70	68.5	70.6
1440	82	80	92	85	84.8

b) p = 40 kPa

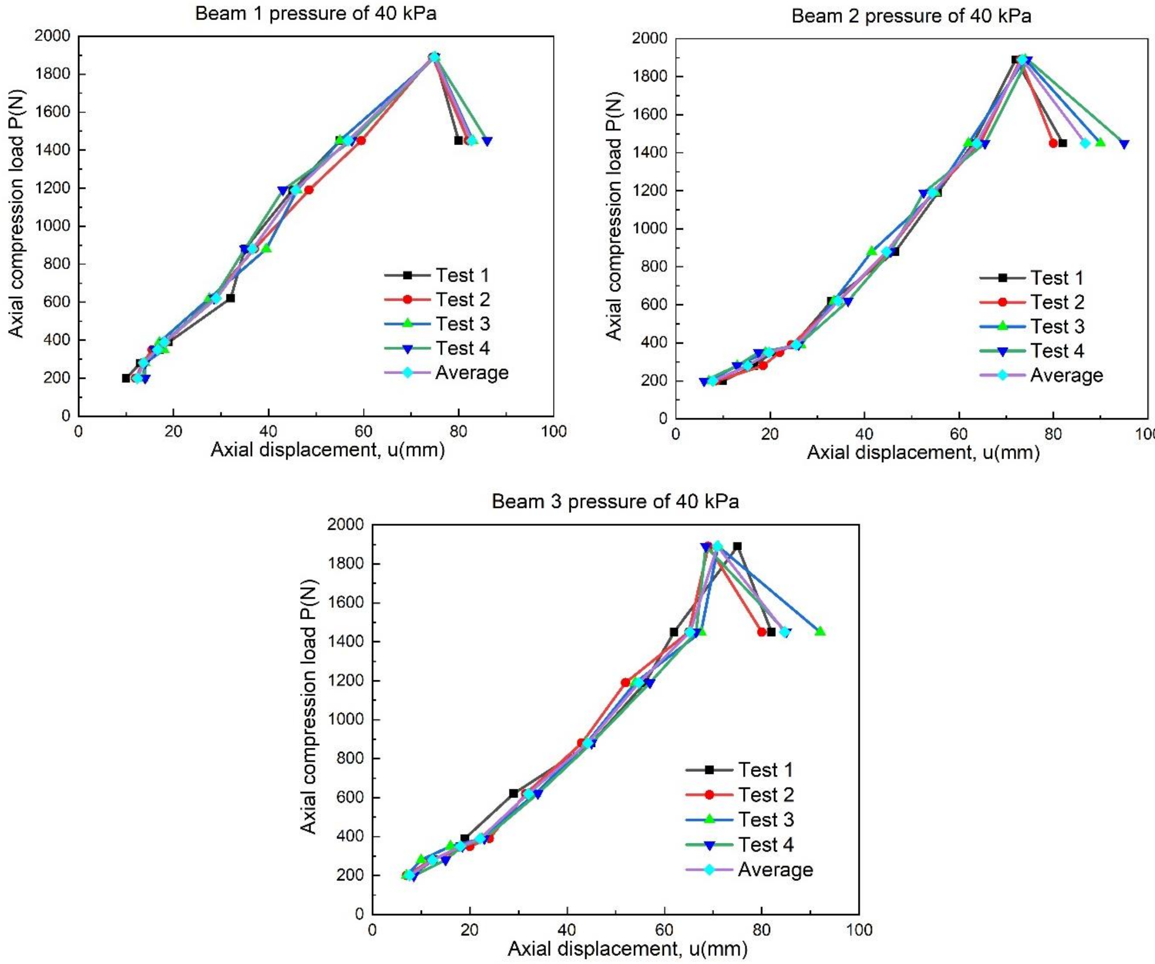

Figure 5.37 Load vs displacement relation of beam at pressure p= 40 kPa

Table 5.13 Load vs displacement relation of beam, p = 40 kPa

P(N)	u (mm) Beam 1				
	Test 1	**Test 2**	**Test 3**	**Test 4**	**Average**
200	10	12	13.5	14	12.4
280	13	13.5	14	14	13.6
350	17	15.5	18	16	16.6
390	19	18.5	17	18	18.1
620	32	28	27.5	28.5	29.0
880	35	37	39.5	35	36.6
1190	45	48.5	46	43	45.6
1450	55	59.5	55	57.5	56.8

1890	75	74.5	75	75	74.9
1450	80	82	83	86	82.8
P(N)	**u (mm) Beam 2**				
	Test 1	**Test 2**	**Test 3**	**Test 4**	**Average**
200	10	8.5	7	6	7.9
280	16.5	18.5	13	13	15.3
350	20.5	22	19	17.5	19.8
390	25	24.5	26.5	26	25.5
620	33	34.5	33.5	36.5	34.4
880	46.5	45	41.5	45.5	44.6
1190	55.5	54.5	55	52.5	54.4
1450	63	64.5	62	65.5	63.8
1890	72	73	74	74.5	73.4
1450	82	80	90	95	86.8
P(N)	**u (mm) Beam 3**				
	Test 1	**Test 2**	**Test 3**	**Test 4**	**Average**
200	8	7	7	8.5	7.6
280	12.5	12	10	15	12.4
350	18	20	16	18.5	18.1
390	19	24	22.5	23	22.1
620	29	31.5	33.5	34	32.0
880	45	43	44	45	44.3
1190	56	52	54	57	54.8
1450	62	65	67.5	66.5	65.3
1890	75	69	71	68.5	70.9
1450	82	80	92	85	84.8

c) p = 60 kPa

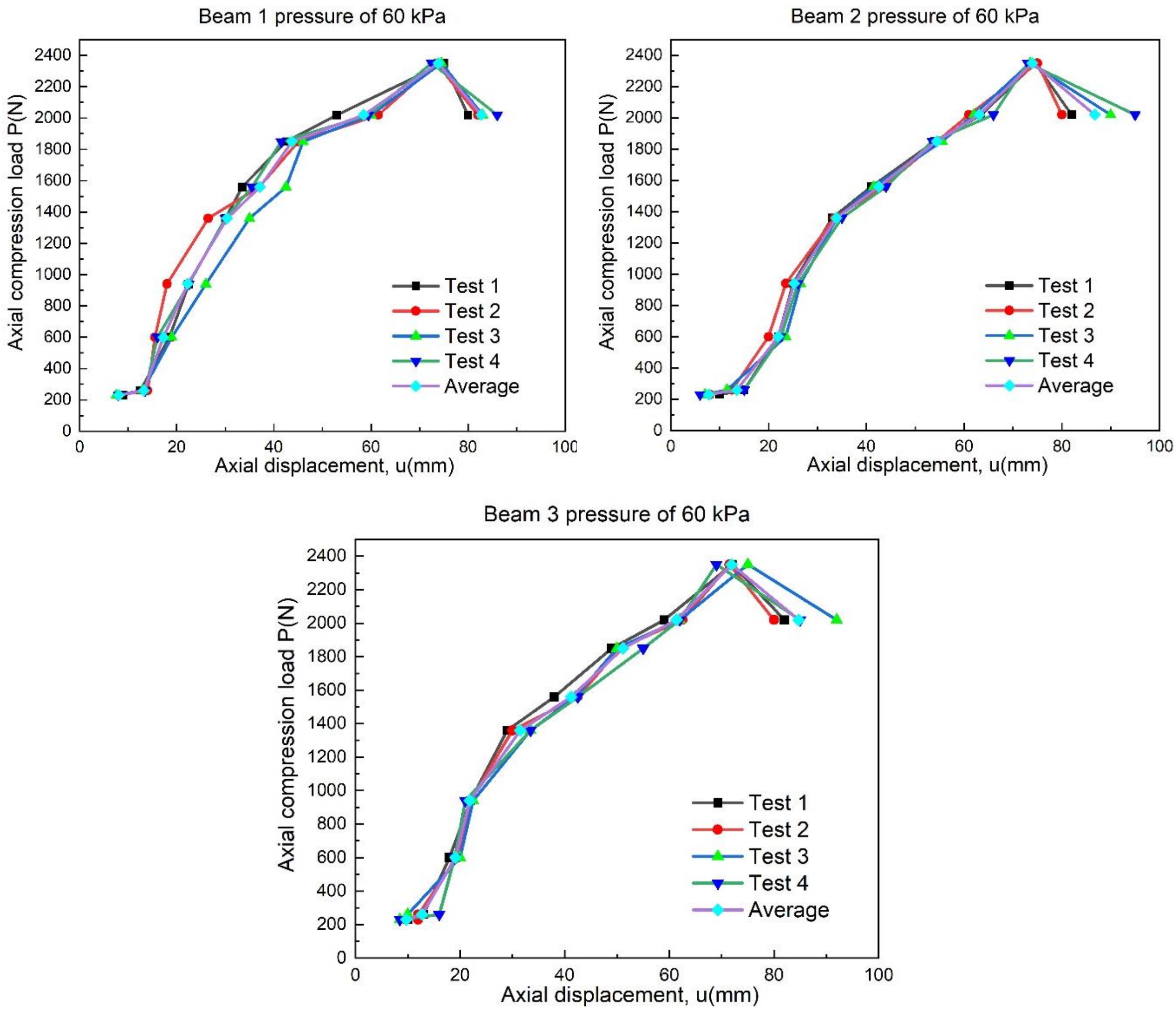

Figure 5.38 Load vs displacement relation of beam at pressure p = 60 kPa.

Table 5.14 Load vs displacement relation of beam, p = 60 kPa

P(N)	u (mm) Beam 1				
	Test 1	Test 2	Test 3	Test 4	Average
230	9	8	7.5	8	8.1
260	12.5	14	13	13.5	13.3
600	18.5	15.5	19	16	17.3
940	22.5	18	26	22.5	22.3
1360	30	26.5	35	30	30.4
1560	33.5	37	42.5	35.5	37.1
1850	42.5	45	46	41.5	43.8

2020	53	61.5	60	59.5	58.5
2350	75	73.5	74.5	72.5	73.9
2020	80	82	83	86	82.8
P(N)	**u (mm) Beam 2**				
	Test 1	**Test 2**	**Test 3**	**Test 4**	**Average**
230	10	8	7	6	7.8
260	15	12.5	11.5	15	13.5
600	22	20	23.5	22.5	22.0
940	25	23.5	26.5	26	25.3
1360	33	33.5	34	35	33.9
1560	41	43.5	41.5	44	42.5
1850	54	54.5	55.5	53.5	54.4
2020	63.5	61	62	66	63.1
2350	74.5	75	73.5	73	74.0
2020	82	80	90	95	86.8
P(N)	**u (mm) Beam 3**				
	Test 1	**Test 2**	**Test 3**	**Test 4**	**Average**
230	10	12	8.5	8.5	9.8
260	13	12	10	16	12.8
600	18	19.5	20	19	19.1
940	22	22	22.5	21	21.9
1360	29	30	33.5	33.5	31.5
1560	38	42.5	42	42.5	41.3
1850	49	50.5	50	55	51.1
2020	59	62.5	62	62	61.4
2350	72	71.5	75	69	71.9
2020	82	80	92	85	84.8

d) p = 80 kPa

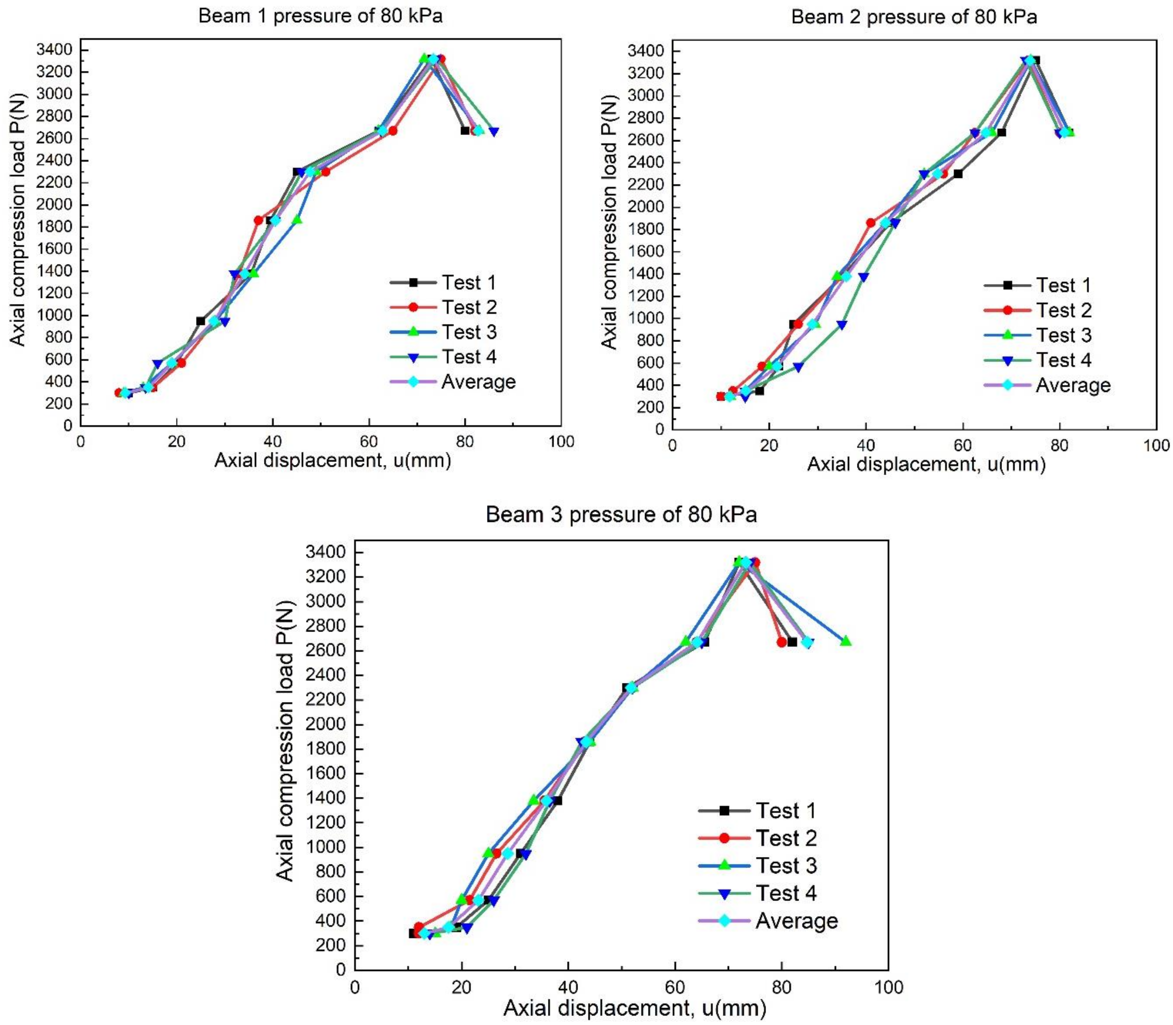

Figure 5.39 Load vs displacement relation of beam at pressure p= 80 kPa

Table 5.15 Load vs displacement relation of beam, p = 80 kPa

P(N)	u (mm) Beam 1				
	Test 1	**Test 2**	**Test 3**	**Test 4**	**Average**
300	10	8	9	10	9.3
350	15	15	13	13.5	14.1
570	20	21	19	16	19.0
950	25	28	28	30	27.8
1380	35.5	33	36	32	34.1
1860	39.5	37	45	40.5	40.5
2300	45	51	49	46	47.8

2670	62	65	62	62.5	62.9
3320	73	75	71.5	74	73.4
2670	80	82	83	86	82.8

P(N)	**u (mm) Beam 2**				
	Test 1	**Test 2**	**Test 3**	**Test 4**	**Average**
300	10	10	12	15	11.8
350	18	12.5	15	15	15.1
570	22	18.5	20	26	21.6
950	25	26	29.5	35	28.9
1380	35	35	34	39.5	35.9
1860	45	41	44	46	44.0
2300	59	56	52	52	54.8
2670	68	62.5	66	62.5	64.8
3320	75	73.5	74	73	73.9
2670	82	80	82	80	81.0

P(N)	**u (mm) Beam 3**				
	Test 1	**Test 2**	**Test 3**	**Test 4**	**Average**
300	11	12	15	14	13.0
350	19	12	18	21	17.5
570	25	21.5	20	26	23.1
950	31	26.5	25	32	28.6
1380	38	35.5	33.5	36.5	35.9
1860	44	43	44	42.5	43.4
2300	51	52	52	52	51.8
2670	65.5	64	62	65	64.1
3320	72	75	72	74	73.3
2670	82	80	92	85	84.8
300	11	12	15	14	13.0

5.6.1.1 Beams inflated with different air pressures

The following **Figure 5.40**, **Figure 5.41**, **Figure 5.42** and **Table 5.16**, **Table 5.17**, **Table 5.18** shows that carrying capacity of beams depends on pressure. The pressure increases, the loading capacity typically increases.

a) Beam 1

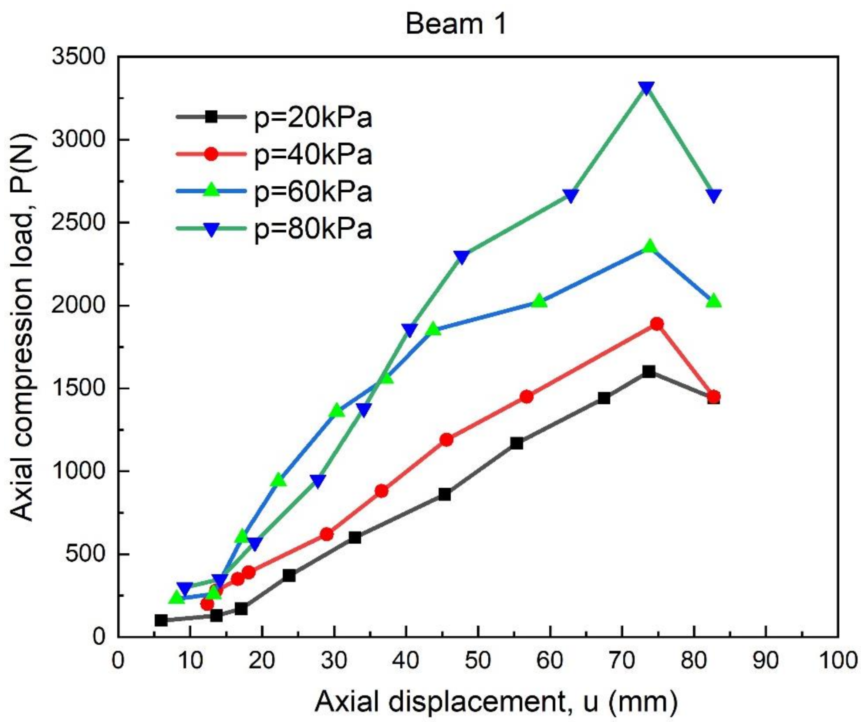

Figure 5.40 Load vs displacement relation of beam 1 at different pressures

Table 5.16 Load vs displacement relation of beam 1 at different pressures

p=20kPa		p=40kPa		p=60kPa		p=80kPa	
u(mm)	P(N)	u(mm)	P(N)	u(mm)	P(N)	u(mm)	P(N)
6	100	12	200	8	230	9	300
14	130	14	280	13	260	14	350
17	170	17	350	17	600	19	570
24	370	18	390	22	940	28	950
33	600	29	620	30	1360	34	1380
45	860	37	880	37	1560	41	1860
55	1170	46	1190	44	1850	48	2300
68	1440	57	1450	59	2020	63	2670

74	1600	75	1890	74	2350	73	3320
83	1440	83	1450	83	2020	83	2670

b) Beam 2

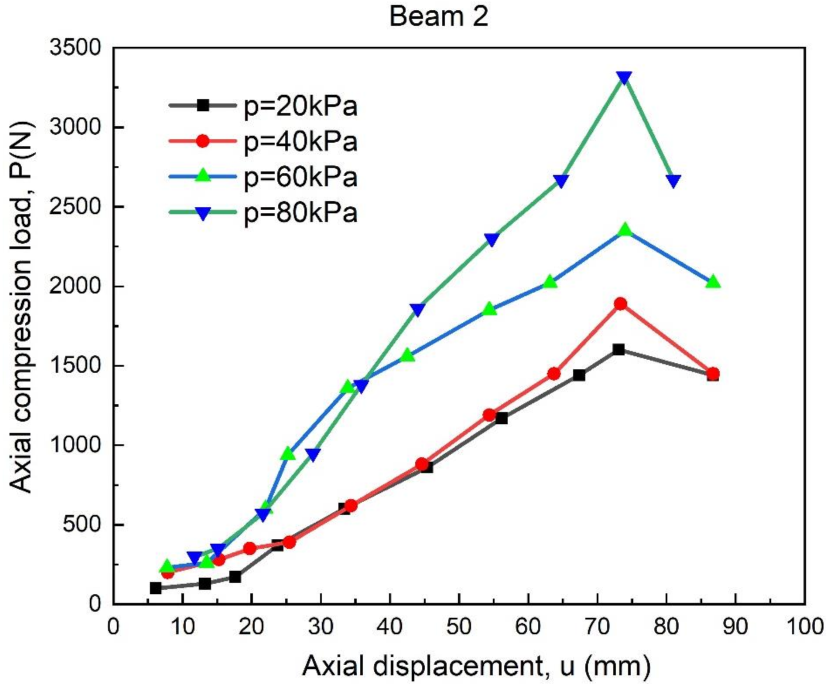

Figure 5.41 Load vs displacement relation of beam 2 at different pressures

Table 5.17 Load vs displacement relation of beam 2 at different pressures

p=20kPa		p=40kPa		p=60kPa		p=80kPa	
u(mm)	**P(N)**	**u(mm)**	**P(N)**	**u(mm)**	**P(N)**	**u(mm)**	**P(N)**
6	100	8	200	8	230	12	300
13	130	15	280	14	260	15	350
18	170	20	350	22	600	22	570
24	370	26	390	25	940	29	950
33	600	34	620	34	1360	36	1380
45	860	45	880	43	1560	44	1860
56	1170	54	1190	54	1850	55	2300
67	1440	64	1450	63	2020	65	2670
73	1600	73	1890	74	2350	74	3320

87	1440	87	1450	87	2020	81	2670

c) Beam 3

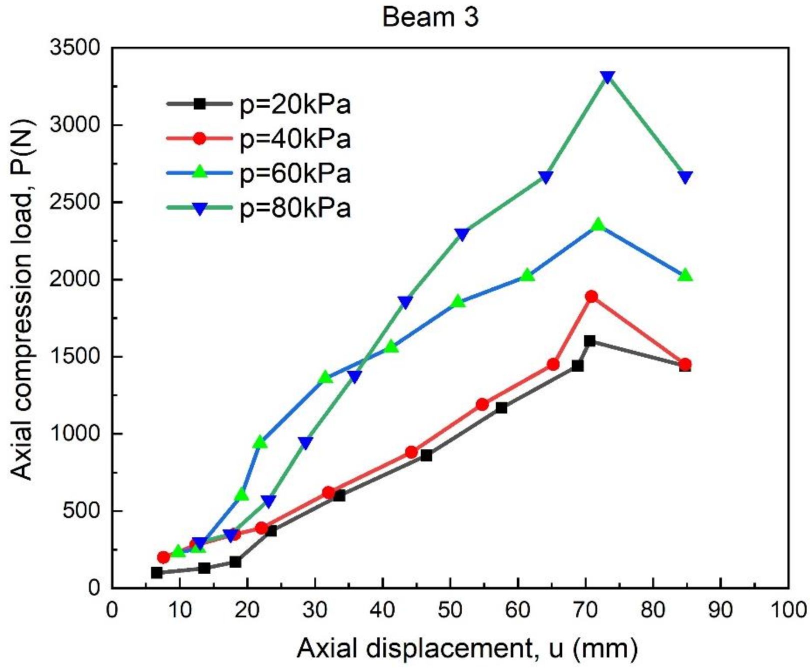

Figure 5.42 Load vs displacement relation of beam 3 at different pressures

Table 5.18 Load vs displacement relation of beam 3 at different pressures

p=20kPa		**p=40kPa**		**p=60kPa**		**p=80kPa**	
u(mm)	**P(N)**	**u(mm)**	**P(N)**	**u(mm)**	**P(N)**	**u(mm)**	**P(N)**
7	100	8	200	10	230	13	300
14	130	12	280	13	260	18	350
18	170	18	350	19	600	23	570
24	370	22	390	22	940	29	950
34	600	32	620	32	1360	36	1380
47	860	44	880	41	1560	43	1860
58	1170	55	1190	51	1850	52	2300
69	1440	65	1450	61	2020	64	2670
71	1600	71	1890	72	2350	73	3320
85	1440	85	1450	85	2020	85	2670

5.6.1.2 Comparison of 3 beams at pressure p = 80 kPa

According to the experimental results, when the axial load-carrying capacity of the beam get higher, the air-pressure maginitude particularly increases. When the air pressure reachs 80 kPa, the average load of three beams is able to withstand a maximum load of 2342 kN as shown in **Table 5.19**. The highest deviation of this critical load on the beams which compared to the average value is approximately 5.85%. This result indicates the uniformity of the specimen during the fabrication process. In summary, the beams with this result are fabricated by gluing with heat method… that give a similar result.

The **Figure 5.43** compares the buckling behaviour of the inflatable beams with different pressure applied, which demonstrates that the air pressure largely affects the stability of the inflatable beam. The experiment also shows that the maximum load-carrying capacity is proportion to the applied pressure.

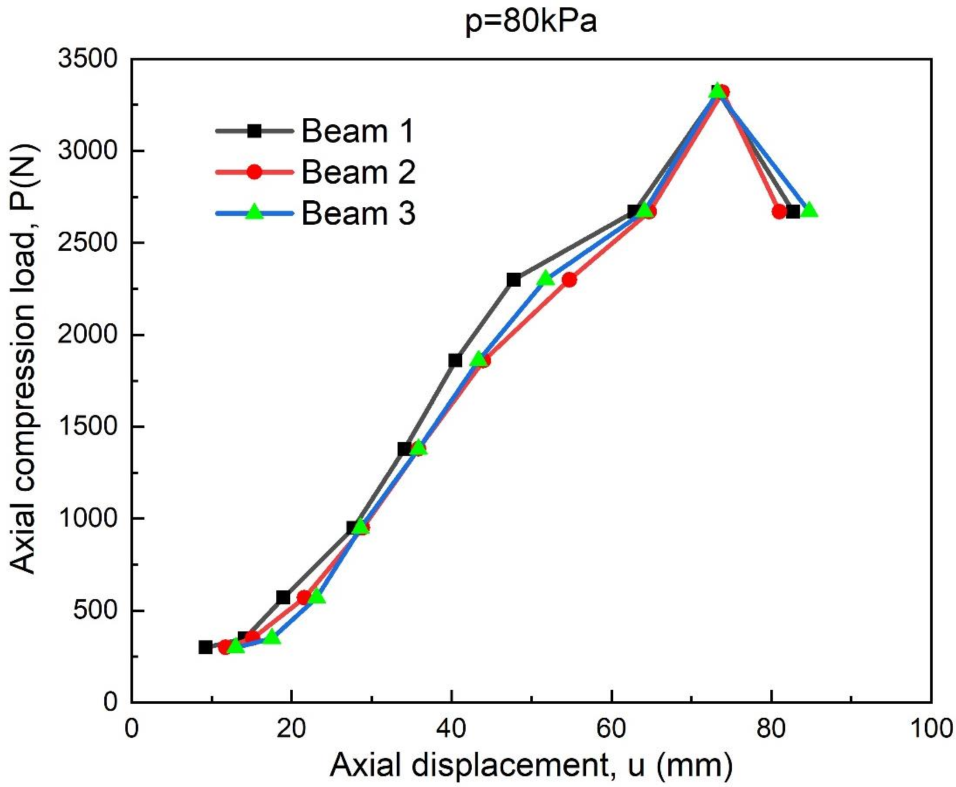

Figure 5.43 Comparison of 3 beams at pressure p = 80 kPa

Table 5.19 Comparison of 3 beams at pressure p = 80 kPa

Beam 1		Beam 2		Beam 3	
u(mm)	**P(N)**	**u(mm)**	**P(N)**	**u(mm)**	**P(N)**
9	300	12	300	13	300
14	350	15	350	18	350
19	570	22	570	23	570
28	950	29	950	29	950
34	1380	36	1380	36	1380
41	1860	44	1860	43	1860
48	2300	55	2300	52	2300
63	2670	65	2670	64	2670
73	3320	74	3320	73	3320
83	2670	81	2670	85	2670

5.6.2 Load vs displacement v relation of beam at pressure

To evaluate the influence of relationship between the load and displacement horizontal direction, each beam was examined respectively with pressure values of 20 kPa, 40 kPa, 60 kPa and 80 kPa. Each experiment was performed four times. Experimental results are presented in **Figure 5.44**, **Figure 5.45**, **Figure 5.46** and **Figure 5.47**. These results also show that when the pressure increases, the load capacity increase simultaneously and the displacing value before cracking also increases respectively.

a) p = 20 kPa

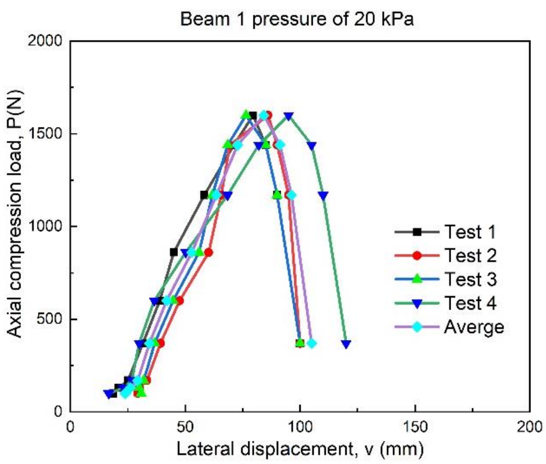

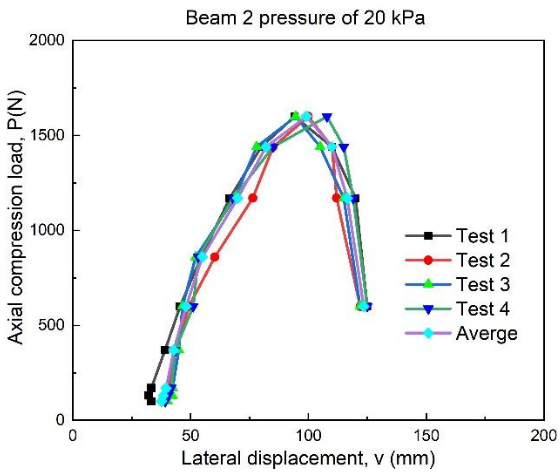

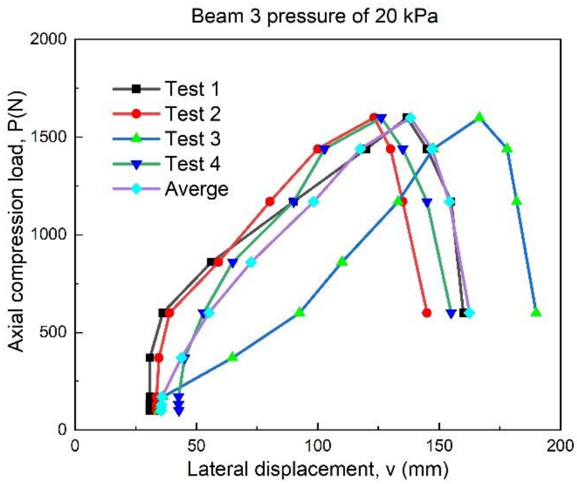

Figure 5.44 Load vs displacement relation of beam at pressure p = 20kPa

Table 5.20 Load vs displacement relation of beam, p = 20 kPa

P(N)	**v(mm) Beam 1**				
	Test 1	**Test 2**	**Test 3**	**Test 4**	**Average**
100	19	29	31	17	24
130	21	30	30	23	26
170	25	33	32	27	29
370	32	39	37	30	34
600	39	48	45	37	42
860	45	60	56	50	53
1170	58	66	62	68	64
1440	71	69	68	82	73
1600	80	86	76	95	84
1440	85	90	85	105	91
1170	90	95	90	110	96
370	100	100	100	120	105
P(N)	**v(mm) Beam 2**				
	Test 1	**Test 2**	**Test 1**	**Test 4**	**Average**
100	33	38	40	39	38
130	32	39	42	40	38
170	33	41	42	42	40

370	39	44	45	43	43
600	46	49	47	51	48
860	54	60	52	53	55
1170	67	76	69	68	70
1440	80	85	78	85	82
1600	94	100	95	108	99
1440	110	110	105	115	110
1170	120	112	115	119	117
600	125	122	122	125	124

P(N)	**v(mm) Beam 3**				
	Test 1	**Test 2**	**Test 1**	**Test 4**	**Average**
100	31	34	35	43	35
130	31	34	35	43	36
170	31	34	36	43	36
370	31	35	65	45	44
600	36	39	92	53	55
860	56	59	110	65	73
1170	90	80	133	90	98
1440	120	100	148	103	118
1600	137	123	167	126	138
1440	145	130	178	135	147
1170	155	135	182	145	154
600	160	145	190	155	163

b) p = 40 kPa

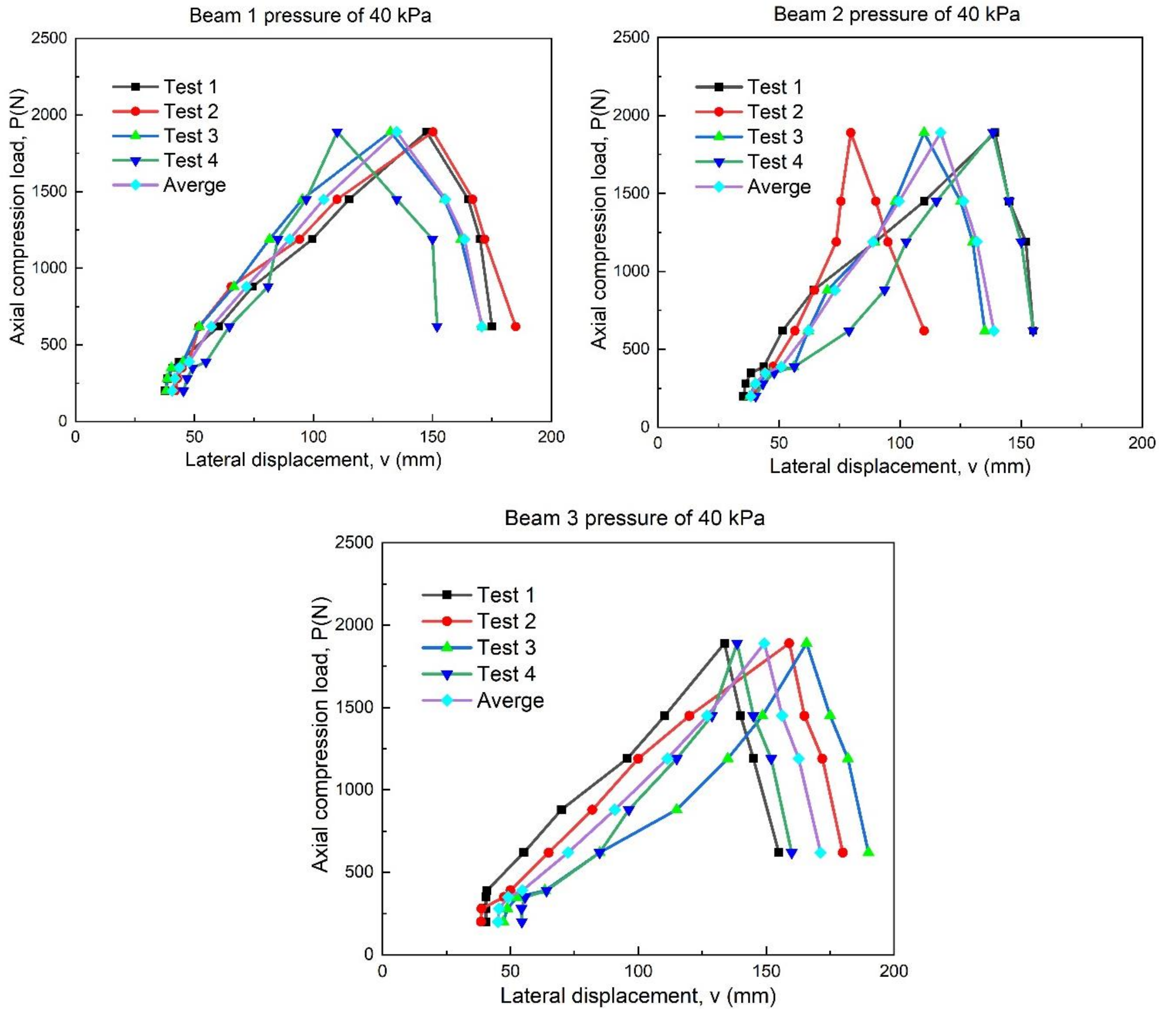

Figure 5.45 Load vs displacement relation of beam at pressure p =40 kPa

Table 5.21 Load vs displacement relation of beam, p = 40 kPa

P(N)	v(mm) Beam 1				
	Test 1	Test 2	Test 3	Test 4	Average
200	38	42	38	45	41
280	39	43	39	47	42
350	41	45	40	49	44
390	44	48	45	55	48
620	60	52	52	65	57
880	74	65	67	81	72
1190	100	94	82	85	90

1450	115	110	95	97	104
1890	147	150	132	110	135
1450	165	167	155	135	156
1190	170	172	162	150	164
620	175	185	171	152	171

P(N)	**v(mm) Beam 2**				
	Test 1	**Test 2**	**Test 1**	**Test 4**	**Average**
200	35	40	38	40	38
280	36	41	40	43	40
350	38	44	47	48	44
390	44	48	56	56	51
620	51	57	62	79	62
880	64	65	70	94	73
1190	90	74	89	103	89
1450	110	76	98	115	100
1890	139	80	110	138	117
1450	145	90	125	145	126
1190	152	95	130	150	132
620	155	110	135	155	139

P(N)	**v(mm) Beam 3**				
	Test 1	**Test 2**	**Test 1**	**Test 4**	**Average**
200	40	39	47	54	45
280	40	39	49	54	46
350	40	48	53	56	49
390	41	50	63	64	55
620	55	65	85	85	73
880	70	82	115	96	91
1190	96	100	135	115	111
1450	110	120	149	129	127

1890	134	159	166	139	149
1450	140	165	175	145	156
1190	145	172	182	152	163
620	155	180	190	160	171

c) p = 60 kPa

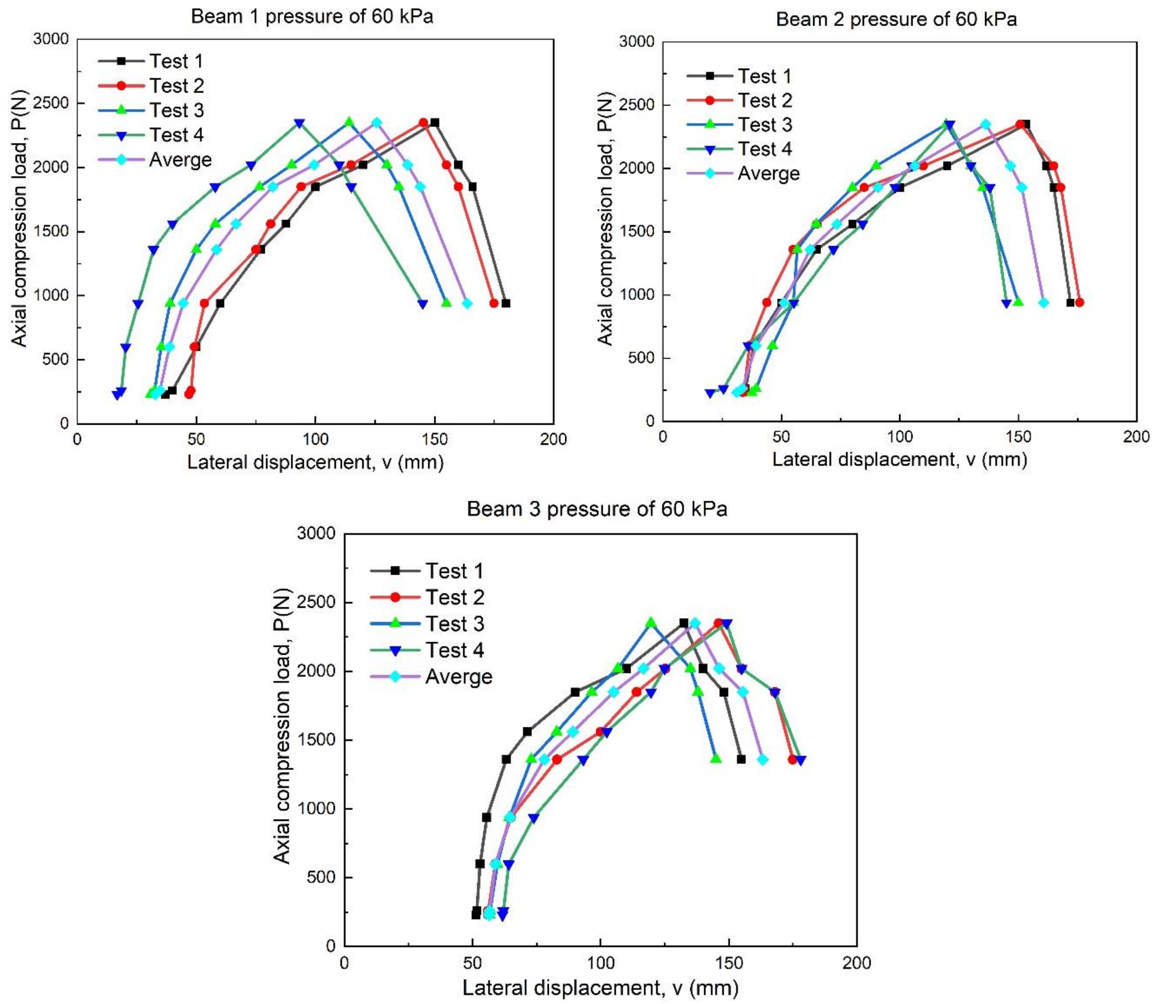

Figure 5.46 Load vs displacement relation of beam at pressure p = 0 kPa

Table 5.22 Load vs displacement relation of beam, p = 60 kPa

P(N)	v(mm) Beam 1				
	Test 1	**Test 2**	**Test 3**	**Test 4**	**Average**
230	37	47	31	17	33
260	40	48	32	18	35

600	50	49	35	20	39
940	60	53	39	26	44
1360	77	75	50	32	59
1560	88	81	58	40	67
1850	100	94	77	58	82
2020	120	115	90	73	100
2350	150	145	114	93	126
2020	160	155	130	110	139
1850	166	160	135	115	144
940	180	175	155	145	164
P(N)	**v(mm) Beam 2**				
	Test 1	**Test 2**	**Test 1**	**Test 4**	**Average**
230	34	34	38	20	31
260	35	34	39	26	34
600	38	37	46	36	39
940	50	44	55	55	51
1360	65	55	57	72	62
1560	80	65	65	84	74
1850	100	85	80	98	91
2020	120	110	90	105	106
2350	153	151	120	121	136
2020	162	165	130	130	147
1850	165	168	135	138	152
940	172	176	150	145	161
P(N)	**v(mm) Beam 3**				
	Test 1	**Test 2**	**Test 1**	**Test 4**	**Average**
230	51	56	57	62	56
260	52	56	57	62	57
600	53	59	60	64	59

940	56	65	64	74	65
1360	63	83	73	93	78
1560	71	100	83	102	89
1850	90	114	97	120	105
2020	110	125	107	125	117
2350	132	146	120	149	137
2020	140	155	135	155	146
1850	148	168	138	168	156
1360	155	175	145	178	163

d) p = 80 kPa

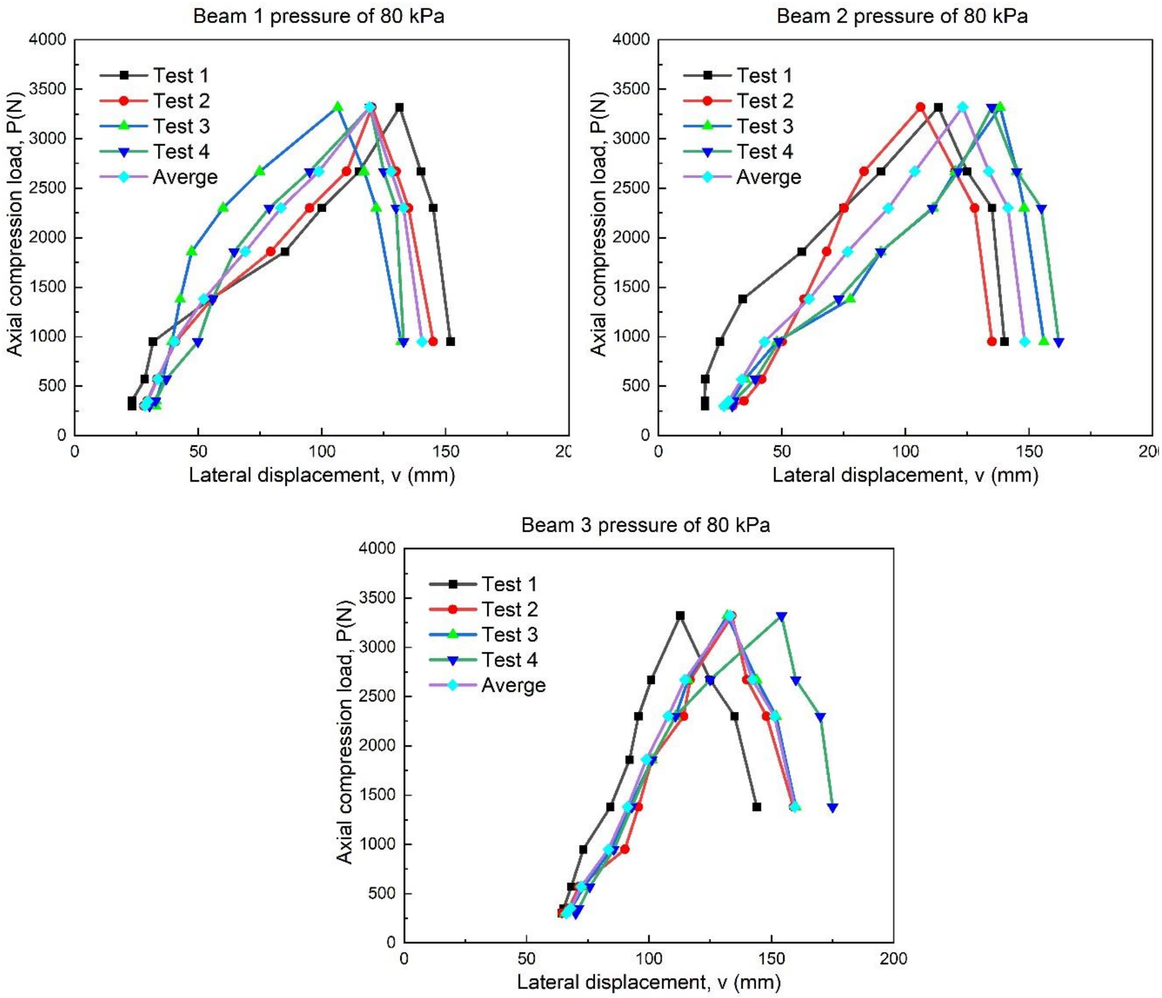

Figure 5.47 Load vs displacement relation of beam at pressure p = 80 kPa

Table 5.23 Load vs displacement relation of beam, p = 80 kPa

P(N)	**v(mm) Beam 1**				
	Test 1	**Test 2**	**Test 3**	**Test 4**	**Average**
300	23	28	33	30	28
350	23	29	33	33	30
570	28	33	35	37	33
950	32	41	39	50	40
1380	55	55	43	56	52
1860	85	79	47	64	69
2300	100	95	60	79	83
2670	115	110	75	95	99
3320	131	120	106	120	119
2670	140	130	117	125	128
2300	145	135	122	130	133
950	152	145	132	133	141
P(N)	**v(mm) Beam 2**				
	Test 1	**Test 2**	**Test 1**	**Test 4**	**Average**
300	19	30	27	30	26
350	19	35	30	31	28
570	19	42	35	39	34
950	25	50	48	49	43
1380	34	59	78	73	61
1860	58	68	90	90	77
2300	75	75	111	111	93
2670	90	83	120	121	104
3320	113	106	138	135	123
2670	125	120	145	145	134
2300	135	128	148	155	142

P(N)	v(mm) Beam 3				
	Test 1	**Test 2**	**Test 1**	**Test 4**	**Average**
950	140	135	156	162	148
300	65	65	66	70	66
350	65	67	68	71	68
570	68	71	73	76	72
950	73	90	85	86	83
1380	84	96	92	93	91
1860	92	101	101	101	99
2300	96	114	111	111	108
2670	101	117	116	125	115
3320	113	134	132	154	133
2670	125	140	144	160	142
2300	135	148	152	170	151
1380	144	159	160	175	160

5.6.2.1 Beams inflated with different air pressures

a) Beam 1

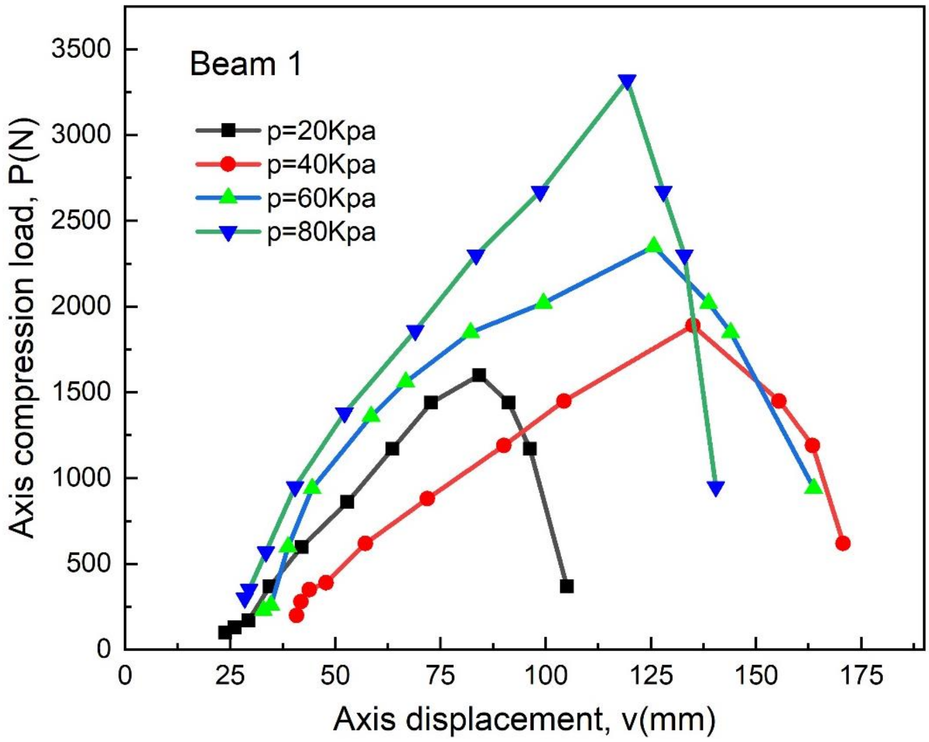

Figure 5.48 Load vs displacement relation of beam 1 at different pressures

Table 5.24 Load vs displacement relation of beam 1 at different pressures

P=20kPa		P=40kPa		P=60kPa		P=80kPa	
v(mm)	P(N)	v(mm)	P(N)	v(mm)	P(N)	v(mm)	P(N)
24	100	41	200	33	230	28	300
26	130	42	280	35	260	30	350
29	170	44	350	39	600	33	570
34	370	48	390	44	940	40	950
42	600	57	620	59	1360	52	1380
53	860	72	880	67	1560	69	1860
64	1170	90	1190	82	1850	83	2300
73	1440	104	1450	100	2020	99	2670
84	1600	135	1890	126	2350	119	3320
91	1440	156	1450	139	2020	128	2670
96	1170	164	1190	144	1850	133	2300
105	370	171	620	164	940	141	950

b) Beam 2

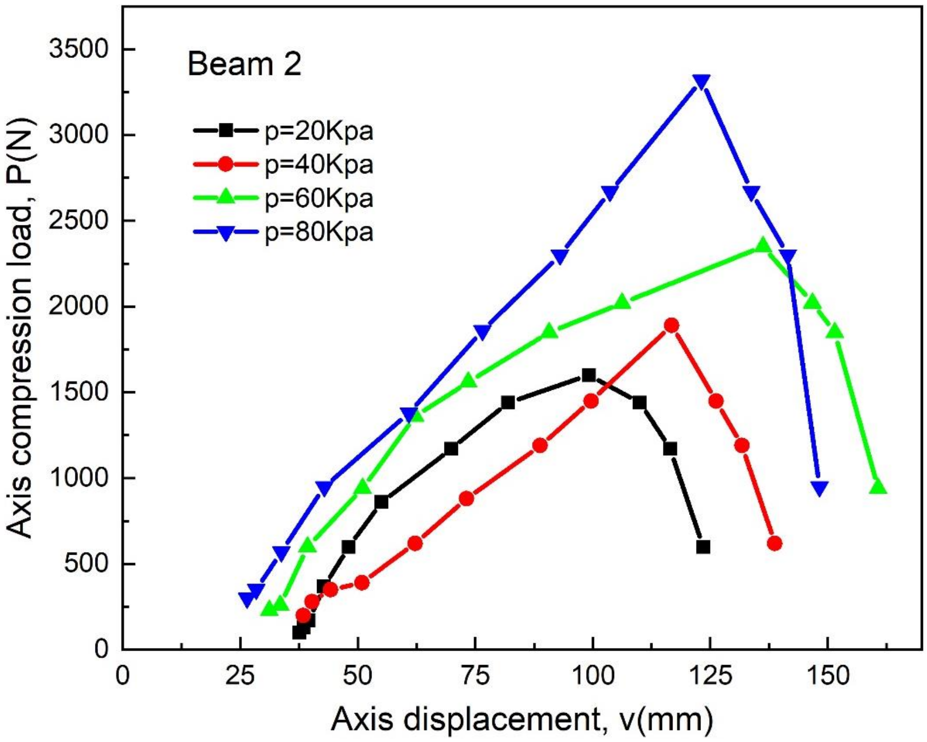

Figure 5.49 Load vs displacement relation of beam 2 at different pressures

Table 5.25 Load vs displacement relation of beam 2 at different pressures

P=20kPa		P=40kPa		P=60kPa		P=80kPa	
v(mm)	P(N)	v(mm)	P(N)	v(mm)	P(N)	v(mm)	P(N)
38	100	38	200	31	230	26	300
38	130	40	280	34	260	28	350
40	170	44	350	39	600	34	570
43	370	51	390	51	940	43	950
48	600	62	620	62	1360	61	1380
55	860	73	880	74	1560	77	1860
70	1170	89	1190	91	1850	93	2300
82	1440	100	1450	106	2020	104	2670
99	1600	117	1890	136	2350	123	3320
110	1440	126	1450	147	2020	134	2670
117	1170	132	1190	152	1850	142	2300
124	600	139	620	161	940	148	950

c) Beam 3

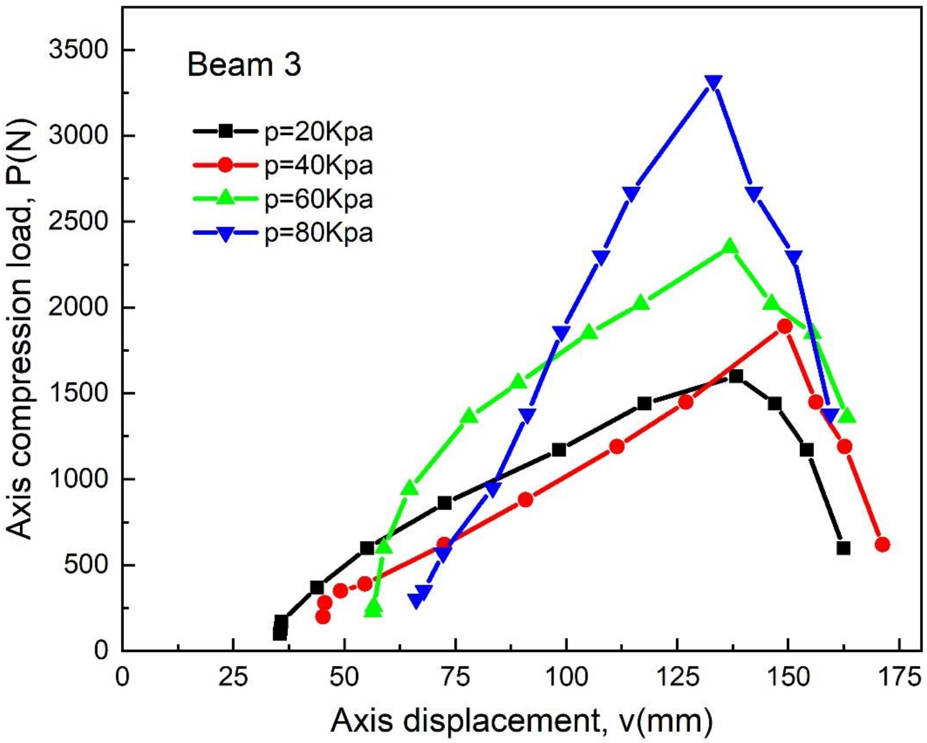

Figure 5.50 Load vs displacement relation of beam 3 at different pressures

Table 5.26 Load vs displacement relation of beam 3 at different pressures

P=20kPa		P=40kPa		P=60kPa		P=80kPa	
v(mm)	P(N)	v(mm)	P(N)	v(mm)	P(N)	v(mm)	P(N)
35	100	45	200	56	230	66	300
36	130	46	280	57	260	68	350
36	170	49	350	59	600	72	570
44	370	55	390	65	940	83	950
55	600	73	620	78	1360	91	1380
73	860	91	880	89	1560	99	1860
98	1170	111	1190	105	1850	108	2300
118	1440	127	1450	117	2020	115	2670
138	1600	149	1890	137	2350	133	3320
147	1440	156	1450	146	2020	142	2670
154	1170	163	1190	156	1850	151	2300
163	600	171	620	163	1360	160	1380

5.6.2.2 Comparison of 3 beams at pressure p = 80 kPa

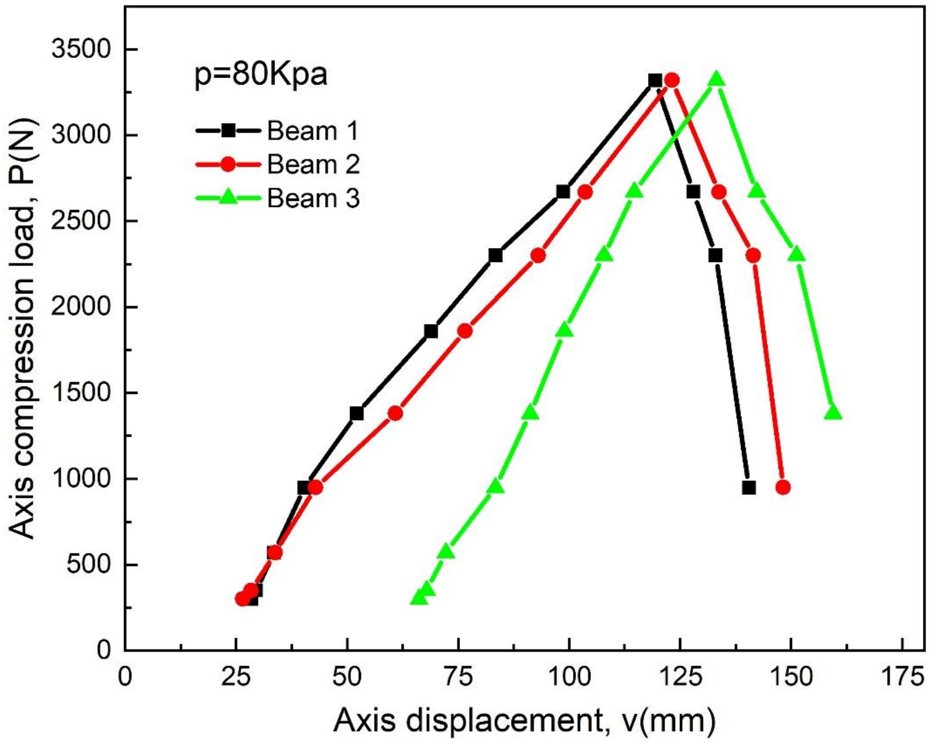

Figure 5.51 Comparison of 3 beams at pressure p = 80 kPa

Table 5.27 Comparison of 3 beams at pressure p = 80 kPa

Beam 1		**Beam 2**		**Beam 3**	
v(mm)	**P(N)**	**v(mm)**	**P(N)**	**v(mm)**	**P(N)**
28	300	26	300	66	300
30	350	28	350	68	350
33	570	34	570	72	570
40	950	43	950	83	950
52	1380	61	1380	91	1380
69	1860	77	1860	99	1860
83	2300	93	2300	108	2300
99	2670	104	2670	115	2670
119	3320	123	3320	133	3320
128	2670	134	2670	142	2670
133	2300	142	2300	151	2300
141	950	148	950	160	1380

5.7 Comparison between experimental and IGA numerical methods

Figure 5.52 and **Figure 5.53** compare the experimental results and numerical results obtained from IGA. In general, it is seen that the results obtained from experiments and those from IGA are somewhat similar in the structural response of inflating beams.

For the beams with low pressure, it can be seen that the experimental results and modelling results are not in good agreement. However, if the pressure in the beam increases, the prediction of IGA model becomes close to the experimental results. This phenomenon can be explained as follows:

- In the experimental process, while we inflate and conduct experiments at low pressures, the beam is not tension enough so that it can keep the beam firm at this time. We can just put the sensors in at this time and it creates settlement on the beam body. At the same time, the sensor has not received the result of compressive force during the compression process.

- The formation according to “u” changes that make the beam radius increases. The result was that we can see initial stages of experiments, the sensors often earlier receive the results on the diagrams. However, when increasing the pump pressure in the beam, we observe that the numerical and experimental results are converged.

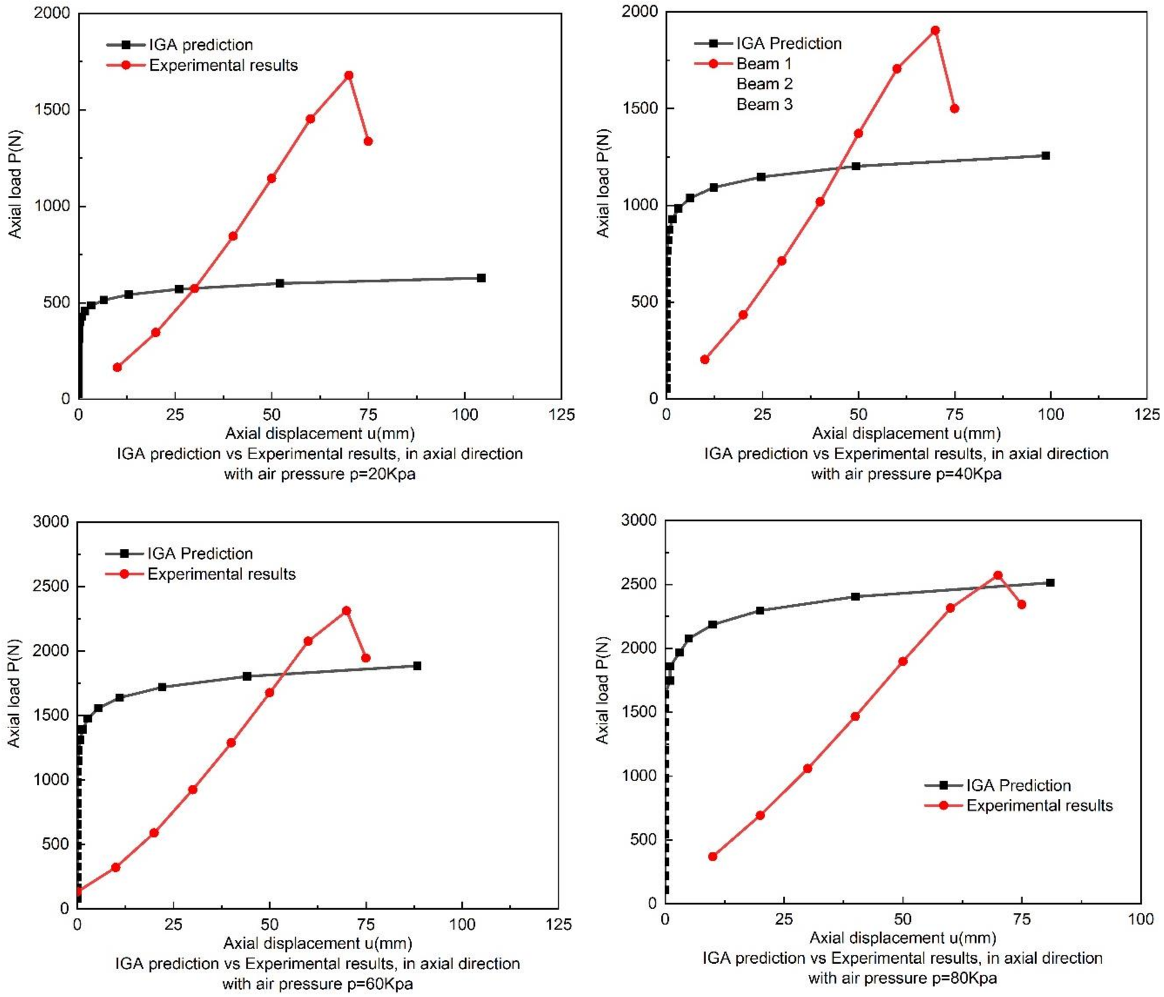

Figure 5.52 IGA prediction vs Experimental results, in axial displacement u with air pressure 20 kPa, 40 kPa, 60 kPa and 80 kPa

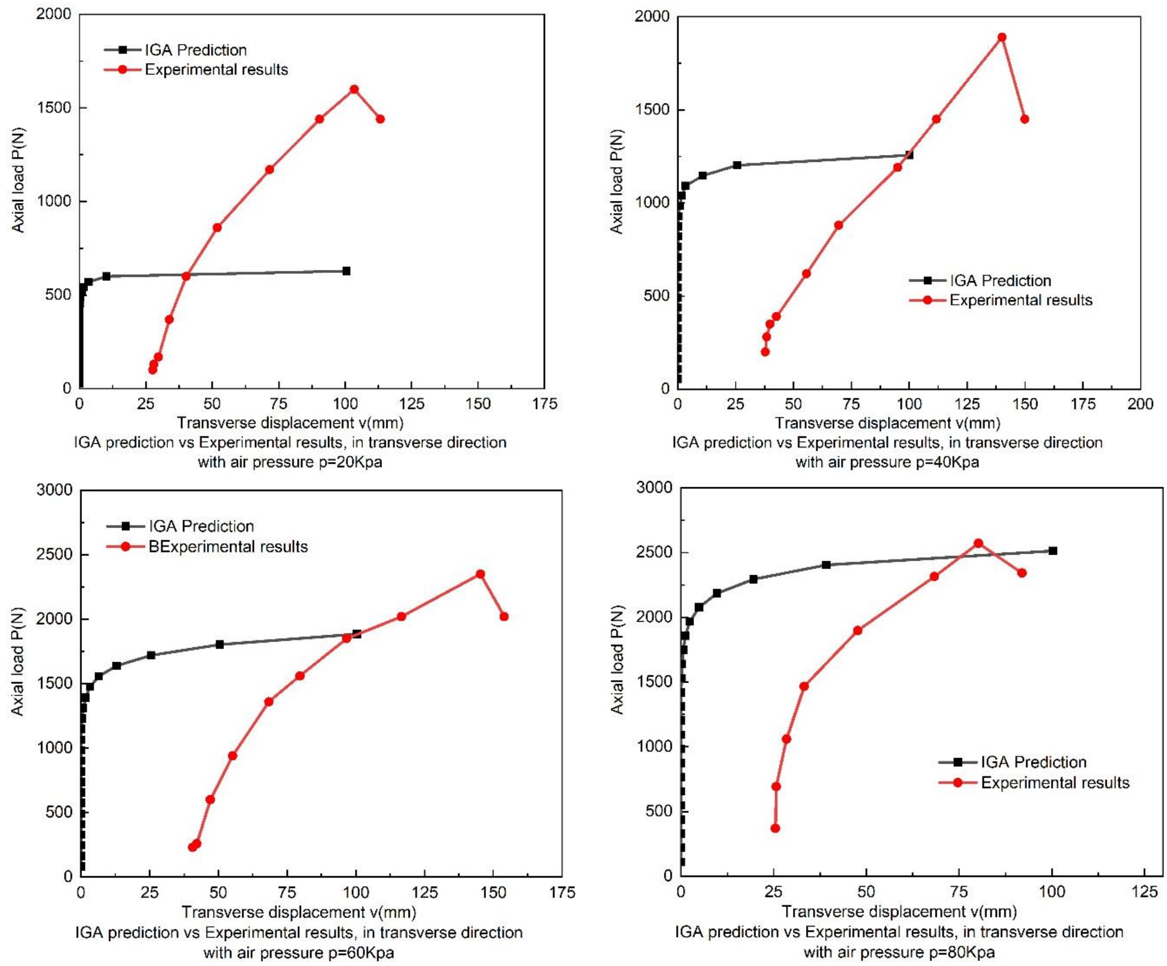

Figure 5.53 IGA prediction vs Experimental results, in transverse displacement v with air pressure 20 kPa, 40 kPa, 60 kPa and 80 kPa

The discepancy between experimental and numerical results for low-pressure beam might be explained due to several aspects, which are summarized as follows:

- The shortage in the real material information and errors in experiemental procedures might caused significant errors in the experimental results.

- The numerical silmulation dose not account for the failure of material, which might be the main failure reason in case of low pressure inflating beams.

- Material models used in the numerical approach might not appropriate for the use of composite fabric material, this need further comprehensive investigations.

5.8 Conclusion

In this chapter, an experimental program was conducted in details to investigate the buckling response of HOWF inflating beams. First of all, some tests are conducted to find out the properties of material. Then the buckling tests are successfully conducted with different air pressure. The results of axial load-deflection are recorded and then compared with numerical predictions based on Isogeometric Analysis.

The experiment results show that the strength of inflating beams increase with the raise of air pressure. This is consistent with those obtained from numerical prediction in the previous chapter. In addition, it is found out that the numerical models only show acceptable prediction for the inflating beams with high pressure.

CHAPTER 6: CONCLUSIONS AND FURTHER STUDIES

6.1 Conclusions

In this study, a numerical modelling technique and an experimental program are conducted to investigate the stability behaviour of inflating beam made from composite materials.

The numerical modeling is conducted based on Isogeometric Analysis approach, in which the beam models are developed based on Timoshenko's beam theory. The governing equations are derived based on total Lagrange approach, in which the membrane and bending actions are considered simultaneously. The NURBS basis funtions of IGA approach are ultilized to descrized the governing equations and develope the global equations. Both linear and nonlinear buckling analyses are carried out. In the nonlinear buckling analysis, the well-known Newton-Raphson technique is adopted to trace the buckling curves. Validiation and various parametric studies are conducted to show the reliability of the approach and study the influence of internal pressure in the beams.

In the experimental study, the material propeties of pabric composite material are firstly investigated. Then, the buckling tests are caried out to study the behaviour of inflating beams with different air pressure. Experimental resutls are also comprared with those obtained from the numerical modeling approach.

Some major conclusions drawn from this study cound be summaried as follows:

- A numerical approach based on IGA was successfully developed to investigate the stability of inflating beams.

- The results obtained from IGA approach are in good agreement with those from traditional FEM. In addition, it was found out that IGA-based approach has a better convergence rate than FEM.

- From the numerical modeling and experimental results, it is seen that the stability strength of inflating beams increases with the level of the internal pressure.

- The prediction of the proposed IGA-based numerical model is more reliable in cases that pressure is high, for cases with low pressure, the prediction show a similar prediction trend with experiemental results but the predicted strength is smaller than experiemental resutls.

6.2 Further studies

The thesis has achieved certain results; however, there are still problems un-resolved which related to the selection of materials, air-beams producing, and measuring methods. Therefore, this study could be expanded to those with infilled-gas beams and other inflating structures. Different loading conditions and different shapes of the inflating structures could be considered to be investigated in future.

For the numerical model, the problems could be extended to those which also considered the failure of composite materials. Other modelling techniques, e.i. using 3d shell model, could be used as an alternative approach to investiga the response of the inflating beams, especially when the local reponses is of interest.

As the results showed that there are inconsistancies between numerical and experimental results for low-pressure beams and this could came from various sources of errors, a rigorious experimental procedure might be considered for further investigation. A more complex numerical, which considers the influence of air pressure in a different manner, might be used for a better prediction.

References

[1] Chawla K.K. (1987). *Carbon fiber composites*. In: Composite Materials. Research and Engineering. Springer, New York.

[2] Veldman, S. L. & Vermeeren, C. A. J. R. (2001). *Inflating Structures in Aerospace Engineering - An Overview*. European Conference on Spacecraft Structures, Materials and Mechanical Testing, (Vol. 468, p.93).

[3] Comer, R. L., & Levy, S. (1963). *Deflections of an inflating circular-cylindrical cantilever beam*. AIAA journal, 1(7), 1652-1655.

[4] Webber, J.P.H. (1982). *"Deflections of inflated cylindrical cantilever beams subjected to bending and torsion."* Aeronautical Journal, 86(10), 306-312.

[5] Main, J. A., Peterson, S. W., & Strauss, A. M. (1995). *Beam-type bending of space-based inflating membrane structures*. Journal of Aerospace Engineering, 8(2)120-125.

[6] Suhey, J., Kim, N., and Niezrecki, C. (2005). *Numerical modeling and design of inflating structures-application to open-ocean-aquaculture cages*. Aquacultural Engineering, 33:285–303.

[7] Fichter, W. B. (1966). *A theory for inflating thin-wall cylindrical beams*. National Aeronautics and Space Administration.

[8] Topping, A.D. (1963). *"Shear deflections and buckling characteristics of inflated members."* Journal of Aircraft, 1(5), 289-292.

[9] Douglas, W.J. (1969). *"Bending stiffness of an inflated cylindrical cantilever beam."* AIAA Journal, 7(7), 1248-1253.

[10] Wielgosz, C., & Thomas, J. C. (2002). *Deflections of inflating fabric panels at high pressure*. Thin-walled structures, 40(6), 523-536.

[11] Thomas, J. and Wielgosz, C. (2004). *Deflections of highly inflating fabric tubes*. Thin-Walled Structures, 42:1049–1066.

[12] Le van, A. and Wielgosz, C. (2005). *Bending and buckling of inflating beams: Some new theoretical results*. Thin-Walled Structures, 43(8):1166–1187.

[13] Cavallaro, P. V., Johnson, M., and Sadegh, A. (2003). *Mechanics of plain-woven fabrics for inflating structures*. Composite Structures, 61:375–393.

[14] Wielgosz, C. and Thomas, J. (2003). *An inflating fabric beam finite element*. Communications in Numerical Methods in Engineering, 19:307–312.

[15] Bouzidi, R., Ravaut, Y., and Wielgosz, C. (2003). *Finite elements for 2d problems of pressurized membranes*. Computers and Structures, 81:2479–2490.

[16] Le van, A. and Wielgosz, C. (2007). *Finite elementing formulation for inflating beams*. Thin-Walled Structures, 45(2):221–236.

[17] Davids, W.G. (2007). *Finite elementing analysis of tubular fabric beams including pressure effects and local fabric wrinking*. Finite elementingAnalysis and Design, 44:24-33.

[18] Davids, W.G. and Zhang, H. (2008) *Beam Finite elementing for nonlinear analysis of pressurized fabric beam-columns*. Engineering structures, 30: 1969-1980.

[19] Malm, C., David, W., Peterson, M. and Turner, A. W. (2009). *Experimental characterization and finite elementing analysis of inflating fabric beams.* Construction and Building Materials, 23:2027-2034.

[20] Plaut, R., Goh, J., Kigudde, M., and Hammerand, D. (2000). *Shell analysis of an inflating arch subjected to snow and wind loading*. International Journal of Solids and Structures, 37:4275–4288.

[21] Plagianakos, T.S., Teutsch, U., Crettol, R., and Luchsinger, R.H. (2009) *"Static response of a spindle-shaped Tensairity column to axial compression."* accepted in Engineering Structures.

[22] Nguyen, T. T., Ronel, S., Massenzio, M., Apedo, K. L., & Jacquelin, E. (2012). *Analytical buckling analysis of an inflating beam made of orthotropic technical textiles*. Thin-Walled Structures, 51, 186-200.

[23] Hughes, T.J.R., Cottrell, J.A. and Bazilevs, Y. (2005). *Isogeometric analysis: CAD, finite elements, NURBS, exact geometry and mesh refinement*. Comput. Methods Appl. Mech. Engrg., 194, pp 4135-4195.

[24] J.A. Cottrell, A. Reali, Y. Bazilevs, T.J.R. Hughes. (2006). *Isogeometric analysis of structural vibrations*. Computer Methods in Applied Mechanics and Engineering, 195(41)5257-5296.

[25] Wolfgang A. Wall, Moritz A. Frenzel, Christian Cyron. (2008). *Isogeometric structural shape optimization*. Computer Methods in Applied Mechanics and Engineering, 197(33)2976-2988.

[26] Kiendl, J., Bletzinger, K. U., Linhard, J., & Wüchner, R. (2009). *Isogeometric shell analysis with Kirchhoff–Love elements*. Computer Methods in Applied Mechanics and Engineering, 198(49), 3902-3914.

[27] Nguyen-Thanh, N., Valizadeh, N., Nguyen, M. N., Nguyen-Xuan, H., Zhuang, X., Areias, P., ... & Rabczuk, T. (2015). *An extended isogeometric thin shell analysis based on Kirchhoff–Love theory*. Computer Methods in Applied Mechanics and Engineering, 284, 265-291.

[28] Benson, D. J., Bazilevs, Y., Hsu, M. C., & Hughes, T. J. R. (2010). *Isogeometric shell analysis: the Reissner–Mindlin shell*. Computer Methods in Applied Mechanics and Engineering, 199(5), 276-289.

[29] Thai, C. H., Nguyen-Xuan, H., Nguyen-Thanh, N., Le, T. H., Nguyen-Thoi, T., & Rabczuk, T. (2012). *Static, free vibration, and buckling analysis of laminated composite Reissner–Mindlin plates using NURBS-based isogeometric approach*. International Journal for Numerical Methods in Engineering, 91(6), 571-603.

[30] Thai, C. H., Ferreira, A. J. M., Carrera, E., & Nguyen-Xuan, H. (2013). *Isogeometric analysis of laminated composite and sandwich plates using a layerwise deformation theory*. Composite Structures, 104, 196-214.

[31] Benson, D. J., Bazilevs, Y., Hsu, M. C., & Hughes, T. J. R. (2011). *A large deformation, rotation-free, isogeometric shell*. Computer Methods in Applied Mechanics and Engineering, *200*(13), 1367-1378.

[32] Tran, L. V., Ferreira, A. J. M., & Nguyen-Xuan, H. (2013). *Isogeometric analysis of functionally graded plates using higher-order shear deformation theory*. Composites Part B: Engineering, 51, 368-383.

[33] Nguyen-Xuan, H., Tran, L. V., Thai, C. H., Kulasegaram, S., & Bordas, S. P. A. (2014). *Isogeometric analysis of functionally graded plates using a refined plate theory*. Composites Part B: Engineering, 64, 222-234.

[34] Piegl, L. and Tiller, W. (1997). *The NURBS book. 2nd edition*, Pringer-Verlag, New York.

[35] Rogers, D.F. (2001). *An introduction to NURBS: with historical perspective*. Morgan Kaufmann Publishers, New York.

[36] Cottrell, J.A., Hughes, T.J.R. and Bazilevs, Y. (2009). *Isogeometric Analysis: To-ward Integration of CAD and FEA*. John Wiley & Sons, New York.

[37] T.J.R. Hughes, J.A. Cottrell, Y. Bazilevs. (2005). *Isogeometric Analysis: CAD, Finite Elements, NURBS, Exact Geometry and Mesh Refinement*. Computer Methods in Applied Mechanics and Engineering, 194(39)4135-4195.

[38] Zhang, Y., Bazilevsj, Y., Goswami, S., Bajaj, C. and Hughes, T.J.R. (2007). *Patientspecic vascular NURBS modeling for isogeometric analysis of blood ow*. Comput. Methods Appl. Mech. Engrg., 196, pp 2943-2959.

[39] Cottrell, J.A., Hughes, T.J.R. and Reali, A. (2007). *Studies of renement and continuity in isogeometric structural analysis*. Comput. Methods Appl. Mech. Engrg., 196, pp 4160-4183.

[40] Hughes, T.J.R., Reali, A. and Sangalli. G. (2010). *Efficient quadrature for NURBS- based isogeometric analysis*. Comput. Methods Appl. Mech. Engrg., 199, pp 301-313.

[41] Pilkey, W.D. and Pilkey, D.F. (2008). *Peterson's stress concentration factors*. 3rd edition, John Wiley & Sons, New Jersey.

[42] Bezier, P.E. (1972). *Numerical control: mathematics and applications*. John Wiley, New York.

[43] Main, J. A., Peterson, S. W., & Strauss, A. M. (1994). *Load-deflection behavior of space-based inflating fabric beams*. Journal of Aerospace Engineering, 7(2), 225-238.

[44] Wielgosz, C. (2005). *Bending and buckling of inflating beams: some new theoretical results*. Thin-Walled Structures, 43(8), 1166-1187.

[45] Apedo, K. L., Ronel, S., Jacquelin, E., Massenzio, M., & Bennani, A. (2009). *Theoretical analysis of inflating beams made from orthotropic fabric*. Thin-walled structures, 47(12), 1507-1522.

[46] Libai, A. and Givoli, D. (1995). *Incremental stresses in loaded orthotropic circular membrane tubes-i*. theory. International Journal of Solids and Structures, 32:13:1907–1925.

[47] Diaby, A., Le-Van, A., and Wielgosz, C. (2006). *Buckling and wrinkling of prestressed membranes*. Finite Elements in Analysis and Design, 42:992–1001.

[48] Apedo, K. L., Ronel, S., Jacquelin, E., Bennani, A., & Massenzio, M. (2010). *Nonlinear finite elementing analysis of inflating beams made from orthotropic woven fabric*. International Journal of Solids and Structures, 47(16), 2017-2033.

[49] Bhatti, M. (2006). *Advanced topics in finite elementing analysis of structures with Mathematica and MATLAB computations*. New York (NY): John Wiley & Sons.

[50] Ovesy, H. R., & Fazilati, J. (2009). *Stability analysis of composite laminated plate and cylindrical shell structures using semi-analytical finite strip method*. Composite Structures, 89(3), 467-474.

[51] Paschero, M., & Hyer, M. W. (2009). *Axial buckling of an orthotropic circular cylinder: Application to orthogrid concept.* International Journal of Solids and Structures, 46(10), 2151-2171.

[52] Nguyen, T. T., PhD Dissertation. (2012). *Numerical modeling and buckling analysis of inflating structures*. University Claude Bernard.

[53] Rogers, D.F. (2001). An introduction to NURBS: with historical perspective. Morgan Kaufmann Publishers, New York.

[54] Kiendl, J.M. (2011). Isogeometric analysis and shape optimal design of shell structures. PhD thesis. The Entrepreneurial Univesity.

[56] Bensen, D.J., Bazilevs, Y., Hsu, M.C. and Hughes, T.J.R. (2009). Isogeometric shell analysis: the Reissner-Mindlin shell. Comput. Methods Appl. Mech. Engrg., 199, pp 276-289.

[57] Shojaee, S., Izadpanah, E., Bui, T.Q. and Vu, V.T. (2012). Free vibration and buckling analysis of laminated composite plates using the NURBS-based isogeometric_nite element method. Compos. Struct., 94, pp 16771693.

[58] Bazilevs, Y., Calo, V.M., Hughes, T.J.R. and Zhang Y. (2008). Isogeometric uidstructure interaction: theory, algorithms and computations. Comput. Mech., 43, pp 3-37.

[59] Cottrell, J.A., Reali, A., Bazilevs, Y. and Hughes, T.J.R. (2006). Isogeometric analysis of structural vibrations. Comput. Methods Appl. Mech. Engrg., 195, pp 5257-5296.

[60] Kagan, P., Fischer, A. and Bar-Yoseph, P.Z. (1998). *New B-spline_nite element approach for geometrical design and mechanical analysis*. Int. J. Numer. Methods Engrg., 41, pp 435-458.

[61] Chapelle, D. and Bathe. K.J. (2011). *The Finite elementing Analysis of Shells - Fun- damentals*. 2nd edition, Springer, New York.

[62] Bazilevs, Y., Calo, V.M., Cottrell, J.A., Evans, J.A., Hughes, T.J.R., Lipton, S., Scott, M.A. and Sederberg, T.W. (2010). *Isogeometric analysis using T-splines, Comput*. Methods Appl. Mech. Engrg., 199, pp 229-263.

[63] Nguyen-Thanh, N., Nguyen-Xuan, H., Bordas, S.P.A. and Rabczuk, T. (2011). *Isogeometric analysis using polynomial splines over hierarchical T-meshes for two-dimensional elastic solids, Comput*. Methods Appl. Mech. Engrg., 200, pp 1892-1908.

[64] Dörfel, M.R., Jüttler, B. and Simeon, B. (2010). *Adaptive isogeometric analysis by local h-renement with T-splines, Comput*. Methods Appl. Mech. Engrg., 199, pp 264-275.

[65] Hughes, T. J., Cottrell, J. A., & Bazilevs, Y. (2005). *Isogeometric analysis: CAD, finite elements, NURBS, exact geometry and mesh refinement*. Computer methods in applied mechanics and engineering, 194(39), 4135-4195.

[66] Apedo, K. (2010a). *Numerical modelling of inflating structures made of orthotropic technical textiles: Application to the frames of inflating tents*. PhD thesis, University of Claude Bernard Lyon 1.

[67] Apedo, K. L. (2010b). *Numerical modelling of inflating structures made of orthotropic technical textiles: Application to the frames of inflating tents*. PhD thesis, University of Claude Bernard Lyon 1.

[68] Babcock, C. (1983). *Shell stability*. Journal of Applied Mechanics, 50:935–940.

[69] Badel, P., Vidal-Salle´, E., and Boisse, P. (2007). *Computational determination of in-plane shear mechanical behaviour of textile composite reinforcements*. Computational Materials Science, 40:439–448.

[70] Blackketter, D., Walrath, D., and Hansen, A. (1993). *Modeling damage in a plain weave fabric-reinforced composite material*. J Comp Tech Res (JCTRER), 15:2:36–142.

[71] Bonet, J., Wood, R., Mahaney, J., and Heywood, P. (2000). *Finite elementing analysis of air supported membrane structures*. Computer Methodes in Applied Mechanics and Engineering, 190:579–595.

[72] Braun, M., Bischoff, M., and Ramm, E. (1994). *Nonlinear shell formulations for complete three-dimensional constitutive laws include composites and laminates*. Computational Mechanics, 15:1–18.

[73] Carvelli, V., Corazza, C., and Poggi, C. (2008). *Mechanical modelling of monofilament technical textiles*. Computational Materials Science, 42:679–691.

[74] Chou, T. (1992). *Microstructural Design of Fibre Composites*. Cambridge University Press, Cambridge.

[75] Christensen, R. and Waals, F. (1972). *Effective stiffness of randomly oriented fibre composites*. Journal of Composite Materials, 6(3):518–535.

[76] Cook, R., Malkus, D., and Plesha, M. (1989). *Concepts and Applications of Finite elementing Analysis*. Wiley, New York.

[77] Cook, R. D., Malkus, D. S., Plesha, M. E., and Witt, R. J. (2002). *Concepts and Applications of Finite elementing Analysis*. John Wiley & Sons Inc.

[78] Cowper, G. (1967). *The shear coefficient in timoshenko's beam theory*. J Appl Mech, 33:335–340.

[79] Cox, B. and Flanagan, G. (1996a). *Handbook of Analytical Methods for Textile Composites*. Rockwell Science Center, Thousand Oaks, CA.

[80] Craig, P. and Summerscales, J. (1988). *Poisson's ratios in glass fibre reinforced plastics*. Composite Structures, 9(3):173 – 188.

[81] Daniel, M. and Ishai, O. (1994). *Engineering mechanics of composite materials*. Oxford University Press.

[82] Djaja, R. (1989). *Finite elementing modeling of fibrous assemblies*. Master's thesis, University of Canterbury, New Zealand.

[83] Esslinger, M. and Geier, B. (1975). *Postbuckling behavior of structures, volume (236) of CSIM Courses and Lectures*. Springer-Verlag, Berlin, New York.

[84] Grosberg, P., Leaf, A., and Park, B. (1968). *The mechanical properties of woven fabrics*. part vi: the elastic shear modulus of plain-weave fabrics. Text Res J, pages 1085–1100.

[85] Harrison, P., Clifford, M., and Long, A. (2004). *Shear characterization of viscous woven textile composites: a comparison between picture frame and bias extension experiments*. Composites Science and Technology, 64:1453–1465.

[86] Haughton, D. and McKay, B. (1996). *Wrinkling of inflating elastic cylindrical membranes under flexure*. International Journal of Engineering Science, 34(13):1531–1550.

[87] Herakovich, C. T. (1998). *Mechanics of Fibrous Composites*. John Wiley & Sons Inc.

[88] Houliara, S. and Karamanos, S. (2006). *Buckling and post-buckling of long pressurized elastic thin-walled tubes under in-plane bending*. International Journal of Non-Linear Mechanics, 41:491–511.

[89] Houliara, S. and Karamanos, S. (2010). *Stability of long transversely-isotropic elastic cylindrical shells under bending*. International Journal of Solids and Structures, 47:10–24.

[90] Hutchings, A. L. (2009). *Experimental determination of material properties for inflating aeroshell structures*. Technical report, Georgia Institute of Technology, Atlanta, GA.

[91] Hyer, M. (1998). *Stress analysis of fiber-reinforced composite materials*. New York: McGraw-Hill.

[92] Itskov, M. (2001). *A generalized orthotropic hyperelastic material model with application to incompressible shells*. International Journal for Numerical Methods in Engineering, 50:1777–1799.

[93] Ivanov, I. and Tabiei, A. (2001). *Three-dimensional computational micromechanical model for woven fabric composites*. Composite Structures, 54:489–496.

[94] Jensen, D. and Hipp, P. (1991). *Compressive testing of filament-wound cylinders*. In Proceedings of the 8th International Conference on Composite Materials (ICCM/8), pages 35–F–1–35–F–9, Honolulu, Hawaii. Proceedings of the 8th International Conference on Composite Materials (ICCM/8).

[95] Jones, E. (1975). *Mechanics of Composite Materials*. Mc Graw-Hill Book Company, New York.

[96] King, M., Jearanaisilawong, P., and Socrate, S. (2005). *A continuum constitutive model for the mechanical behavior of woven fabrics*. International Journal of Solids and Structures, 42:3867–3896.

[97] Ko, F. (1989). *Preform fiber architecture for composites*. Ceramic Bull., 68(2). Kuo, W.-S. and Pon, B.-J. (1997). Elastic moduli and damage evolution of three-axis woven fabric composites. Journal of materials science, 32:5445–5455.

[98] Lebrun, G., Bureau, M. N., and Denault, J. (2003). *Evaluation of bias-extension and picture-frame test methods for the measurement of intraply shear properties of pp/glass commingled fabrics*. Composite Structures, 61(4):341–352. Selected Papers from the Symposium on Design and Manufacturing of Composites.

[99] Lee, S.-K., Byun, J.-H., and Hong, S. H. (2003). *Effect of fiber geometry on the elastic constants of the plain woven fabric reinforced aluminum matrix composites*. Materials Science and Engineering, A347:346–358.

[100] Levy, R. and Spillers, W. (1995). *Analysis of Geometrically Nonlinear Structures*. Chapman & Hall, London.

[101] Liu, L., Chen, J., Li, X., and Sherwood, J. (2005). *Two-dimensional macromechanics shear models of woven fabrics*. Composites: Part A, 36:105–114.

[102] Lomov, S., Barburski, M., Stoilova, T., Verpoest, I., Akkerman, R., Loendersloot, R., and Thije, R. (2005). *Carbon composites based on multiaxial multiply stitched preforms. part 3: Biaxial tension, picture frame and compression tests of the preforms*. Composites Part A: Applied Science and Manufacturing, 36(9):1188–1206.

[103] Long, A. (2005). *Design and manufacture of textile composites*. CRC Press LLC.

[104] Lu, K., Accorsi, M., and Leonard, J. (2001). *Finite elementing analysis of membrane wrinkling*. International Journal for Numerical Methods in Engineering, 50:1017– 1038.

[105] Luijk, C. V. (1981). *Structural Analysis of Wool Yarns*. PhD thesis, University of Canterbury, New Zealand.

[106] Lussier, D. and Chen, J. (2000). *Shear frame standardization for stamping of thermoplastic woven fabric composites*. In 32nd International SAMPE Technical Conference, pages 150–160.

[107] Masters, J., Foye, R., Pastore, C., and Gowayed, Y. (1993). *Mechanical properties of triaxial braided composites: experimental and analytical results*. Journal of Composites Technology Research, 15(2):112–122.

[108] NASA (1965). *Buckling of thin-walled circular cylinders*. Technical report, NASA Space vehicle design criteria. NASA SP-8007.

[109] Nguyen, T.-T., Ronel, S., Massenzio, M., Phan, D.-H., Apedo, K., and Jacquelin, E. (2012b). *An analytical approach for buckling analysis of an inflating beam made of orthotropic technical textiles*. In 8th European Solid Mechanics Conference, Graz, Autria.

[110] Onate, E. (2008). *Structural Analysis by the Finite elementing Method*. Vol.2: Beams, Plates and Shells. CIMNE-Springer.

[111] Pan, N. (1996). *Analysis of woven fabric strengths: Prediction of fabric strength under uniaxial and biaxial extensions*. Composites Science and Technology, 56:311–327.

[112] Peng, X. and Cao, J. (2005). *A continuum mechanics-based non-orthogonal constitutive model for woven composite fabrics*. Composites: Part A, 36:859–874.

[113] Posada, L. M. (2007). *Stability analysis of two-dimensional truss structures*. Master's thesis, University of Stuttgart.

[114] Potluri, P. and Thammandra, V. (2007). *Influence of uniaxial and biaxial tension on meso-scale geometry and strain fields in a woven composite*. Composite Structures, 77(3):405–418.

[115] Quaglini, V., Corazza, C., and Poggi, C. (2008). *Experimental characterization of orthotropic technical textiles under uniaxial and biaxial loading*. Composites: Part A, 39:1331–1342.

[116] Saadé, K., Espion, B., and Warzée, G. (2002). *Flexural torsional buckling of three dimensional thin walled elastic beams*. In 15th ASCE Engineering Mechanics Conference. Columbia University, New York, NY.

[117] Scida, D., Aboura, Z., Benzeggagh, M., and Bocherens, E. (1997). *Prediction of the elastic behaviour of hybrid and non-hybrid woven composites*. Composites Science and Technology, 57:1727–1740.

[118] Singer, J. (1982). *The status of experimental buckling investigation of shells, in: Buckling of shells*. In Ramm, E., editor, Proceedings of the State-of-the-Art Colloquium, Stuttgart, Springer-Verlag, Berlin, Heidelberg, New York, pages 501–533.

[120] Singer, J., Arbocz, J., and Weller, T. (1998). *Buckling Experiments, Experimental Methods in Buckling of Thin-Walled Structures, Volume 1, Basic Concepts, Columns, Beams and Plates*. John Wiley & Sons.

[121] Taylor, R. (2001). *Finite elementing analysis of membrane structures*. In Internal CIMNE report, Barcelona.

[122] Tennyson, R. (1980). *Interaction of cylindrical shell buckling experiments with theory, in: Theory of Shells*. North-Holland Publishing Co.

[123] Valdés, J., J. Miquel, and Onate, E. (2009). *Nonlinear finite elementing analysis of orthotropic and prestressed membrane structures*. Finite Elements in Analysis and Design, 45:395–405.

[124] Veldman, S. (2006). *Wrinkling prediction of cylindrical and conical inflating cantilever beams under torsion and bending*. Thin-Walled Structures, 44(2):211–215.

[125] Veldman, S., Bergsma, O., and Beukers, A. (2005a). *Bending of anisotropic inflating cylindrical beams*. Thin-Walled Structures, 43:461–475.

[126] Veldman, S., Bergsma, O., Beukers, A., and Drechslerb, K. (2005b). *Bending and optimisation of an inflating braided beam*. Thin-Walled Structures, 43:1338–1354.

[127] Zienkiewiezcz, O. and Taylor, R. (2000). *The Finite elementing Method*. ButterworthHeinemann, Oxford, Fifth edition.

[128] Zouani, A., Bui-Quoc, T., and Bernard, M. (1999). *Cyclic stress-strain data analysis under biaxial tensile stress state*. Exp Mech, 39:92–102.

[129] Almroth, B.O., Holmes, A.M.C. & Brush, D.O. (1964). *An experimental study of the bucking of cylinders under axial compression*. Experimental Mechanics 4, 263–270.

[130] Nguyen, T.T, Ronel, S., Massenzio, M., Jacquelin, E., Apedo, K.L., Phan-Dinh, H. (2013) *Numerical buckling analysis of an inflatable beam made of orthotropic technical textiles*, Thin-Walled Structures 72. 61-75.

List of Publications

Parts of this dissertation have been published in international journals, national journals or presented in conferences. These papers are:

- **Articles in international scientific journal**

1. T. Le-Manh, Q. Huynh-Van, **Thu D. Phan**, Huan D. Phan, H. Nguyen-Xuan "Isogeometric nonlinear bending and buckling analysis of variablethickness composite plate structures". *Composite Structures 2017,* Pages 818-826.

- **International Conference**

2. **Phan Thi Dang Thu**, Phan Dinh Huan and Nguyen Thanh Truong "Effect parametric to properties of a 2D orthogonal plain classical woven fabric composite". *International Conferrence on Engineering Mechanics and Automation (ICEMA), Ha Noi city 2014* - ISBN: 978-604-913-367-1, pages 509-517.

- **National Conference**

3. **Phan Thi Dang Thu**, Phan Dinh Huan and Nguyen Thanh Truong "Biaxial beam inflation test on orthotropic fabric beam"; *National Conference on Solid Mechanics, Ho Chi Minh city 2013* - ISBN: 978-604-913-213-1, pages 1169-1176.

4. Nguyen Thanh Truong, Phan Dinh Huan, **Phan Thi Dang Thu** "Discretizing an analytical inflating beam model by the shellmembrane finite elelment". *National Conference on Solid Mechanics, Ho Chi Minh city 2013* - ISBN: 978-604-913-213-1, pages 1221-1228.

5. **Phan Thi Dang Thu**, Le Manh Tuan, Nguyen Xuan Hung, Nguyen Thanh Truong "Geometrically nonlinear behaviour of composite beams of variable fiber volume fraction in isogeometric analysis". *National Conference on Solid Mechanics, Da Nang city 2015* - ISBN: 978-604-82-2028-0, Pages: 1404-1409.

6. **Thu Phan-Thi-Dang**, Tuan Le-Manh, Giang Le-Hieu, Truong Nguyen-Thanh "Buckling of cylindrical inflating composite beams using isogeometric analysis". *Proceedings of the National Conference on science and technology in*

mechanics IV, Ho Chi Minh City 2015, Viet Nam - ISBN: 978-604-73-3691-3, Pages 821-826.

7. **Phan Thi Dang Thu**, Nguyen Thanh Truong, Phan Dinh Huan "Mô hình dầm hơi composite phi tuyến chịu uốn". *National Scientific Conference on Composite Materials and Structures, Nha Trang city 2016* - ISBN: 976-604-82-2026-6, Page 699-706.

8. **Phan Thi Dang Thu**, Nguyen Thanh Truong, Phan Dinh Huan, Le Dinh Tuan "Biaxial experiments for determining material properties and joint strength of textile plain woven fabric composites". *National Conference on Solid Mechanics, Ha Noi city 2017* - ISBN: 978-604-913-722-8, Page 1174-11.